

Flexible Linear Motors for Mobile Continuum Robots

(移動連続体ロボットのための柔軟直動モータに関する研究)

January, 2020

Doctor of Philosophy (Engineering)

Ayato Kanada

金田 礼人

Toyohashi University of Technology

Acknowledgements

I would like to thank my supervisor Prof. Tomoaki Mashimo for the continuous supports of my BSc, MSc, and Ph.D study for six years.

I would like to thank my external supervisors: Prof. Fumiya Iida for giving me great opportunities to work at Cambridge for six months; Prof. Taro Nakamura and Prof. Hiromi Mochiyama for their many comments and discussions in my examinations of promotion.

I am grateful to all my lab's staff, Prof. Zhong Zhang, Prof. Takamua Akiduki and ex-lab's staff, Prof. Kazuhiko Terashima, Prof. Takanori Miyoshi, and Prof. Ryosuke Tasaki. I would like to also thank all of our lab and ex-lab members at Toyohashi University of Technology and Iida's lab members at University of Cambridge for helping me out in my work and stay.

Abstract

Organisms that exploit soft structures produce the incredible capabilities for locomotion and manipulation in complex natural environments. While conventional robots with discrete links and rigid actuators are fast, strong, and easy to control, they struggle to operate in such surroundings. Soft robots with a deformable, continuum body and soft actuators can potentially approach this problem due to their elasticity, safety of interaction, and environmental adaptability. However, soft actuators have several problems including a limited stroke, difficulty of control, and slow response time, restricting their deployment. On the other hand, rigid actuators such as electromagnetic and piezoelectric motors widely adopted today solve these drawbacks, but do not have the softness.

A combination of soft and classical technologies may address this challenge. This thesis introduces a concept of flexible linear motors that consists of a rigid motor's stator and a flexible elongated shaft. By moving the flexible shaft linearly via changes of a relative position to the stator, flexible linear motors provide a large stroke, fast response time, and ease of control. This research shows two examples of how flexible linear motors can be realized and investigates how the above advantages contribute to the mobility of continuum soft robots.

One is a flexible ultrasonic motor that consists of a single metal cube stator with a hole and an elastic and long coil spring inserted into the hole. When voltages are applied to piezoelectric elements on the stator, a shaft inserted the hole moves back and forth. To investigate the influence of softness on the ultrasonic motor, we first inserted a slightly flexible coil spring and a solid shaft into the stator. We change both shafts diameter with micron-order accuracy to provide a pre-pressure between the stator and shaft to improve the output of the ultrasonic motor. Experiments show that the coil spring is easier to adjust the pre-pressure and provides a larger output. Next, we use the elastic and long coil spring to bring flexibility for the motor and enables a large stroke. The coil spring also works as a position sensor by regarding itself as a variable resistance. In order to clarify the design methodology, the pre-pressure, motion model, and position sensing of the coil spring are formulated. The resulting sensor-actuator system has good response characteristics, high linearity, and robustness, without reducing flexibility and controllability. We build a

continuum robot based on two flexible ultrasonic motors and demonstrate feedback control of planar motion based on the constant curvature model.

The other is a flexible rack pinion actuator that consists of a pinion gear rotated by DC motor and a flexible metallic tube that works as a rack. Rotating the pinion gear moves the flexible tube linearly by a engage with the helical groove on the tube surface. We build a continuum robot whose section has three flexible rack pinion actuators connected in parallel. The elongation and bending motion of each section can be controlled during operation by varying the speed of each flexible tube. This design not only allows the expansion of the robot to otherwise unreachable work areas but also improves the locomotion velocity by generating a large traveling distance of the flexible tubes. First, we test two types of locomotion on the ground using a continuum robot with the two sections (6 DoF). The results show that earthworm-like locomotion with a large body stretch has good mobility even in a slippery environment. Next, study how soft and large deformations can enhance the climbing capabilities of LEECH; a natural land leech-inspired continuum robot with the one section (3 DoF) and two suction cups at the ends. The large deformations occurring in LEECH extend its workspace compared to robots based on constant curvature models, and we show successful locomotion transition from one surface to another at angles between 0° and 180° in experiment.

The findings in this thesis demonstrate that the proposed motors provide capabilities and behaviors that cannot be achieved by either soft actuators or conventional rigid motors alone. Using the concept of the flexible linear motor results in continuum robots with good mobility, and has the potential to erase the boundary between conventional rigid and soft robots.

Preface

The content of this dissertation is based on five peer-reviewed publications. The content of the publications has been edited and extended to match this thesis.

The publications are:

1. A. Kanada and T. Mashimo, “Design and Experiments of Flexible Ultrasonic Motor using a Coil Spring Slider,” *IEEE/ASME Transaction on Mechatronics*, Vol. 25, No. 1, pp. 468–476, 2019.
2. A. Kanada, F. Giardina, T. Howison, T. Mashimo, and F. Iida, “Reachability Improvement of a Climbing Robot based on Large Deformations induced by Tri-Tube Soft Actuators,” *Soft Robotics*, Vol. 6, No. 4, pp. 483-494, 2019.
3. A. Kanada and T. Mashimo, “Mobile Continuum Robot with unlimited section lengths”, in *2018 IEEE/RSJ International Conference on Intelligent Robots and Systems (IROS)*, 2018, pp. 7117-7122.
4. A. Kanada, T. Mashimo, and K. Terashima, “Flexible Ultrasonic Motor using an Output Coil Spring”, in *2017 IEEE/RSJ International Conference on Intelligent Robots and Systems (IROS)*, 2017, pp. 5616-5621.
5. A. Kanada, T. Mashimo, and K. Terashima, “Study on Output Shafts for a Rotary-Linear Ultrasonic Motor,” *International Journal of Automation Technology* (Special issue on Innovative Actuators), Vol. 10, No. 4, pp. 549-556, 2016.

Table of contents

List of figures	viii
List of tables	xi
1 Introduction	1
1.1 Continuum Robots	3
1.1.1 Extrinsic Actuation	3
1.1.2 Intrinsic Actuation	4
1.2 Linear Actuators	4
1.2.1 Rigid Linear Actuators	5
1.2.2 Soft Expansion/Contraction Actuators	6
1.2.3 Flexible Linear Motors	7
1.3 Specific Applications	10
1.3.1 Pipeline Inspection Robot	10
1.3.2 Climbing Robot	11
1.4 Objective	12
1.5 Thesis Organization	12
2 Flexible Ultrasonic Motor	14
2.1 Ultrasonic Motor Overview	14
2.2 Driving Principle	15
2.2.1 Rotation	15
2.2.2 Translation	19
2.3 Ancestor of Flexible Ultrasonic Motor	22
2.3.1 Stator Characteristics	22
2.3.2 Pre-pressure Mechanisms and Experiments	27
2.3.3 Conclusion	33
2.4 Flexible Ultrasonic Motor Prototype	33

2.4.1	Modeling	33
2.4.2	Static Evaluation	39
2.4.3	Dynamic Evaluation	44
2.4.4	Conclusion	45
2.5	Twin-coil USM	47
2.5.1	Design and Fabrication	48
2.5.2	Experiments	51
2.5.3	Demonstration of a Twin-coil USM	55
2.5.4	Conclusion	57
3	Flexible Rack Pinion Actuator	59
3.1	Design and Mechanism	59
3.1.1	Robot Common Design	60
3.2	Mobile Continuum Robot	60
3.2.1	Kinematics	61
3.2.2	Experiments	63
3.2.3	Conclusion	70
3.3	Climbing Continuum Robot	71
3.3.1	Modeling	72
3.3.2	Robot Architecture and Locomotion Principle	76
3.3.3	Experiments	78
3.3.4	Conclusion	87
4	Conclusion and Future Work	90
4.1	Conclusion	90
4.2	Future Work	91
	References	92
	Appendix A Experimental Verification of the Strain Energy	100

List of figures

1.1	Classification of linear actuators	5
1.2	Rigid linear actuators	6
1.3	Soft actuators	8
1.4	Imaginary view of a flexible linear motor	9
1.5	Imaginary view of a continuum robot using flexible linear motors	10
2.1	Schematic of the stator	16
2.2	Vibration modes for rotation	18
2.3	Generation of elliptical motions for rotation	19
2.4	Vibration modes for translation	21
2.5	Generation of elliptical motions for translation	22
2.6	Schematic of the rotary-linear ultrasonic motor	23
2.7	Resonant frequency of the R3, T1, and T2 modes	24
2.8	Shematic diagram of the vibration measurement	25
2.9	Vibration Amplitude	26
2.10	Pre-pressure methods using two shafts	28
2.11	Prototype motors with two shafts	29
2.12	Resonant frequencies in changing the shaft diameter.	29
2.13	Experimental setup for measuring the torque and thrust force	31
2.14	Torque and thrust force in changing the shaft diameter	31
2.15	Relationship of torque and thrust force to the voltage frequency	32
2.16	Flexible ultrasonic motor	34
2.17	Geometric relationship between the coil spring and the stator	35
2.18	A generalized model of the flexible ultrasonic motor	37
2.19	A model at the right side of the coil spring	38
2.20	Support part for wiring	40
2.21	Frequency response of the T1 and T2 modes	41
2.22	Relation of the velocity and the force to pre-pressure	42

2.23	Experimental setup for measuring the velocity under load	43
2.24	Load characteristic of the flexible ultrasonic motor	43
2.25	Experimental setup to examine the relationship between the velocity and bending radius	44
2.26	The relationship between the velocity and bending radius	45
2.27	Step response of the flexible ultrasonic motor	46
2.28	Twin coil spring-based flexible ultrasonic motor (Twin-coil USM).	48
2.29	Principle of self-sensing using the coil	50
2.30	Constant curvature model for the Twin-coil USM	50
2.31	Change in the sensor output	52
2.32	Feedback control circuit for the flexible ultrasonic motor with self-sensing.	53
2.33	Time table of the control cycle.	53
2.34	Relationship between the velocity and the driving frequency	54
2.35	Feedback control scheme.	55
2.36	Bode plot for the flexible ultrasonic motor.	55
2.37	Structure of Twin-coil USM	56
2.38	The signals from the two coil spring-based resistive sensors	57
2.39	Experimental circular motion obtained by the camera	57
3.1	Overview of the flexible rack pinion actuator	60
3.2	Overview of the continuum robot using flexible rack pinion actuators	61
3.3	Kinematics of a continuum section	62
3.4	Experimental setup for measuring the robot end effector	65
3.5	Dynamic response following circular trajectories	66
3.6	Snake-like and Earthworm-like locomotion	68
3.7	Experiment to verify the robustness	69
3.8	Real leech and LEECH	71
3.9	Sketches of the proposed model	73
3.10	Simulation results of the model	77
3.11	System hierarchy	78
3.12	Steps in the locomotion procedure	79
3.13	Comparison of the flexible tube shape in simulation with the real world . .	80
3.14	One-chain model	82
3.15	Deformation for constant shape parameter σ	83
3.16	Comparison between the predicted endpoints of the constant curvature model and the two-chain model	84
3.17	Six types of locomotion maneuvers	86

3.18 Manipulator workspace for constant curvature and two-chain model 88

A.1 Strain energy stored by the twist of the coil spring 101

List of tables

- 1.1 Characteristics of flexible linear motors 13
- 2.1 Model Properties of the Flexible Ultrasonic Motor 47
- 3.1 Values of Physical Parameters of LEeCH Model 76

Chapter 1

Introduction

Robotics researchers have told us for decades that robots will become our good partners and enhance quality of our lives, but this has not yet been achieved. Conventional robots designed to be stiff to achieve a precise and repetitive position control are useful in well-defined and structured environments, primarily manufacturing factory. However, they struggle to operate in unstructured environments such as homes and open fields. This is a fundamental problem in robotics because of its limited ability to accurately recognize the surrounding environment and contact/deal objects in the right way, and overcoming it will be a milestone. Imagine a robot that picks up a small stone. First, the robot uses a camera or laser sensor to create a 3D model of the stone for picking, but due to sensor resolution and occlusion issues, the model is not perfect. Next, the robot considers how to pick up the stone, but many unknown factors such as hardness, material, weight, and friction of the stone lead to uncertainty in its behavior. These unexpected events stop the robot's operation and require human intervention to return. How do robots achieve such interactions with unstructured environments? One answer is softness (flexibility).

There are no milestones yet, but over the past 10 years there have been major changes in the structure of a typical robot consists of high-gear motors and rigid serial links. Atlas is a humanoid robot that employs a hydraulic system to absorb shocks, demonstrated a jumping on boxes, performing a backflip while jumping [1]. Cheetah is an MIT's (Massachusetts Institute of Technology) quadruped robot with low ratio gears for backdrivability, showed to jump over obstacles up to 40cm in height while running at 2.5 m/s [2, 3]. One key to achieving these superior motions is the softness or compliance of the actuator reduced complexity in their interactions with their environment. Another major change is the emergence of soft robotics, a new research field that seeks to achieve even greater softness in robots [4–6]. In soft robots, the actuators that make up most of their structure are made of soft, elastic, deformable materials such as rubber and elastomer. The inherent compliance of the soft

actuators leads to realize systems that are safer, cheaper, and adaptable than the level that a robot with the traditional motors can achieve. Researchers believed that a completely soft robot would achieve these full potentials, but it has a drawback, namely, it would be much too unconstrained. How would the robot recognize and control the infinite degrees of freedom (DoF) of its body? We don't yet have a design method and control system like a biological system that properly positions and uses myriad muscles and sensors. Unlike robots, animals with the system produce the incredible capabilities for locomotion and manipulation in unstructured environments.

The feasible way to bridge the gap between robots and animals is probably to gradually soften a traditional, completely rigid robot. The most successful robot that looks soft or flexible to date is hyper-redundant discrete robots (i.e. snake robots [7] or arm robots [8] with many DoF). They mainly consist of a number of rigid links connected in series and motors attached at each joint, which have a high level of dexterity to reach any point in a 3D workspace. However, they are inherently rigid to accurately determine the shape and tip position of the robot and their ability to conform to obstacles is limited. The next stage of hyper-redundant robots in robot softness is continuum robots. Continuum robots are defined as a robot that has a continuous form, or backbone, which can be bent at any point along its length [9]. With no prior planning or knowledge, the deformable body can help the robot adapt and navigate through confined spaces, prevent injuries in interaction with obstacles, which leads to energy efficiency for locomotion tasks.

Despite these great benefits, most of the applications of continuum robots are not mobile robots but manipulators. Although several hyper-redundant discrete manipulators have been replaced by continuum manipulators in the field of minimally invasive surgery [10], there is no sign yet that snake robots will be replaced by continuum robots. What is preventing the application of continuum robots? A satisfactory answer to this question is not fully understood within the scope of this study, but probably the lack of actuator performance is the main factor. Wire-driven and fluid elastomer actuators, which are most commonly used in continuous robots, are not suitable for locomotion because they require large external devices. In other actuators, the problems of response time, stroke (strain) range, and sensing limit applications. The stroke range issues are particularly important, and because high strains or large stroke are often required to achieve high mobilities. We describe the structure of continuum robots in the next subsection and the linear actuator of that in the next subsection to describe this problem in more detail.

1.1 Continuum Robots

The history of continuous robots is surprisingly long, and the generally first known example, "tensor arm", released in 1967, consists of a series of plates interconnected by universal joints driven by tendons [11]. To be precise, this robot is a not continuum robot but hyper redundant robot because it does not have a bendable continuous backbone. Even when the deformation is not continuous, some hyper redundant robots are sometimes classified as continuum robots because their sufficiently large degree of freedom and flexibility can realize most functions of continuum robots [9]. For example, a snake that is a vertebrate behaves like a continuum robot, but its backbone consists of very small rigid links (bones). In recent years, a continuum robot with a soft body, inspired by invertebrates, has been proposed. The octopus arm robot uses tendons or shape memory alloys to create longitudinal and lateral contractions in order to simulate a biological muscle system, and can exhibit basic movements of real octopus such as stretching and bending in water [12]. In particular, elongation motion is interesting because it does not exist in vertebrates whose length is fixed by the spine. A real octopus uses a strain amplification mechanism to provide a large elongation of 70%, which is not achieved with the octopus robot. The elongating/shortening motion is also applied in the locomotion of many invertebrates (e.g. earthworms, caterpillars, leeches) [13]. This locomotion method adapts confined spaces and works in unstructured environments. An important factor in determining their speed of locomotion is their displacement of the body elongation, but nature muscles generally only move in the direction of contraction. Many invertebrates use a flexible skeleton supported by fluid pressure called a hydrostatic skeleton to transform circular, radial or transverse muscle contraction into increased length body [14, 15]. Mechanical structures and actuators with capabilities comparable to natural hydrostatic skeletons have not yet been built. We approach this problem with structures and actuators that are different from animals. The next subsection discusses the general actuation/structure of continuum robots.

1.1.1 Extrinsic Actuation

The actuation of continuum robots is classified as either extrinsic or intrinsic depending on where actuation force occurs: when the force is transmitted from the outside of the robot structure through mechanical transmissions, it is extrinsic; when the force is generated inside the robot structure itself, it is intrinsic [10]. The common approach to drive continuum robots is the use of remotely actuated cables or thin rods. Most continuum robots are so-called single-back bone robots that have one central elastic structure and multiple disks that support the passage of cables [16–18]. Multi-backbone continuum robots use secondary backbones,

such as thin rods, instead of cables. They control bending motion by adjusting the lengths of the cables or secondary backbones from their base [19, 20]. For example, the use of a central backbone with an elastic structure is known to reduce the length of the robot by compressing the elastic body [21].

The another extrinsic actuation of continuum robots is a concentric-tube transmission. Concentric-tube robots are composed of multiple, precurved, elastic tubes that are nested inside of each other (The smaller the diameter, the farther the tube is positioned) [22, 23]. The tubes whose ends are not fixed to each other are translated and rotated to control the robot shape. The concentric backbone structure allows the continuum robots to generate the elongating/shortening motion by moving the backbones linearly [24–26]. These robots can obtain a relatively slender body and good accessibility into narrower spaces, but they are not suitable for locomotion due to large external spaces for actuation.

1.1.2 Intrinsic Actuation

Intrinsic actuated continuum robots usually form a backbone from soft actuators made of soft materials. In this respect, the robot design is close to biological structure. A typical structure has one or more sections, each section consists of three fluid elastomer actuators (FEAs) whose both ends are fixed to each other [27–29]. Depending on their design, FEAs either increase or decrease in length when pressurized. When each actuator operates at different pressures, the section bends along a nearly constant curvature. When each actuator operates at the same pressure, the length of the section either increases or decreases. Direct intrinsic actuation can reduce the external footprint, but the need for a fluid tether to a fixed position limits the range of movement.

While intrinsic actuation is clearly more suitable for mobile robots than extrinsic actuation, actuator specific problems prevent its application. In order to investigate this problem, the next section describes the details of general linear actuators and then discusses the performance of the actuator that we aim to build.

1.2 Linear Actuators

Linear motion is the basic unit movement in continuum robots and soft robots, which can be extended, contracted, bent and twisted by adding some constraints or combining the motions [30]. Here we classified linear actuators based on their materials and drive principles into four categories as shown in Fig. 1.1. First, they can be subdivided as hard or soft depending on the compliance of the material. In this category, the entire actuator does not

necessarily need to be soft, and only the driving part may be soft. For example, wire-driven are included in “soft” in spite of the use of conventional motors in external platforms for actuation because of the compliance of the wire or cable. Next, linear actuators can be subdivided as shape/volume-based or relative positions-based depending on the driving principle. For example, electromagnet motors generate the motion via changes of relative positions between their components such as stator and rotor, while soft actuators generate the motion via changes of their shape or volume due to stresses generated within them. The former produces large strokes with their continuous drive according to the shaft length, whereas the latter has compliance due to fluid compression and material stiffness. Let us summarize the features of each linear actuator.

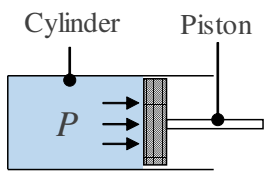
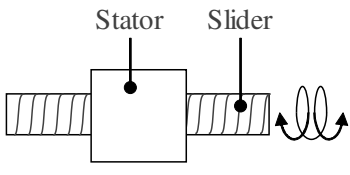
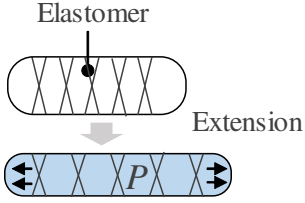
		Driving Principle	
		Shape/Volume	Relative Positions
Material	Hard	a 	b 
	Soft	c 	d 

Fig. 1.1 Classification of linear actuators based on materials and driving principles. (a) Fluidic cylinders. (b) Traditional linear motor including electromagnetic motor and piezoelectric motors. (c) Soft expansion and contraction actuators. (d) A few exceptions exist [31–33] but are not generally recognized.

1.2.1 Rigid Linear Actuators

Fluidic cylinders and electromagnetic motors are typical conventional linear actuators, and are shown in the Fig. 1.2 (a) and (b), respectively. The fluidic cylinders are mechanical

devices that use the power of compressed fluid to produce a force in a reciprocating linear motion. The most common cylinder has a simple mechanism that consists of a piston and rod moving inside a closed cylinder, and generated by air or hydraulic pressure. These cylinders are cheaper, reliable, and have compliance in the axial direction due to fluid compressibility. However, they have a limited stroke range by the length of the cylinder and a control difficulty due to fluid compressibility. Electromagnetic linear motors are mechanical devices in which a stator and a rotor of rotary motors are linearly deployed, and generate linear motion instead of rotational motion. They have no bearings and are simple in structure and they are used as weapons, maglev trains, aircraft launching and mass drivers for spacecraft propulsion. In the field of robotics, the combination of the rotary electromagnetic motor with a reduction gear and ball screw is more preferred because of their design flexibility. They consist of rigid components without softness, but generally can make the stator hollow and have a large stroke depending on the length of the shaft.

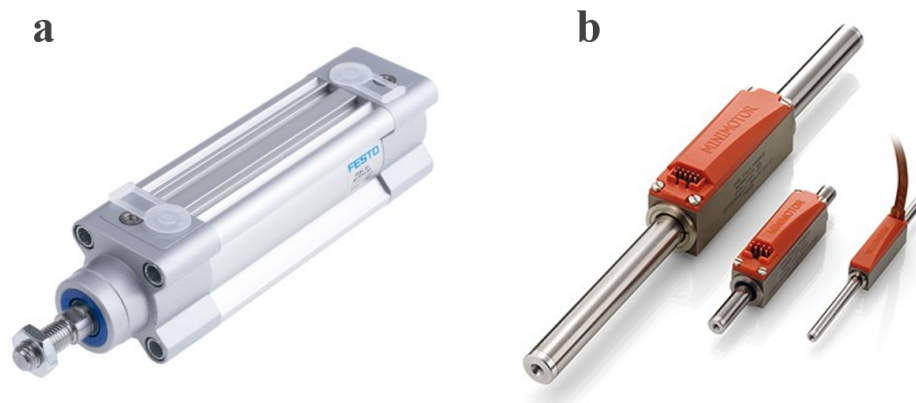


Fig. 1.2 Rigid linear actuators. (a) Fluidic cylinder and (b) electromagnetic linear motor (refer to <https://www.micromo.com/> and <https://uk.rs-online.com/web/>).

1.2.2 Soft Expansion/Contraction Actuators

Soft actuation as shown in Fig. 1.1 (c) can be categorized into three types (Fig. 1.3): variable length tendon [34], fluidic elastomer actuators (FEAs) [35], and electro-active polymers (EAPs) [36]. Variable-length tendon actuators including wire-driven and SMA are typically embedded in soft segments, and change the length of the cable by winding or shortening to create motions [37, 38]. Wire-driven, which is an exception among soft actuators, is an easy-to-control drive system due to the use of conventional rotary motors in external platform for actuation. However, since wire-driven robots can generate force only in the pulling

direction, they need a restoring force by springs or their soft body to return to their original shape. SMA is an actuator that can memories and recover its original shape, after heated over its transformation temperature. SMA actuators actuated electrically by Joule heating are lightweight and powerful, and require no additional mechanical components. From these excellent features, they are used for various soft robots to replicate the functionality of muscular structure [39, 40], but their small strain and slow response time are restricted for their applications.

Fluidic elastomer actuators (FEAs) are the most prevalent soft actuators, which inflate channels within the soft body to deform the structure in a controlled manner. They can generate various motions such as bending and twisting from expansion/contraction motions by adding inextensible constraints such as cloth, paper, plastics, fiber and even stiffer rubbers. There can be many sub-groups of actuators under the FEA-type such as pneumatic artificial muscles (PAMs) [41, 42], soft pneumatic actuators (SPAs) [43, 44] and flexible-fluidic actuators (FFAs) [45, 46]. They are highly scalable and less complex to product by using casting, soft-lithography, and multi-material 3D printing [47]. These fabrication tools allow soft robots to be combined composites with heterogenous materials, embedded electronics, and internal channels for actuation. A large challenge for FEAs is portable power sources for actuation. With a few recent and very notable exceptions [48–50], fluidic power sources are heavy and bulky, restricting mobility and making miniaturization difficult.

Electro-active polymers (EAPs) are polymer-based actuators that generate a change in size or shape when stimulated by an electric field [51]. They are low weight and have fracture tolerance, pliability, and relatively large actuation strain, which are suitable for soft robot actuation. Besides actuators, EAPs can be used as sensors, electronic components, and energy harvesting devices. EAPs are classified based on the driving principle into two categories: electronic EAPs and ionic EAPs. Electronic EAPs, which are actuated by applied electric fields and Coulomb forces, have a large strains and rapid response time (mSec order) but require high voltages for actuation (~ 150 MV/m). Ionic EAPs, which are driven by the migration of ions or molecules, work at low voltages (less than 5 V) but usually are used as bending actuators. Most of them can work only in wet conditions.

1.2.3 Flexible Linear Motors

Actuators classified in Fig. 1.1 are generally not known and rarely have been studied [31–33]. We named them "flexible linear motors", which are defined as motors that consist of a stator and a flexible shaft that moves linearly via changes of a relative position to the stator. Flexible linear motors are clearly different from conventional soft actuators that change their shape by internal stress. There would be three possible benefits if flexible linear motors were realized.

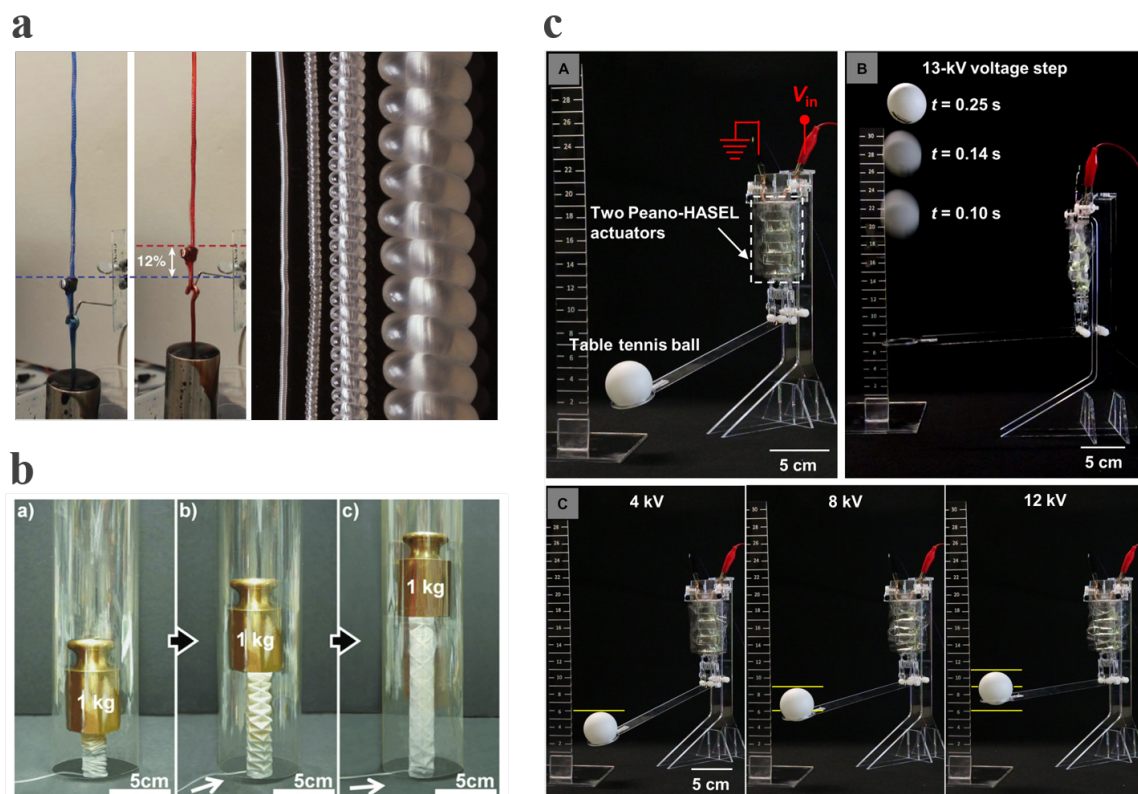


Fig. 1.3 Three typical types of soft actuators. (a) Variable-length tendon [34], (b) fluidic elastomer actuator (FEA) [35], (c) electro-active polymer (EAP) [36].

First, the motors can use an attractive driving principle. For driving sources, traditional rigid motors use piezoelectric effects and electromagnetic forces that are easy to control, while soft actuators mainly use compressed air and heat that are difficult to control. Furthermore, the former has good response time and high resolution. Flexible linear motors with a stator based on conventional motors would inherit these excellent features. Second, the motors can obtain a large stroke regardless of the shaft material. Soft actuators can only produce a limited stroke depending on the fracture resistance and stiffness of their material because of their driving principle. On the other hand, traditional motors with a hollow stator would have a large stroke depends on the shaft length because the energy for driving such as vibrations and electromagnetic forces is applied from the stator. Third, the motors can attach multiple stators on one shaft. This implies that motor output would be increased according to the number of stators. As an example of a use of multiple stators, take for instance continuum robots that have a flexible and elongated body: a continuum robot that has several backbones, or flexible shafts, would be able to have multi driving units with two or more stators on the shaft axis (Fig. 1.5). This implies that the continuum robot can increase the degree of freedom (DoF) without the diameter increase.

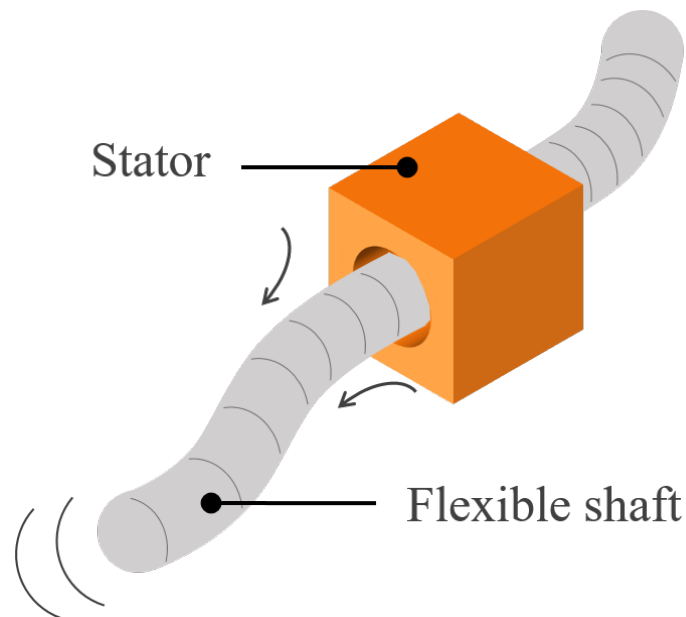


Fig. 1.4 Imaginary view of a flexible linear motor. A stator based on a conventional motor drives a flexible shaft lineary.

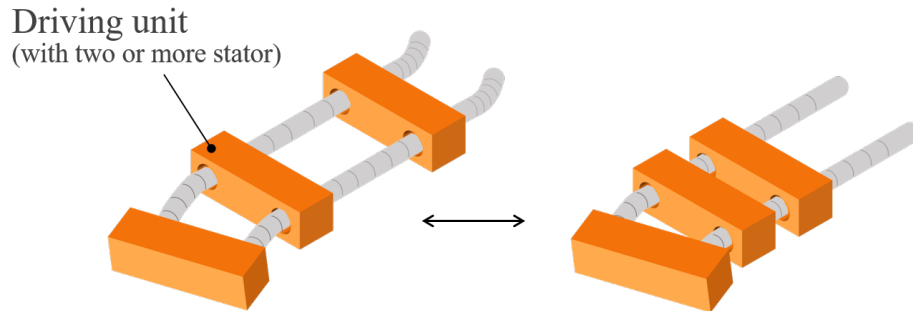


Fig. 1.5 Imaginary view of a continuum robot using flexible linear motors. Several driving units with two or more stators move along the flexible tubes. Changing the lengths of the flexible tube between each driving unit allows the robot to elongate and bend significantly.

1.3 Specific Applications

The previous subsection described the advantages of flexible linear motors, but the specific application is still unknown. Here, we will explain the background of the continuum robots for the application.

1.3.1 Pipeline Inspection Robot

Continuum robots that can access hard-to-reach targets in unpredictable environments have a wide range of potential applications from rescue to medicine [47, 14]. For example, a typical place where continuum robots apply is the pipeline which is long, narrow, and has significant curvature. A flexible and elongated continuum robot goes inside the pipe via small opening and enables the inspection and subsequent repair activity.

With the increase in the expectation of such continuum robots, many hardware designs have been proposed and demonstrated. The important characteristics of these robots to explore deeper and inaccessible sites are flexibility and stroke. High flexibility is necessary to conform to surroundings. A long stroke expands reachable work areas and increases the locomotion speed. One challenge of continuum robot design is to have both high flexibility and long stroke in the elongated body. However, it is difficult to have both the characteristics because the designable space inside the elongated tube robots is limited.

A remarkable development in recent years has been the proposal of continuum robots that can achieve significant growth of several 1000% [52, 53]. They consist of multiple expandable balloons, which provide manipulation by varying the amount of air in the balloon. However, they are completely fixed to the ground and cannot move around. Locomotion is often essential for navigating substantially long and narrow environments and accessing remote locations. The most commonly used locomotion in pipe inspection robots is based on

earthworms [54, 55]. Earthworm robots have a plurality of segments and move through a narrow conduit by sequentially stretching or contracting each segment. Many robots have only the ability to go straight [56, 57], but some exceptions allow for selective branching. However, they suffer from low speed movement.

1.3.2 Climbing Robot

Climbing robots have a wide range of potential applications, including building inspection, maintenance, construction, and search and rescue tasks [58–61]. A challenging problem in climbing robots is increasing reachability to navigate and transition between obstacles such as steps and walls. Most climbing robots are yet to achieve such tasks, whereas soft-bodied animals such as leeches, slugs, and caterpillars easily complete them. One strategy often observed in such organisms is the exploitation of large deformations and, therefore, nonlinearities to increase reachability.

Some traditional rigid robots that can climb at many angles and transition from wall to wall have been demonstrated [62–66]. However, since all climbing robots are always at risk of falling from high altitudes, it is desirable for them to be as light and flexible (as the organisms are) for safety and survival. Unlike traditional climbing robots with rigid links, soft robots have great potential to interact with environments safely and adaptively [67]. Some soft climbing robots with extreme compliance have been reported [68–70], but they can only generate simple locomotion on the wall. Despite the difficulties of modeling and control of soft robots arising from the many degrees of freedom in such systems, a few recent and very notable exceptions partially overcame these difficulties.

Flippy [71] is a cable-driven continuum robot with two grippers attached to the ends. It can transition between interior planes in different orientations by bending its body 180°. While this locomotion enables transition motion without complex sensing or control, its stride is restricted and increases the risk of collision with obstacles. Treebot [32] has a continuum body that consists of three mechanical springs, and it can extend and bend in any direction by controlling the spring lengths. This provides a large working space and makes it possible to climb from a tree trunk to a branch. Treebot has superior maneuverability and adaptability, but the body deformation was only explored within the regime of deformations which was predicted by a constant curvature model, thus constraining the range of possible robot postures. It is still an open challenge to achieve a wall-to-wall transition in soft robots (or continuum robots) and to model and control large nonlinear deformations.

1.4 Objective

This thesis argues that the realization of a flexible linear motor can overcome many of the drawbacks of previous soft actuators. To support this argument, subsequent chapters studied the proposal, model, performance, sensor, and control of flexible linear motors. The advantage of this approach that fuses rigid motors and soft actuators is to involve both features such as flexibility, robustness, large stroke, precise control, and electrically-driven. Explicitly enumeration the objectives:

- Proposal of flexible linear motors. To achieve a realization of the motors, two flexible linear motors based on the electromagnetic and piezoelectric principles are proposed and built.
- Experiments of flexible linear motors. To evaluate these motors, we build models, measure the basic performance, and consider sensor and control.
- Robot implementation of flexible linear motors. To demonstrate the advantages of these motors for soft robots, especially continuum robots, robots embedded these motors are built and tested.

1.5 Thesis Organization

This thesis comprises four chapters. This chapter introduces the concept of the flexible linear motor and the main body of literature related to soft robots and linear actuators. We show the benefits obtained from the realization of flexible linear motors and the goal and approach of this research. Chapters 2 and 3 propose two flexible linear motors: flexible ultrasonic motor and flexible rack pinion actuator, respectively. Table 1.1 sums up the characteristics and capabilities of each flexible linear motor. The former is advantageous for miniaturization, and the latter is easy to make multiple degrees of freedom (DoF) robot due to a simple driving circuit. Chapter 2 investigates the effect of inserting a slightly flexible shaft on the ultrasonic motor as a preliminary step in creating the flexible ultrasonic motor. After verifying experiments of the hard shaft, the flexible ultrasonic motor is built which has a flexible and elongated coil spring as the drive shaft. We formulate the pre-pressure and motion model of the coil spring to clarify the design methodology of the flexible ultrasonic motor. Experiments including when the motor moves under a load, a bending constraint, and feedback control are tested. Moreover, we build a self-sensing sensor by regarding the coil spring as a variable resistance. We build a twin coil spring-based flexible ultrasonic motor prototype and demonstrate feedback control of planar motion based on the constant

Table 1.1 Characteristics of flexible linear motors

	Flexible ultrasonic motor	Flexible rack and pinion actuator
Power	< 0.5 N	> 10 N
Response	Starting time: 10ms Stopping time: 1ms	\simeq 100 ms
Efficiency	< 30 %	\simeq 90 %
Size	1–20 mm ³	> 25×30×50 mm ³
Power supply	High AC voltage: > 100 V _{p-p} High Frequency: > 20 kHz	Low DC voltage: < 24 V
Driving principle	Piezoelectric phenomenon	Electromagnetic phenomenon (with mechanical transmission)

curvature model. After having introduced the design and mechanism of the flexible rack pinion actuator, Chapter 3 presents a mobile continuum robot and soft climbing robot as their applications. To clarify how superior flexibility and stroke, the main advantages of flexible linear motors, contribute to manipulation and locomotion, these robots are modeled and are tested. Chapter 4 summarizes the outcomes of our studies and puts the results of the individual chapters. The concept of the flexible linear motor opens several ideas for future work.

Chapter 2

Flexible Ultrasonic Motor

This chapter will introduce a flexible ultrasonic motor as a first flexible linear motor. Although the main focus of this thesis is a linear motion of a flexible shaft, the flexible ultrasonic motor can not only translate but rotate, therefore we will also mention the rotary motion briefly. Section 2.1 introduces principles, features and applications of general ultrasonic motors. Section 2.2 presents the driving principle of a rotary-linear motor that is an ancestor of the flexible linear motor. Section 2.3 shows experiments of the ancestor motor that inserted a slightly flexible shaft as a preliminary step for the flexible ultrasonic motor. Section 2.4 builds the flexible linear motor and formulates the pre-pressure, position sensing, and motion model of the coil spring. In addition, the motor performance under various conditions is evaluated.

2.1 Ultrasonic Motor Overview

Ultrasonic motors are types of electro-driven motors that use mechanical vibrations in ultrasonic range (>20 kHz) as their driving principle [72–76]. AC voltages are applied to piezoelectric elements to generate expansion and contraction motions. The displacement of piezoelectric oscillations amplifies by the mechanical resonance of a stator. A rotor or slider pressed against the stator moves by receiving the vibration via a frictional force.

The first ultrasonic motor was put into practical use in 1986 [73]. Since then, ultrasonic motors have been used for autofocus system in camera lenses, head-rest control in cars, and calendar turning mechanism in watches. These adoptions are thanks to the excellent features of the ultrasonic motors shown below.

- High power/weight ratio
- High power at low speed

- High holding power at zero speed
- Quick response time
- Compact size and light weight
- Design flexibility
- Resistance to external magnetic fields or radiation

Despite these attractive features, necessity for a high frequency power supply, less durable due to friction drive, and thermal problem due to long-time driving have restricted their deployment.

2.2 Driving Principle

There are many type of the driving methods of ultrasonic motors including traveling wave type, standing wave type, mode rotation type, and multi-mode excitation type [77]. Here, we use travelling wave typed ultrasonic motor, which is the most commonly known. We particularly focus on a rotary-linear ultrasonic motor that has a very simple cube stator with a through hole [78, 79].

A schematic of the stator of the rotary-linear ultrasonic motor is shown in Fig. 2.1. Four plate piezoelectric elements are bonded on the four side of the cube made of phosphor bronze. Each piezoelectric has two silver electrodes polarized positive on one side. Totally, there are eight electrodes on the outside of the stator. The other side, a silver electrode polarized negative, conducts electrically to the metallic body and ground reference of power supply devices. Voltages are applied by the eight wires connected to the eight electrodes, respectively, as shown in Fig. 2.1. The four sides of the stator are labeled "A" to "D" clockwise, and the forward and backward directions are labeled " f " and " b ", in the axial direction, respectively. The voltages applied to all silver electrodes of the eight piezoelectric elements are named as " E_{Af} ", " E_{Ab} " to " E_{Db} ", " E_{Df} ".

2.2.1 Rotation

The stator of rotary-linear ultrasonic motor excites individual vibration modes for rotary and linear motions as the driving principle. The rotation is based on a vibration mode that excites three waves along the circumference of the through-hole (R3 mode) shown in Fig. 2.2. When a periodic force F_a acts on the top surface of the stator by piezoelectric effect, a standing wave R3 mode is generated. When the other periodic force F_b acts on the next surface

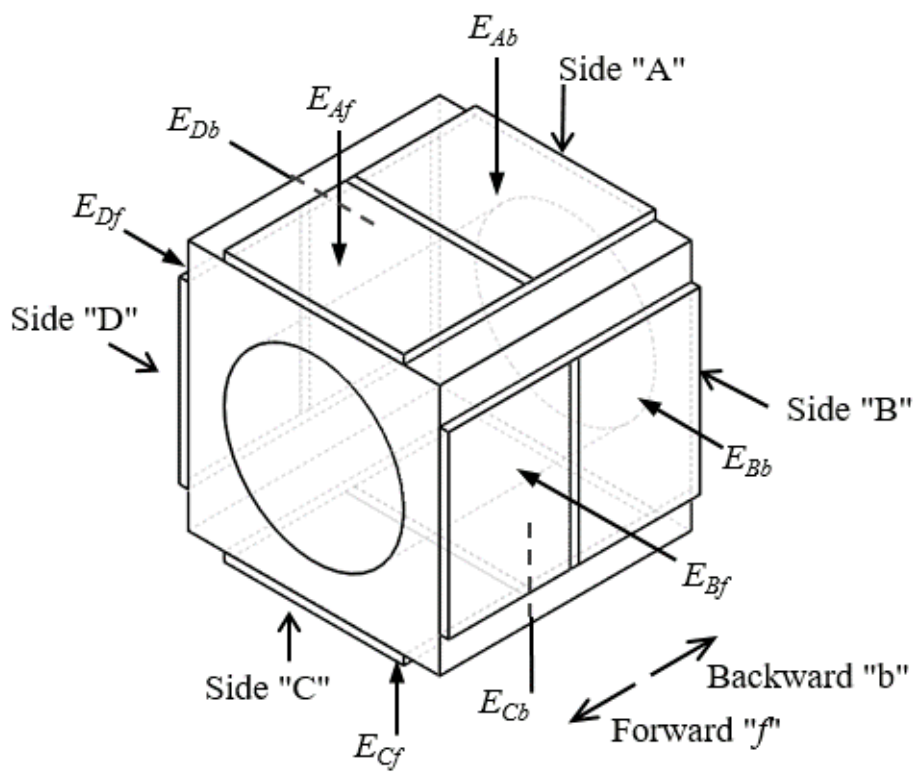


Fig. 2.1 Schematic of the stator and applied voltages

with 90 degrees, another R3 mode is excited. By generating these two R3 modes with the temporal phase difference of $\pi/2$ (one-quarter of a cycle) simultaneously, the travelling wave is produced on the inner surface of the through-hole (Fig. 2.3). While producing the traveling wave, elliptical motion is generated, and it moves the output shaft in the circumferential direction. This driving principle of the rotation is the same as that of the traveling type ultrasonic motor [80], although it appears different design. The voltages applied to all silver electrodes of the eight piezoelectric elements are named as " E_{Af} ", " E_{Ab} " to " E_{Db} ", " E_{Df} ". To generate rotation, four kinds of the voltages with phase shift of $\pi/2$ are applied:

$$E_{Af} = E_{Ab} = A_E \sin(2\pi f_E t) \quad (2.1)$$

$$E_{Bf} = E_{Bb} = A_E \sin(2\pi f_E t + \pi/2) \quad (2.2)$$

$$E_{Cf} = E_{Cb} = A_E \sin(2\pi f_E t + \pi) \quad (2.3)$$

$$E_{Df} = E_{Db} = A_E \sin(2\pi f_E t + 3\pi/2) \quad (2.4)$$

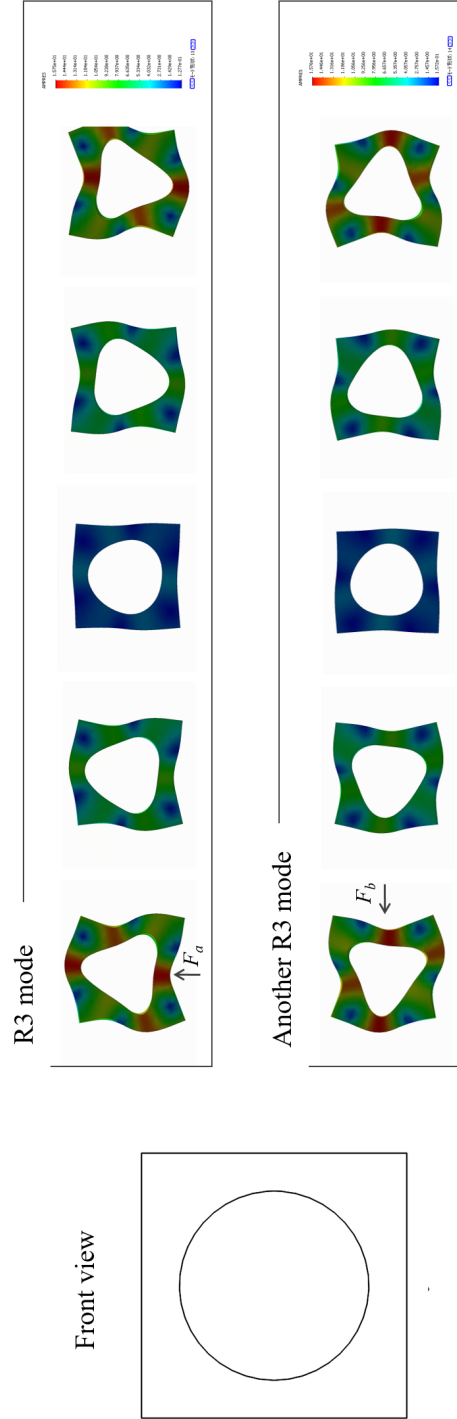


Fig. 2.2 Vibration modes for rotation. The stator generates three waves around the hole (R3 mode).

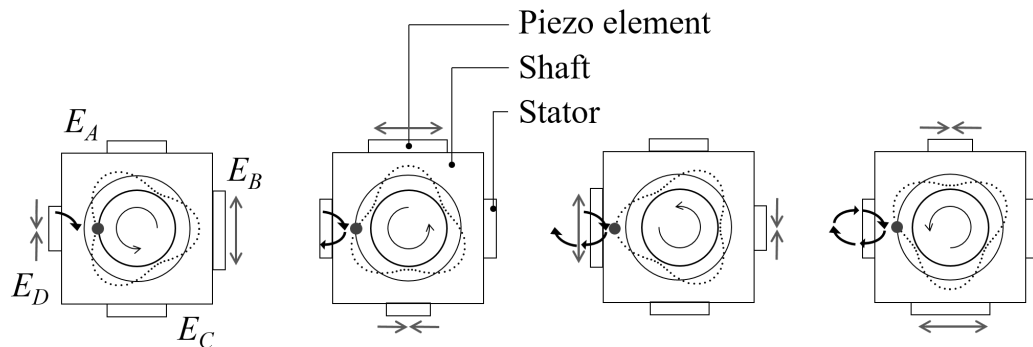


Fig. 2.3 Generation of elliptical motions for rotation. When R3 and another R3 modes are simultaneously excited, the stator generates an elliptical motion and moves a rotor

where A_E is the amplitude and f_E is the frequency of the applied voltages. When the frequency f_E is in the neighborhood of the natural frequency of R3 mode, the amplitude of the vibration is enhanced. This fact results in the production of a traveling wave with a large vibration amplitude.

2.2.2 Translation

The linear motion is generated by coupling the first extension mode (T1 mode) and the second extension mode (T2 mode) of the stator shown in Fig. 2.4. T1 mode is symmetry and the T2 mode is asymmetry with respect to the axial direction. When the stator design is cubic, the natural frequency of T1 mode and T2 mode are accorded. This fact has been verified by vibration analyses in existing literature [78, 80]. Giving the temporal phase difference $\pi/2$ between T1 mode and T2 mode, the inner surface of the stator generates an elliptical motion that moves the output shaft in the axial direction (Fig. 2.5). Such driving principle for the linear motion is well-known in linear ultrasonic motors [81, 82] and multi-degree of freedom ultrasonic motors [83, 84]. In these motors, combination of the first extension mode and the second bending mode is used as their driving principle. Modal analysis using finite element methods (FEM) clarifies mode shapes and natural frequencies of the stator. The material characteristics of the stator used in FEM model are the same as those of phosphor bronze. The stator shape is a single metallic cube with a side length of 14 mm and a through-hole of 10 mm in diameter. The modal analysis shows the mode shape of R3, T1, and T2 modes as shown in Fig. 2. The resultant R3 mode is excited at approximately 66.7 kHz. The resultant T1 and T2 modes are observed at 78.0 kHz and 77.5 kHz, respectively. To generate linear

motion, two kinds of voltages with phase of $\pi/2$ are applied:

$$E_{Af} = E_{Bf} = E_{Cf} = E_{Df} = A_E \sin(2\pi f_E t) \quad (2.5)$$

$$E_{Ab} = E_{Bb} = E_{Cb} = E_{Db} = A_E \sin(2\pi f_E t + \pi/2) \quad (2.6)$$

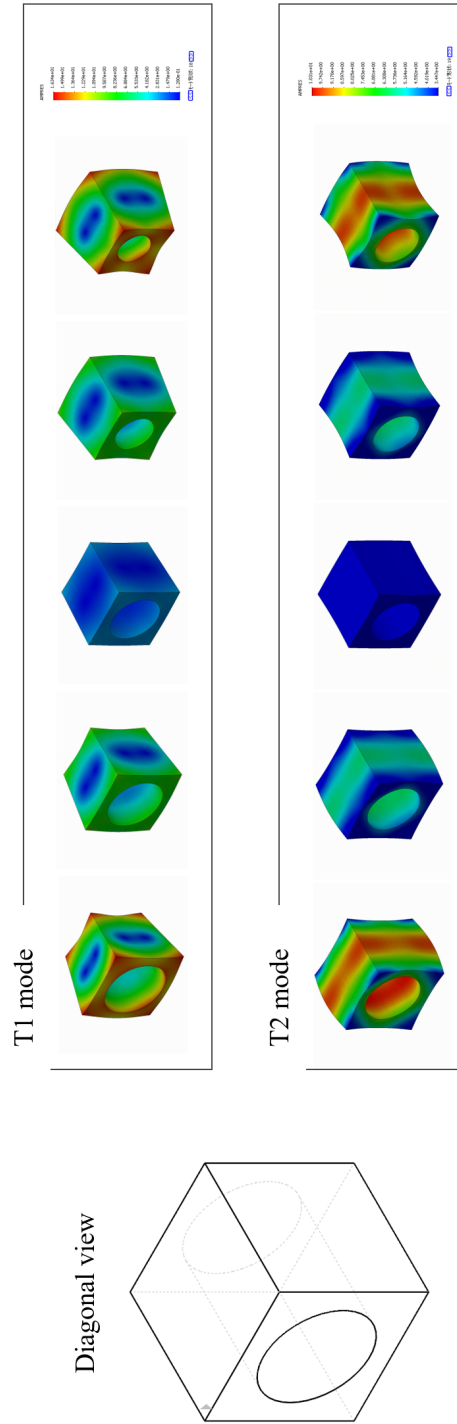


Fig. 2.4 Vibration modes for translation. The stator generates T1 and T2 modes.

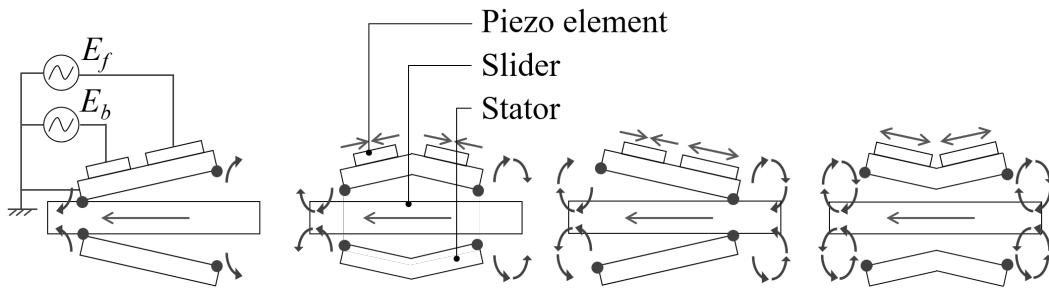


Fig. 2.5 Generation of elliptical motions for translation. When T1 and T2 modes are simultaneously excited, the stator generates an elliptical motion and moves a shaft.

2.3 Ancestor of Flexible Ultrasonic Motor

This subchapter introduces a rotary-linear ultrasonic motor as an ancestor of the flexible ultrasonic motor. Since ultrasonic motors are actuators that transmit vibrations to a hard shaft by friction, it is challenging to operate a very flexible shaft. Therefore, moving a slightly flexible shaft is the starting point for this study. We focus on a rotary linear motion ultrasonic motor with a simple structure. The stator comprises of a single metallic cube with a through-hole, and the output shafts inserted to the hole generates motions in both its circumferential and axial directions arbitrarily. The ultrasonic motor requires the pre-pressure between the slider and shaft for improving the output. In this subchapter, two ideas for optimizing pre-pressure by the output shafts are examined. First idea is a cylinder shaft with micron-order accuracy in its diameter. The cylinder shaft contacts the whole inner surface of the stator and generates pre-pressure between the stator and the shaft. The other idea is a spring shaft having slightly larger diameter than the stator hole. It expands in the radial direction and generates the pre-pressure. The former is completely rigid, while the latter is slightly flexible.

2.3.1 Stator Characteristics

Prototype

The stator consists of a metallic cube and four piezoelectric plates on its four sides (Fig. 2.6). The cube, made of phosphor bronze, has a side length of 14 mm and a hole of 10 mm. Nickel plating is coated inside the hole to reduce wear. In the neighborhood of a corner of the stator, an internal thread of 1 mm in diameter is opened to connect to a ground line. Each piezoelectric plate with a length of 14 mm, a width of 10 mm, and a thickness of 0.5 mm, has

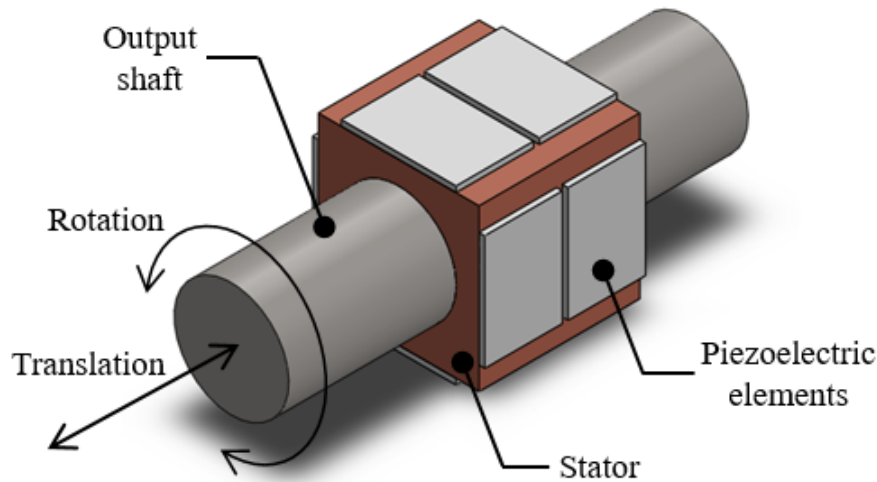


Fig. 2.6 Schematic of the rotary-linear ultrasonic motor.

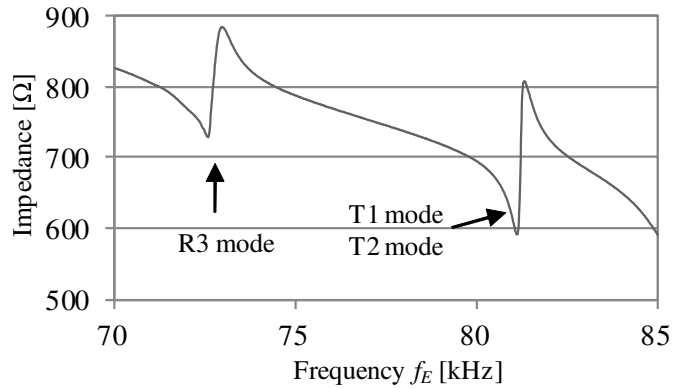
two silver electrodes on one side. The four piezoelectric plates are bonded using an epoxy adhesive (TB2280E, ThreeBond, Japan) at 120 °C for 2 hours.

Impedance Analysis

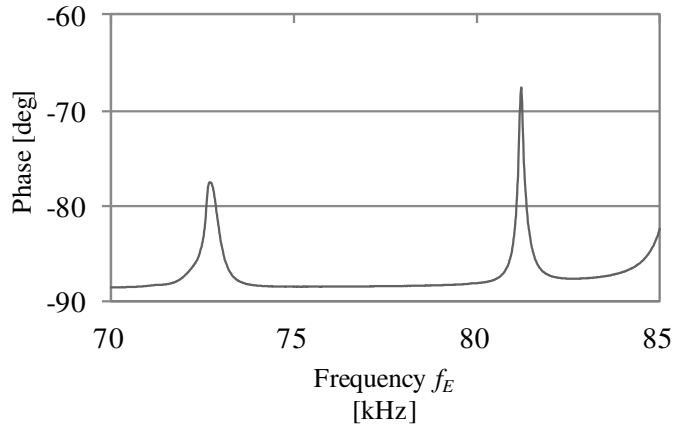
The resonant frequency of the prototype stator can be found by an impedance analyzer (IM3570, Hioki E. E. Co., Japan). A wire soldered to a piezoelectric element electrode and the ground wire from the metallic cube are connected to the impedance analyzer. The bottom of the stator is fixed with a flexible adhesive. Fig. 2.7 shows the frequency characteristics of the impedance and phase of the stator. A steep change in the impedance is observed at the frequency close to the frequency estimated as the R3, T1 and T2 modes. The resonant frequency of R3 mode is shown at approximately 73 kHz and T1 and T2 modes at about 81 kHz. These frequencies are slightly higher than the estimated frequency by the FEM modal analysis. It is due to that fixing the stator to a test bench increases the resonant frequencies.

Measurement of Vibration Amplitude

The shape of the vibration modes can be clarified by measuring vibration amplitude. A laser Doppler vibrometer (NLV2500-5, Polytec, Germany), which outputs the vibration velocity of a point, is used for the measurement. By integrating the vibration velocity, we can obtain



(a)



(b)

Fig. 2.7 Resonant frequency of the R3, T1, and T2 modes. (a) Impedance and (b) Phase.

the amplitude of the vibration. Two laser Doppler vibrometers LDV1 and LDV2 are installed to measure the inner surface and the end of the stator, respectively, as shown in Fig. 2.8. The laser from LDV1 is aligned with the axis of the stator hole. A rod mirror located into the stator hole reflects the laser orthogonally to the inner surface of the through-hole. This reflection enables to measure the radial vibration velocity. To define the position of the mirror, we denote ϕ the angle of the mirror and l_d the distance from the end of the stator to the center of the mirror. The other point that LDV2 measures is close to the stator hole at the end of metallic cube. The axial vibration amplitude of the stator is measured. By using these laser Doppler vibrometers and manipulating the rod mirror, the mode shapes and their vibration amplitudes are clarified.

The vibration amplitude of R3 mode is measured by rotating the mirror in the direction of ϕ . The gravity direction of the stator is defined as $\phi = 0$ degree. To focus on a single R3

mode, voltages expressed in Equations (2.1) and (2.3) are applied ($A_E = 120 \text{ V}_{\text{p-p}}$ and $f_E = 72.2 \text{ kHz}$) and voltages in Equations (2.2) and (2.4) are turned off. Fig. 2.9 (a) shows the vibration amplitude inside the through-hole of the stator measured by LDV1 when rotating the mirror. The result shows generation of three waves, in which the positive and negative are determined by the phase. The peak vibration amplitude of approximately $0.2 \mu\text{m}$ is obtained at the antinode of R3 mode. In fixing the angle ϕ , radial vibration amplitude is roughly constant regardless of the direction of l_d . During the vibration of R3 mode, the vibration amplitude of the stator edge measured by LDV2 is about $0.013 \mu\text{m}$.

The vibration amplitude of the stator excited by T1 and T2 modes is measured by displacing the mirror in the direction of l_d . The voltages in Equations (2.5) and (2.6) are applied ($A_E = 120 \text{ V}_{\text{p-p}}$ and $f_E = 81.0 \text{ kHz}$) to observe the vibration amplitude. Fig. 2.9 (b) shows the vibration amplitude measured by the LDV1 when the mirror is moved. The resultant vibration amplitude increases at the both end of the stator and it decreases at the center at where node of the T2 mode locates. The stator generates the peak vibration amplitude of approximately $2.16 \mu\text{m}$. The vibration amplitude measured by LDV2 is about $1.57 \mu\text{m}$, which is roughly equal to the amplitude of the center. Compared to the peak amplitude of R3 mode, the amplitude of T1 and T2 modes is more than ten times larger than the R3 mode.

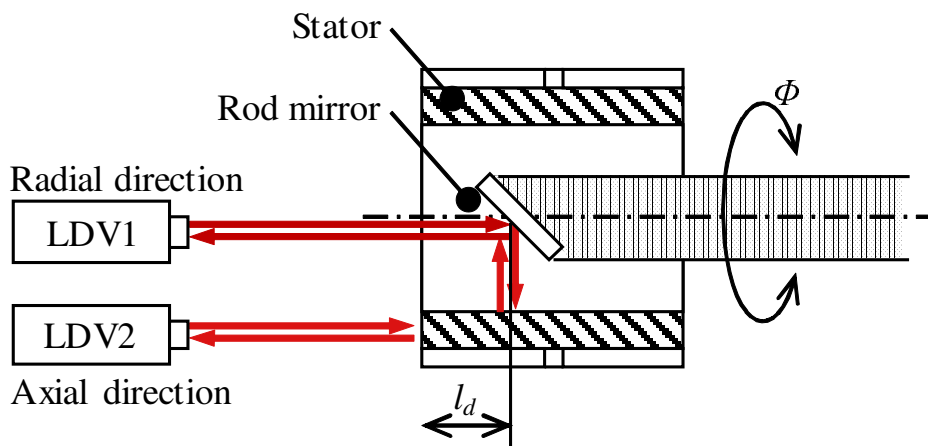
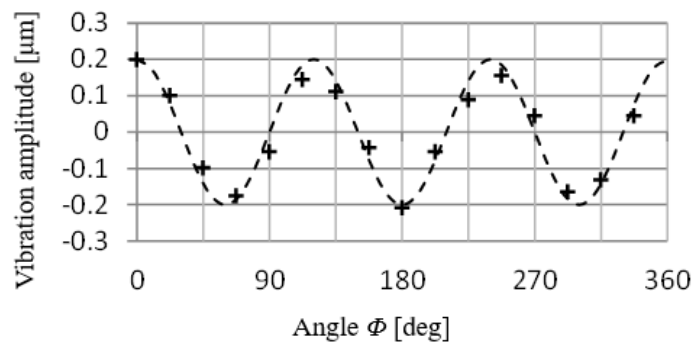
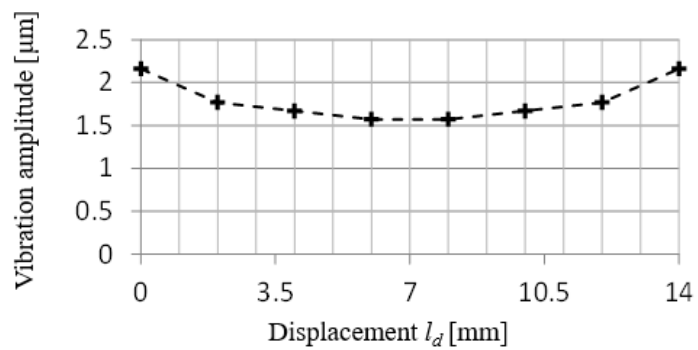


Fig. 2.8 Schematic diagram of the vibration measurement by laser Doppler vibrometer (LDV).



(a)



(b)

Fig. 2.9 Vibration amplitude of (a) R3 mode and (b) T1 and T2 modes. (a) In R3 mode, three waves are observed on the inner surface of the stator. (b) the vibration amplitude increases at the both end of the stator and it decreases at the center at where node of the T2 mode locates.

2.3.2 Pre-pressure Mechanisms and Experiments

Proposal of Two Output Shafts

We propose two output shafts with a pre-pressure generation mechanism to solve this problem by (i) adjusting clearance between a cylinder shaft and the stator hole and (ii) reducing a spring shaft to the stator diameter. Fig. 2.10 (a) shows a pre-pressure method using the cylinder shaft. The cylinder shaft made of carbon steel has a weight of approximately 30.8 g, and its weight becomes a pre-pressure between the stator and the shaft. To evaluate the contact of the cylinder shaft to the stator hole, let us denote d_c the diameter of the cylinder shaft. When the cylinder diameter is smaller than the stator hole diameter ($d_c < D$), the shaft contacts with only the bottom of the through-hole by gravity. When the cylinder diameter is equal to the stator diameter ($d_c = D$), the outer surface of the shaft contacts the whole inner surface of the stator, and this contact condition is ideal for both rotation and linear motion. When the cylinder diameter is larger than the stator diameter ($d_c > D$), the friction force between the stator and the shaft increases and prevents the motor motions.

Fig. 2.10 (b) shows the other pre-pressure method using the spring shaft, which is the same one as a closed coil spring. The spring shaft made of stainless steel has a diameter of d_s , weight of about 3 g, length of 30 mm and wire-diameter of 0.5 mm. When a moment is applied to the both ends of the spring shaft around the axial direction, the spring shaft is twisted and its diameter decreases. While the spring shaft diameter is smaller than the stator hole diameter by twisting, the shaft is inserted to the stator. When the applied moment is removed, the outer diameter of the shaft expands and contacts evenly to the inner circumferential surface of the stator. This is an ideal condition because the pre-pressure acts between the shaft and the stator without clearance. This pre-pressure can be optimized by choosing the spring shaft diameter: the pre-pressure increases at the larger spring diameters. Similarly to the cylinder shaft, if the pre-pressure is too large, the friction force prevents the motor motions. Fig. 2.11 (a) and (b) show the prototype motor with the cylinder shaft and the spring shaft, respectively.

Impedance Analysis when Inserted Shafts

We examine how impedance characteristics of the motor behave when the cylinder shafts and the spring shafts are inserted to the stator. The resonant frequency of R3 mode f_R and that of T1 and T2 modes f_T are clarified by the impedance analyzer.

Fig. 2.12 (a) and (b) show the behavior of the resonant frequencies f_R and f_T , respectively, in changing the cylinder shafts diameter with 1 μm accuracy. Several cylinder shafts are prepared for experiments as the output shaft. When the diameter of the cylinder shaft is

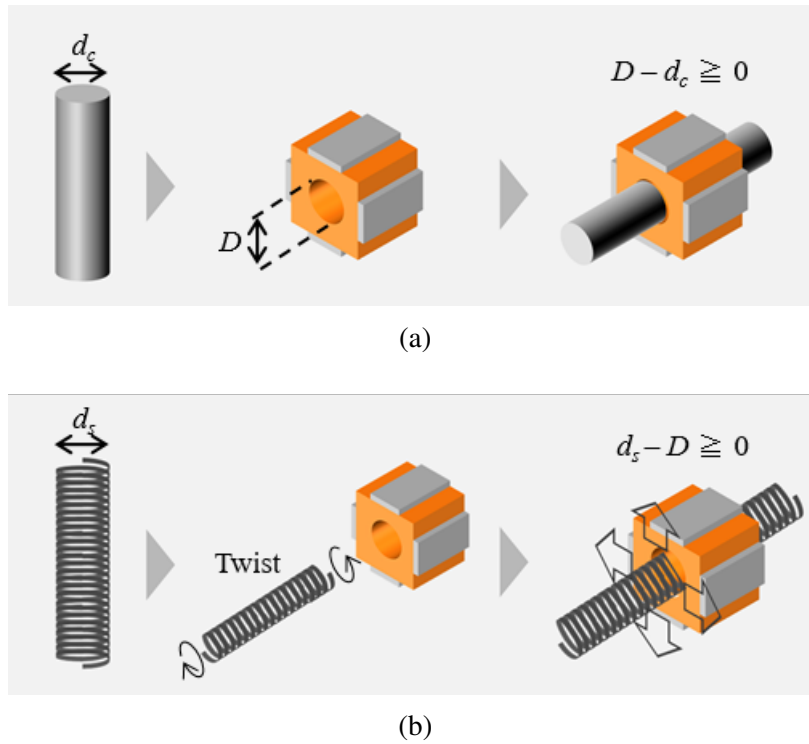


Fig. 2.10 Pre-pressure methods using (a) a cylinder shaft and (b) a spring shaft.

smaller than that of the stator hole, the shaft can be inserted to the stator hole smoothly. The clearance between the stator and the shaft decreases as the shaft diameter increases. When the shaft diameter is accorded with the stator hole, inserting the shaft into the hole needs a strong force. We determine this case as zero clearance. For evaluation of the cylinder shaft, we define clearance between the stator and the cylinder shafts $C_c (= D - d_c)$ as the subtraction of the cylinder diameter from the stator diameter. When the clearance C_c is smaller than $4 \mu\text{m}$, the both resonant frequencies sharply increase. This reveals that the outer diameter of the shaft contacts the inner circumferential surface of the stator without clearance. These resonant frequencies peak at $C_c = 1 \mu\text{m}$.

Fig. 2.12 (c) and (d) show the shift of the resonant frequencies in changing the spring shaft diameter, which is measured by a micrometer. The spring shaft is twisted to be inserted to the stator. The shaft diameter possible to be inserted without twisting is determined as zero clearance. This determination of the spring shaft clearance differs from that of the cylinder shaft. We define a reduction value of the spring diameter $R_s (= d_s - D)$ as the subtraction of the stator diameter from the spring diameter. Also, R_s is an amount of shrinkage in spring shaft of the radial direction. The resonance frequency stays constant regardless of the reduction value R_s . This is because the spring shaft is hollow and its mass is very small unlike the solid cylinder shaft.

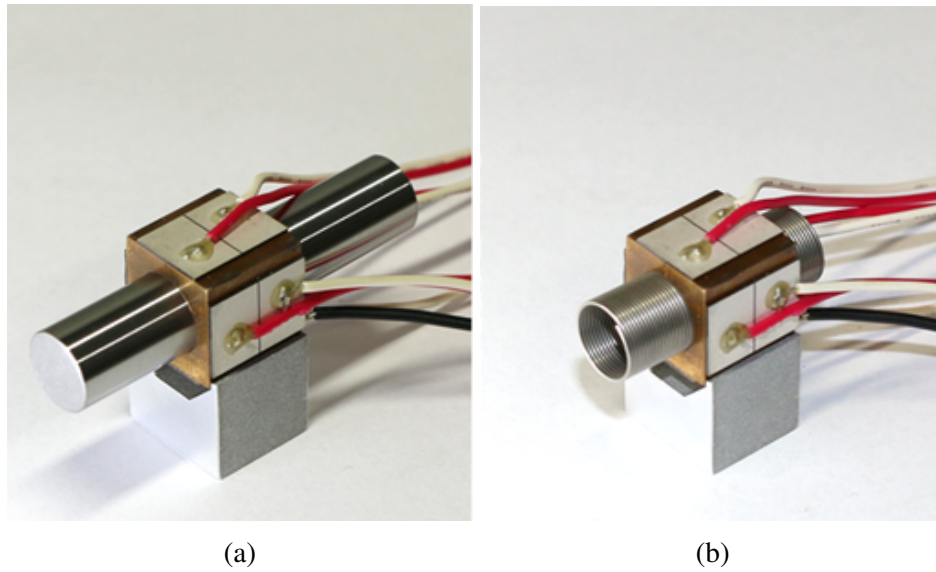


Fig. 2.11 Prototype motors with (a) the cylinder shaft and (b) the spring shaft.

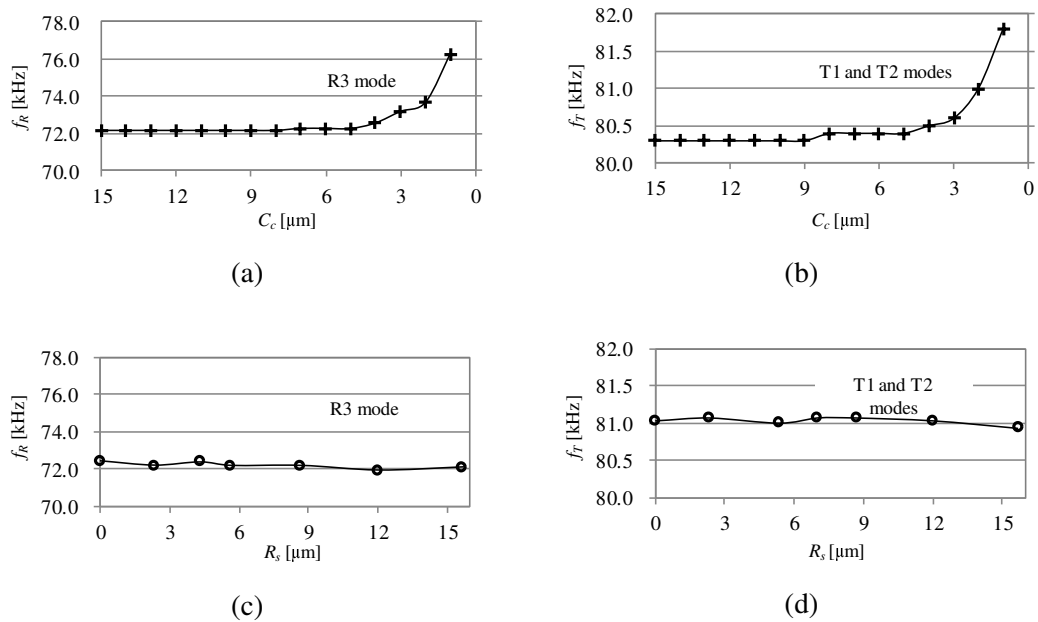


Fig. 2.12 Resonant frequencies in changing the shaft diameter. (a) R3 mode and (b) T1 and T2 modes in the cylinder shaft. (c) R3 mode and (d) T1 and T2 modes in the spring shaft. (C_c : the clearance between the stator and the cylinder shafts, f_R : the resonant frequency of the R3 mode, f_T : the resonant frequency of the T1 and T2 modes).

Torque and Thrust Force

Let us show how the clearance C_c and the reduction value R_s effect on the torque and thrust force of the rotary-linear ultrasonic motor. Fig. 2.13 shows experimental setup for measuring the torque and thrust force. The torque and thrust force are statically measured by a force gauge (ZP-20N, Imada Co., Japan). In Fig. 2.13 (a), an output shaft is attached to the spring shaft, and its torque is measured by the force gauge via a pulley. In Fig. 2.13 (b), the output shaft is attached to the spring shaft, and its thrust force is measured in axial direction. In the experiment, the amplitude of the voltages are constant ($A_E = 120 \text{ V}_{\text{p-p}}$), and the frequency f_E is adjusted to make the torque and force maximum. After the voltages are applied, heat generation occurs. The stator and the shafts expand according to a coefficient of thermal expansion. Influence of the heat generation can be ignored in this experiment because the change of the clearance is very small. Incidentally, if the temperature rises by 5°C , The change of the clearance between the stator (coefficient of thermal expansion $\alpha = 17\text{--}18 \times 10^{-6} \text{ K}^{-1}$) and the shafts ($\alpha = 11\text{--}18 \times 10^{-6} \text{ K}^{-1}$) is less than $0.35 \mu\text{m}$. Fig. 2.14 (a) and (b) show the relation of the maximum torque and thrust force to the clearance C_c . When the clearance is minimum ($C_c = 1 \mu\text{m}$), both the torque and the thrust force peak ($T = 3.6 \text{ mNm}$ and $F = 1.5 \text{ N}$). When there is no clearance ($C_c = 0 \mu\text{m}$), the motor cannot generate motions. It is due to that static friction is too large to drive the cylinder shaft. Fig. 2.14 (c) and (d) show the relation of the maximum torque and thrust force to the reduction value R_s . The peak torque of $T = 2.8 \text{ mNm}$ and peak thrust force of $F = 2.9 \text{ N}$ are obtained at $R_s = 5 \mu\text{m}$ and $R_s = 9 \mu\text{m}$, respectively.

We discuss a difference of the peak thrust forces values between the cylinder shaft and the spring shaft (Fig. 2.6 (b) and (d)). It is seen that the peak thrust force of the spring shaft is roughly twice larger than that of the cylinder shaft. This is because the spring shaft can adjust the pre-pressure value precisely and optimally by changing its diameter. In other words, it is insufficient to optimize the pre-pressure by the cylinder shaft with $1 \mu\text{m}$ accuracy. Another interesting aspect is that the spring shaft has a difference between the torque peak and the thrust force peak: the torque peaks at $R_s = 5 \mu\text{m}$ and the thrust force peaks at $R_s = 9 \mu\text{m}$ (Fig. 2.6 (a) and (b)). It is due to that the vibration amplitude of T1 and T2 modes is larger than that of R3 mode (Fig. 2.9). The motor can generate large thrust force with high vibration amplitude under the large pre-pressure, whereas a small pre-pressure with low vibration amplitude reduces the torque.

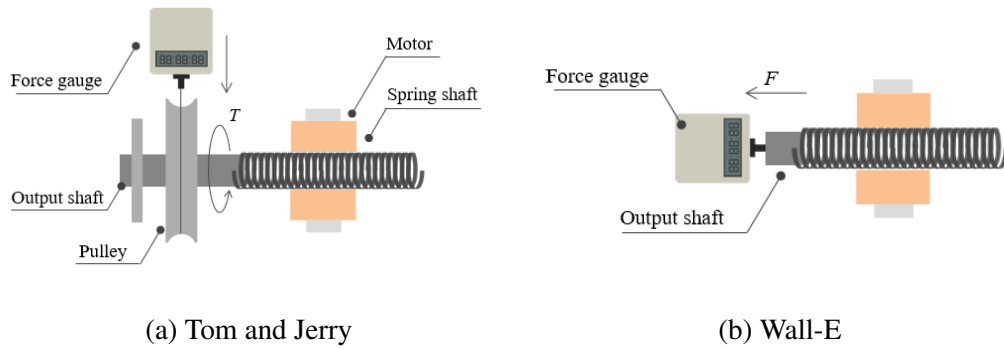


Fig. 2.13 Experimental setup for measuring (a) the torque and (b) the thrust force.

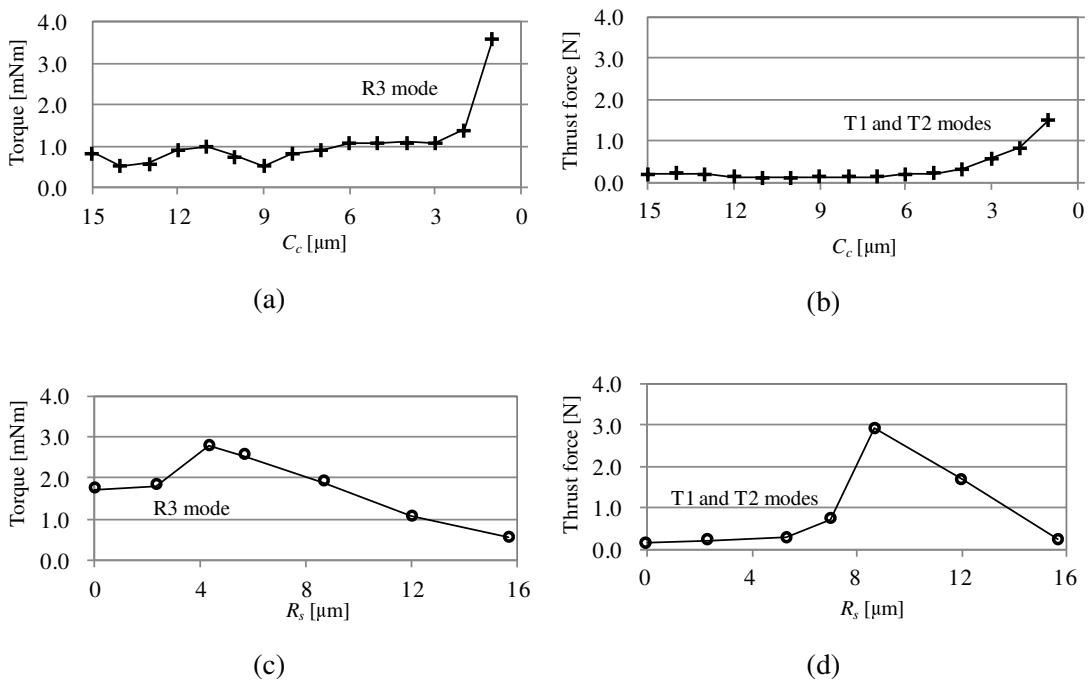
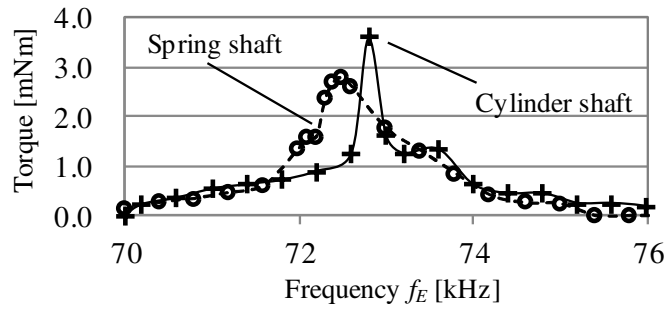
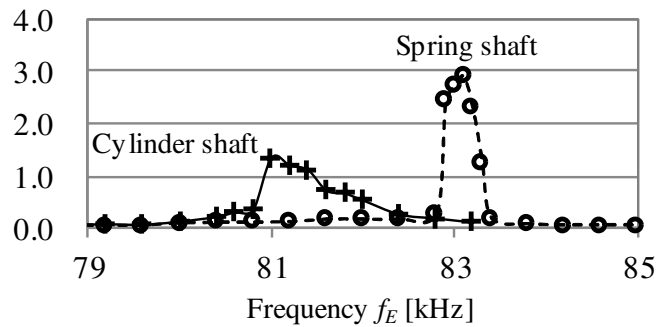


Fig. 2.14 Torque and thrust force in changing the shaft diameter. (a) R3 mode and (b) T1 and T2 modes in the cylinder shaft. (c) R3 mode and (d) T1 and T2 modes in the spring shaft.



(a)



(b)

Fig. 2.15 Relationship of torque and thrust force to the frequency of applied voltages: (a) torque and (b) thrust force.

Frequency Characteristic using the Optimal Diameters

Frequency characteristic of ultrasonic motors is important to be used for control of the torque and the thrust force. We examine the torque and thrust force of the rotary-linear ultrasonic motor by changing the frequency of the voltages at the constant amplitude $A_E = 120 \text{ V}_{p-p}$. Fig. 2.15 (a) shows the behavior of the maximum torque when the frequency is changed. The torque peaks in the neighborhood of the resonant frequency. The range of torque generation is 70-76 kHz in both the cylinder shaft and spring shaft. Fig. 2.15 (b) shows the frequency characteristic of the maximum thrust force. The range of thrust force is 79-83 kHz in the cylinder shaft and is 81-85 kHz in the spring shaft. The thrust force of the spring shafts peaks slightly higher frequency than that of the cylinder shaft. The resulting torque and thrust force are non-linear with respect to the change in the frequency.

2.3.3 Conclusion

The torque and thrust force have been improved by optimizing the diameter of the cylinder shafts and the spring shafts experimentally. Compared with the previous rotary-linear ultrasonic motor with the similar size of the stator when applying the same voltages [9], the maximum torque of the spring shaft is 1.5 times larger and that of the spring shaft is 1.2 times larger; the maximum thrust force of the cylinder shaft is 4.4 times larger and that of the spring shaft is 8.5 times larger. In the future, for larger torque and thrust force, there are several ideas such as coating the output shafts by an appropriate material with an optimal friction coefficient. The proposed spring shaft works well at the optimal pre-pressure. One of the advantages of using the spring shaft is the flexibility. Flexible robotics might be an interesting application of this motor.

2.4 Flexible Ultrasonic Motor Prototype

In the previous subchapter, we have succeeded to move the slightly flexible shaft and provide pre-pressure by changing the shaft diameter in the micron order. Here, we use a longer and more flexible coil spring to bring flexibility for the motor and enable a long stroke to access to deeper sites (Fig. 2.16). In addition, the long and flexible coil spring generates the pre-pressure with larger diameter shrinkage (millimeter order) and works as a position sensor by regarding itself as a variable resistance. We formulate the relation between the coil spring parameters and the pre-pressure to clarify the design methodology of the flexible ultrasonic motor. We model the linear motion of the coil spring by an equation of motion and compare it with the transient response by experiments. The performance under various loads or feedback loops is evaluated to study the characteristics of flexible ultrasonic motors.

2.4.1 Modeling

Design of the Coil Spring and Pre-Pressure

In the flexible ultrasonic motor that uses the friction drive as the principle, the most important parameter for optimizing its output is the pre-pressure between the stator and slider. The magnitude of the pre-pressure can be designed from the dimensions of the coil spring and the diameter of the stator hole. The coil spring slider is composed of a single metallic wire formed into a helix. It has a slightly larger diameter than the stator hole.

Fig. 2.17(a) shows an original coil spring and the coil spring inserted to the stator hole. The coil spring with an outer radius r_1 shrinks to the hole radius r_2 . The shrinkage of the

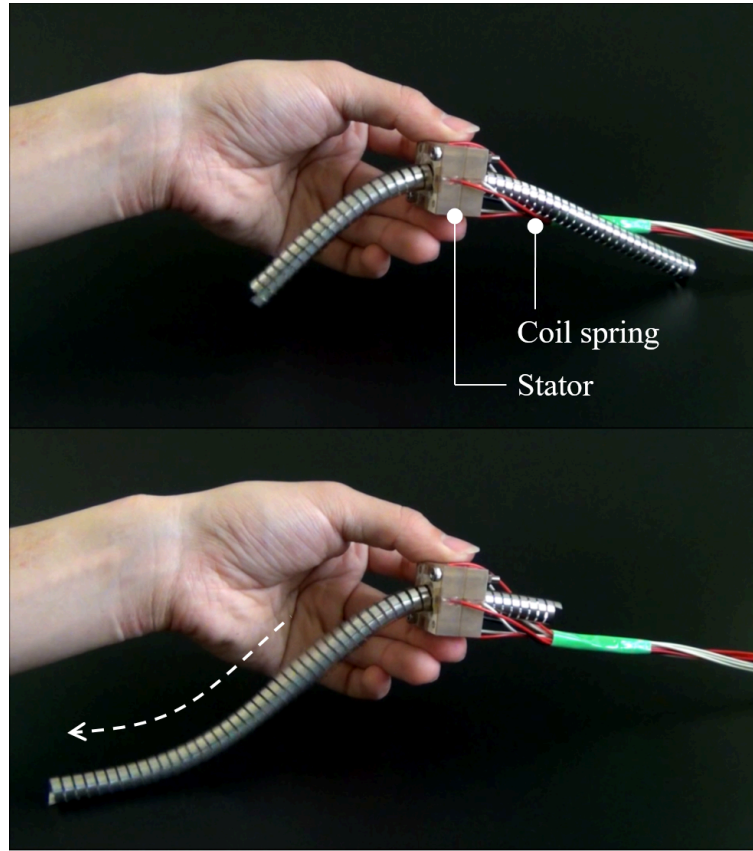


Fig. 2.16 Flexible ultrasonic motor. The coil spring inserted to the stator can move back and forth when voltages are applied.

outer radius is defined as $\Delta r (= r_1 - r_2)$. The coil spring has a rectangular cross-section with a width b and a thickness h , as shown in the detailed view in Fig. 2.17(a). The median centerline of the coil spring exists at the cross-section center vertically, and the median centerline length that spirals inside the stator hole is defined as L . In other words, L is the product of 2π , the radius r_2 , and the number of turns N between both the edges of the stator after the coil insertion:

$$L = 2\pi r_2 N \quad (2.7)$$

When the coil spring is inserted into the stator hole, the shrunk coil generates the pre-pressure P at the interface between the stator and the coil spring as shown in the right of Fig. 2.17 (a). To estimate the pre-pressure value from the coil's parameters, we consider two types of the elastic potential energy stored in the coil spring: strain energies by a shrinkage in the radial direction and by bending deformation. Assuming that these two energies take the same

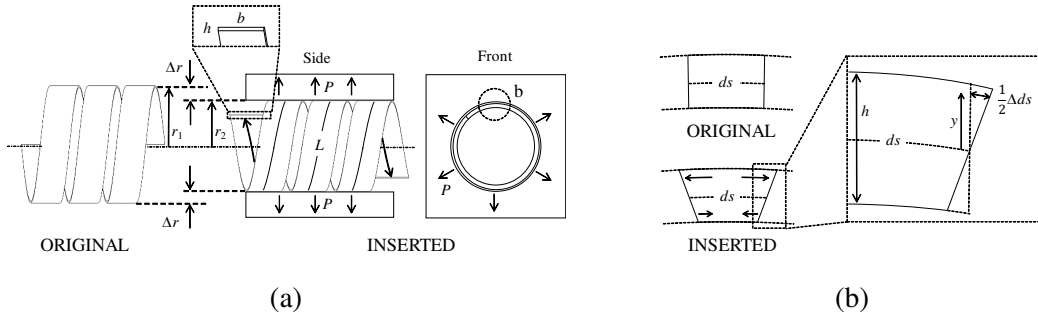


Fig. 2.17 Geometric relationship between the coil spring and the stator. (a) A coil spring with a slightly larger diameter than the stator hole diameter is inserted to the stator hole. The coil spring shrunk to the stator hole generates pre-pressure in the radial direction. (b) The detail of the deformation of a coil spring element. The cross section either lengthen or shorten, creating the strain.

value, we can estimate the pre-pressure using this equivalence. First, we consider the energy by the shrinkage in the radial direction. Deriving a rigid solution of the radial deformation is too complicated because the coil spring with a thick cross-section has a non-linearity. In addition, the shrinkage of the coil spring results in the radial and circular deformations. To simplify this radial deformation, we regard the coil spring as a cylinder with an unknown elastic coefficient. When the pressure P is applied in the radial direction, the coil spring shrinks with a displacement of Δr . The work done by the pressure is equivalent to the strain energy stored in the coil spring:

$$U = \frac{1}{2} P b L \Delta r \quad (2.8)$$

where the product of the width b and length L is similar to the outer surface area where the pressure acts. This is the energy stored by the radial shrinkage, and the pressure P is still unknown in (2.8). The pressure P can be estimated after the strain energy is solved from the bending deformation.

Second, we consider the bending deformation of the Euler–Bernoulli beam, which is well known in the mechanics of materials [85]. Fig. 2.17 (b) shows an element of the coil spring from the view of the axial direction of the stator hole. When the coil spring is inserted into the stator hole and bends, the upper part of the beam is in tension and the lower is in compression. In somewhere between the top and bottom, there is a neutral line, which is neither under tension nor compression. An elemental length of the neutral line that remains constant is defined as ds . Denoting the deformation at a distance y from the neutral line as Δds , the strain ϵ is determined as $\Delta ds/ds$ ($\epsilon = \Delta ds/ds$). The strain energy by the bending

deformation is the integral over the volume of the coil spring:

$$U = \int_V \frac{1}{2} E \varepsilon^2 dV = \frac{1}{2} E b L \int_{-h/2}^{h/2} \varepsilon^2 dy \quad (2.9)$$

where E is Young's modulus and the coil spring volume V is the product of b , h , and L . How the strain ε changes with y is geometrically determined when the dimensions of the coil spring and the inner radius of the stator hole are determined. The strain ε is expressed as

$$\varepsilon = \frac{\Delta r}{r_1 r_2} y \quad (2.10)$$

Substituting (2.10) into (2.9), the strain energy can be obtained. Hence, these equations (2.8)-(2.10) show the relation between the pre-pressure and the design parameters of the coil spring slider. The pre-pressure P can be estimated by substituting the energy U solved in (2.9) into (2.8).

Modeling of Translational Motion

We build a mechanical model to estimate the linear motion of the flexible ultrasonic motor. In general, the motion of the ultrasonic motors is expressed as a first-order lag system regardless of rotary and linear motions [86]. When the stator generates a force F and the slider translates with the velocity \dot{x} , the motion is expressed as

$$m\ddot{x} + c\dot{x} = F \quad (2.11)$$

where m is the mass of the slider and c is the damping coefficient. This damping coefficient is determined by the axial velocity of the elliptical motion generated by the stator [87]. This is the simplest model of the linear ultrasonic motor with a rigid slider.

In the flexible ultrasonic motor, the coil spring exists at both sides of the stator; therefore, the equation of motion must incorporate the spring components of the coil spring in addition to the above model. Fig. 2.18 shows the model of the flexible ultrasonic motor with a coil spring slider, both the sides of which are expressed as mechanical components: m_L , c_L , and k_L are mass, damper, and spring at left side, respectively, and m_R , c_R , and k_R are those at right side. The sum of m_R and m_L is the mass of the whole coil spring slider. The terms with c_L and c_R are mechanical loss in the coil spring, regardless of the stator's vibration. This model has three degrees of freedom with x_L , x , and x_R . When the stator generate a force F ,

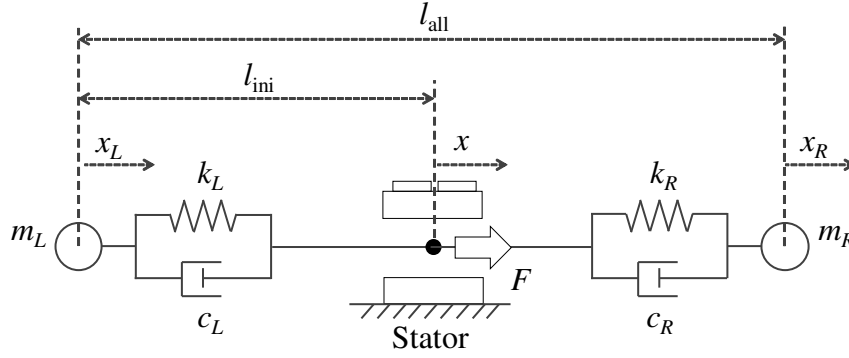


Fig. 2.18 A generalized model of the flexible ultrasonic motor, which is expressed as three-degrees of freedom system.

the motion of the coil spring can be expressed by the equation of motion:

$$\begin{bmatrix} m_L & 0 & 0 \\ 0 & 0 & 0 \\ 0 & 0 & m_R \end{bmatrix} \begin{bmatrix} \ddot{x}_L \\ \ddot{x} \\ \ddot{x}_R \end{bmatrix} + \begin{bmatrix} -c_L & c_L & 0 \\ -c_L & c_L + c_R & -c_R \\ 0 & c_R & -c_R \end{bmatrix} \begin{bmatrix} \dot{x}_L \\ \dot{x} \\ \dot{x}_R \end{bmatrix} + \begin{bmatrix} -k_L & k_L & 0 \\ -k_L & k_L + k_R & -k_R \\ 0 & k_R & -k_R \end{bmatrix} \begin{bmatrix} x_L \\ x \\ x_R \end{bmatrix} = \begin{bmatrix} 0 \\ F \\ 0 \end{bmatrix} \quad (2.12)$$

This three degrees of freedom model is usable at $x \cong 0$. i.e., the motion can be estimated when the displacement x is in the neighborhood of the stator position that generates a force F .

When the displacement x enlarges and the position that generates the force F is far from the stator ($x \gg 0$), the model (2.12) is not accorded to the actual. The stator is rigidly fixed in an experimental setup while the coil spring slider moves. In this case, the parameters of the coil spring slider change with the displacement x . Fig. 2.19 shows the right side of the stator when the displacement increases. Parameters at $x \gg 0$ are expressed using the prime symbol (') to distinguish from those of $x \cong 0$. The mass and the spring coefficient become a function of x . The mass m_R' is expressed as

$$m_R' = \frac{m}{l_{\text{all}}} (l_{\text{ini}} + x) \quad (2.13)$$

where m and l_{all} are the mass and length of the whole coil spring, respectively, l_{ini} is the initial length between the stator center and the coil spring end, defined in Fig. 2.18. The spring coefficient k_R' is

$$k_R' = 2l_{\text{all}} \frac{k}{l_{\text{ini}} + x} \quad (2.14)$$

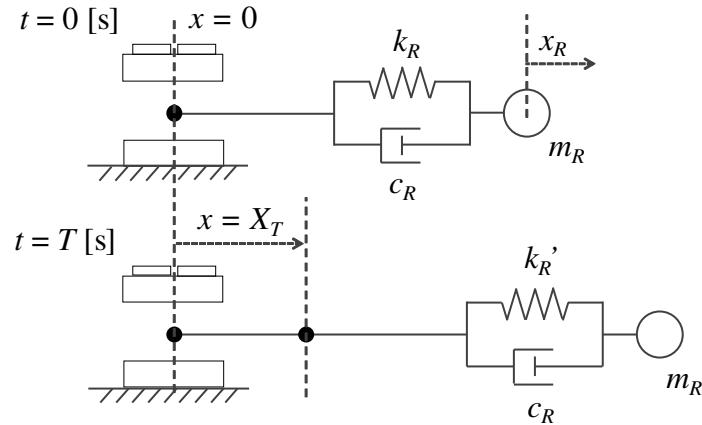


Fig. 2.19 A model at the right side of the coil spring. The mass and spring coefficient become variables of the displacement.

where k is the spring constant of the whole coil spring. There is a damping coefficient, but it can be regarded as constant because its change is small. When the stator generates a force F , the displacement x occurs. Regarding that the behavior of the displacement x is independent of the motion of the masses, the displacement x can be simply estimated from the axial velocity of the elliptical motion. The relationship between displacements x and x_R' is expressed by the equation of motion with the variable mass and spring coefficient as follow.

$$m_R' \ddot{x}_R + c_R(\dot{x} - \dot{x}_R) + k_R'(x - x_R) = 0 \quad (2.15)$$

The motion at the left side in the model can be estimated by replacing index R with L in (2.13) to (2.15).

The natural angular frequency of the coil spring depends on length of the coil at both the sides of the stator. Seeing the right side from the stator, the natural angular frequency is described as

$$\omega = \sqrt{\frac{k_R'}{m_R'}} \quad (2.16)$$

This equation shows that the natural angular frequency decreases at larger displacements; that is, an end of the coil spring vibrates slowly as it moves away from the stator.

2.4.2 Static Evaluation

Prototype of the Stator

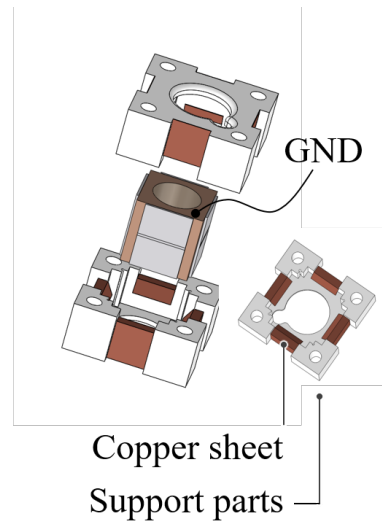
We use almost the same stator as used in section 2.3. The size of the stator and piezoelectric element is the same, but nickel plating is coated inside the hole to reduce wear. We use almost the same stator as used in section 2.3. The size of the stator and piezoelectric element is the same, but nickel plating is coated inside the hole to reduce wear. We build a support part to facilitate the connection of the stator wiring as shown in Fig. 2.20. The support part has four copper sheets to which four electrode wires are connected. When the stator is inserted into the support part, these sheets are elastically deformed and contacted to each piezoelectric element, making electricity flow for driving.

The resonances of the stator can be found by analyzing the frequency characteristics of admittance. To move the coil spring slider linearly, both the T1 and T2 modes should be simultaneously excited at the same driving frequency. We confirm that the two vibration modes exist at the same frequency by observing the admittance curve. The admittance and phase of the stator are measured by an impedance analyzer (IM3570, Hioki E. E. Corp., Nagano, Japan). Changing the connection between the stator and the impedance analyzer can clarify the existence of both T1 and T2 modes. The left of Fig. 2.21 (a) shows how to connect the piezoelectric plate electrodes to the analyzer. To excite T1 mode, the input voltage wire is connected to all eight electrodes of the piezoelectric plates, and the ground wire is connected to the metallic cube of the stator. When the voltage V_{in} is applied, all the piezoelectric plates repeat extension and contraction and generate T1 mode. On the other hand, to excite T2 mode, the input voltage is connected to the four electrodes at backward and the ground wire is connected to the other four electrodes at forward as shown in the right of Fig. 2.21 (a). In this case, when the backward extends, the forward contracts, or vice versa. The repetition of these extension and contraction generates T2 mode.

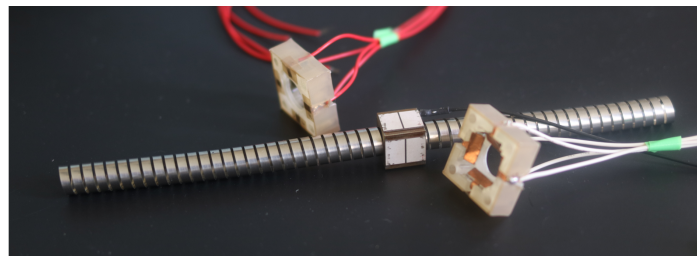
Fig. 2.21 (b) and (c) show the frequency response of the admittance and phase, respectively, in which the solid lines and dashed lines show T1 and T2 modes, respectively. The resonance of T1 and T2 modes is observed as a steep change at almost the same frequency at around 82.0 kHz. These figures show that the T1 and T2 modes can be excited at the same driving frequency. When two voltages described in (2.5) and (2.6) are applied at 82.0 kHz, the excitation of T1 and T2 generate a translation as shown in Fig. 2.5.

Relation between the Output and the Pre-pressure

The important characteristic of the proposed motor is how the motor output changes with respect to the pre-pressure. We experimentally clarify the relation of the pre-pressure with



(a)



(b)

Fig. 2.20 Support part for wiring. (a) CAD design and (b) Prototype of the support part

the thrust force and velocity generated by the motor. The coil spring model are given as a length $L = 94.2$ mm, width $b = 3$ mm, height (thickness) $h = 0.15$ mm, and Young's modulus $E = 196$ GPa. To change the pre-pressure, we insert several coil springs with different diameters ranging from 10 to 11 mm into the stator hole with a diameter of 10 mm. i.e., the coil spring with a larger diameter generates a large pre-pressure because the diameter of the stator hole is constant. The pre-pressure can be estimated from (2.8) after the strain energy is computed using (2.9). For example, when the coil spring diameter is 10 mm, the pre-pressure becomes zero. When a coil spring with a diameter of 11 mm is inserted into the stator hole, it generates a pre-pressure of $P = 0.036$ N/mm² and stores a strain energy of $U = 2.8$ mJ. (The strain energy is evaluated by the experiment shown in the Appendix). We can also change other design parameters of the coil spring to change the pre-pressure. However, we need to consider additional effects arising between the stator and the coil spring, for example, a coil spring with very small height or low Young's modulus possibly decreases the transmission efficiency of the vibration energy. In the experiments, the force is measured by a force gauge

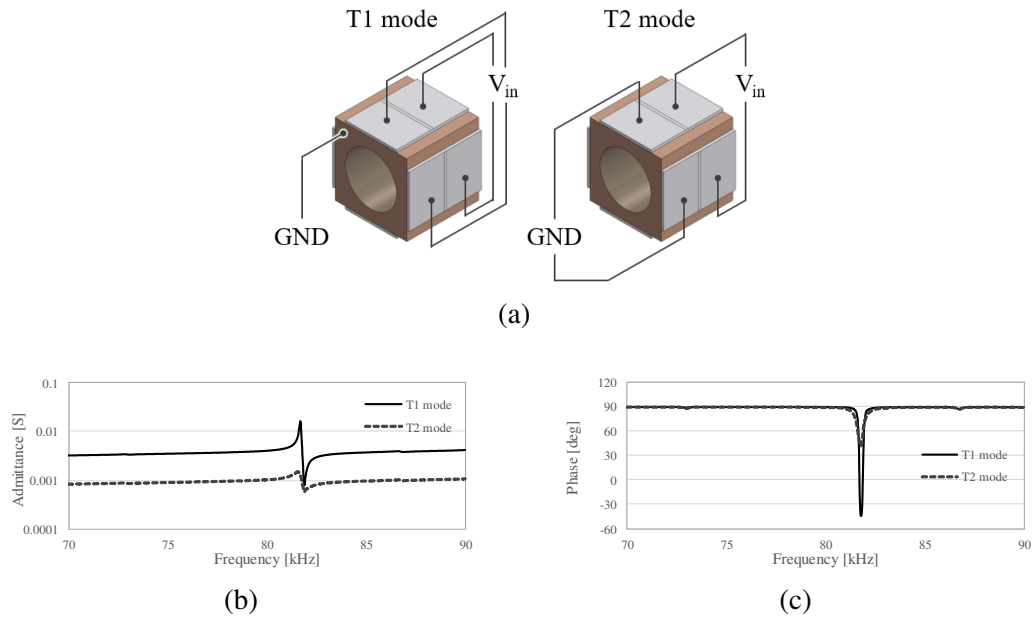


Fig. 2.21 Frequency response of the T1 and T2 modes. (a) Connection of the piezoelectric plates to the impedance analyzer. Frequency characteristic of (b) admittance and (c) phase. The result shows that T1 and T2 modes occur at the same resonant frequency.

(ZP-20N, Imada Co., Japan) attached to the end of the coil spring. The velocity is measured by a laser displacement sensor (ZX2-LD50, OMRON Corp., Kyoto, Japan) placed in the travelling direction of the coil spring.

In general, the velocity is calculated from the differentiation of the displacement, but estimating the motor velocity has large noise because the coil spring vibrates. We define the velocity from the displacement of the coil end after vibration and the period that the voltages apply. In this measurement, the transient time is ignored because the motor velocity peaks within a few milliseconds—the mass of the coil spring is much smaller than the output or brake force. During the experiments, the amplitude of the voltages is constant at $120 V_{p-p}$, and the frequency is adjusted to about 82 kHz to maximize the force and velocity. The optimum frequency has a slightly different value by coil springs because it depends on the pre-pressure value. For example, the optimum frequency at a coil diameter of 10.8 mm is 81.6 kHz, 0.2 kHz higher than the natural frequency at that of 10.15 mm.

Fig. 2.22 shows the behavior of the force and velocity when the pre-pressure varies. The force increases with the pre-pressure and peaks at 0.02 N/mm^2 (a coil diameter of 10.5 mm). A too large pre-pressure over 0.03 N/mm^2 (a coil diameter of 10.8 mm) decreases the force. On the other hand, the velocity is 200 mm/s at maximum, and decreases at higher pre-pressures. This is because a higher pre-pressure increases the friction at the stator-slider

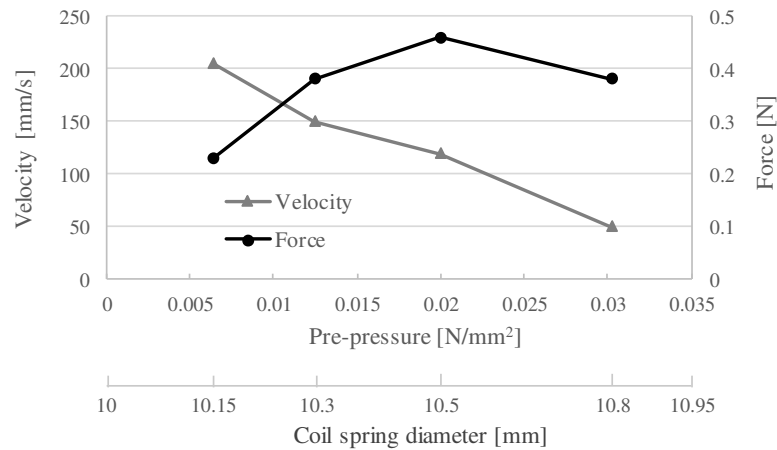


Fig. 2.22 Relation of the velocity and the force to pre-pressure. The pre-pressure is changed by using several coil springs with different diameters.

interface. Such a relation between the motor output and the pre-pressure has been seen in the pre-pressure characteristic of ultrasonic motors with a friction drive [88, 89].

Load Characteristic

The relation between the force and velocity is a fundamental characteristic of linear actuators. It can be seen by measuring the motion of a coil spring that lifts load attached to its end. Fig. 2.23 shows an experimental setup to examine the force–velocity curve. The coil spring that generates an optimal pre-pressure of 0.02 N/mm^2 is placed in the setup vertically. External weights are connected to the coil spring as load. Because the weight of the coil spring is approximately 6 g, the sum of the coil spring and the additional weights is the force generated by the motor. The velocity is measured by the laser displacement sensor while the coil spring moves upward with the weights. Fig. 2.24 shows the force-velocity curve when the weights change from 0 to 50 g. The velocity decreases as the load increases, and the motor cannot generate a motion over a load of 50 g. This behavior is roughly linear as with the load characteristic of other ultrasonic motors [86].

Relation to the Bending Radius of the Coil Spring

Another important characteristic of the proposed motor is its flexibility. Evaluating the flexibility should be to examine the motion of the coil spring curved by constraints and/or external forces. The top of Fig. 2.25 shows the experimental setup to clarify how the velocity of the coil spring behaves under constraints. The coil spring end is fixed to a rotary constraint component that transfers the linear motion of the coil spring into a motion around an arc

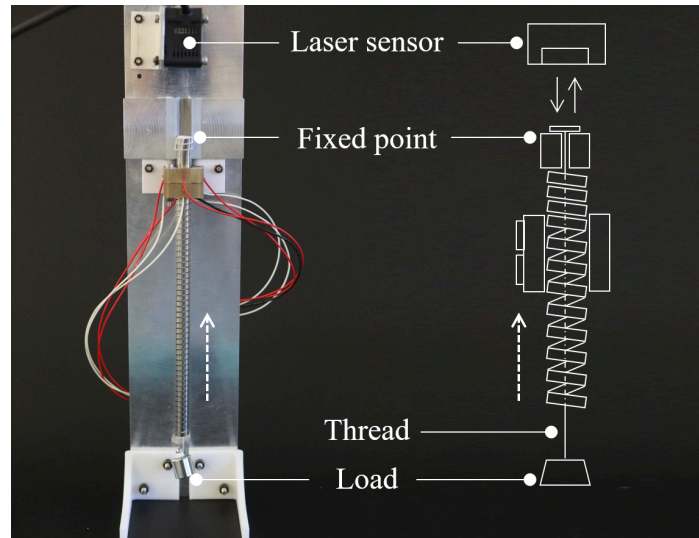


Fig. 2.23 Experimental setup for measuring the velocity when the flexible ultrasonic motor lifts a load. The coil spring slider moves upward in this experiment.

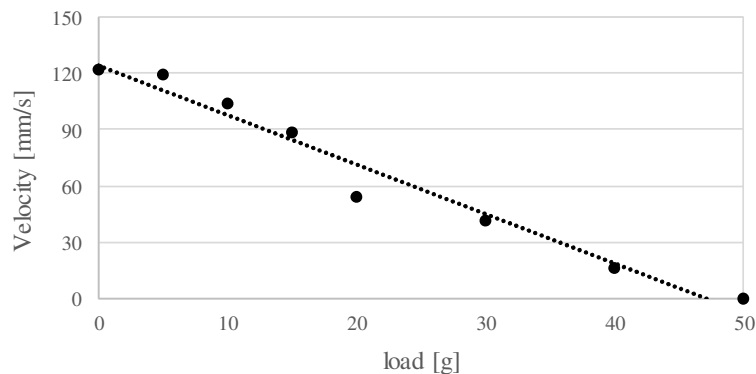


Fig. 2.24 Load characteristic of the flexible ultrasonic motor. It means a force-velocity curve.

trajectory with a radius R . As shown in the bottom of Fig. 2.25, when the motor generates a linear motion, the coil spring moves to the left side of the stator and bends by the rotary constraint. The distance between the rotary constraint center and the coil spring end is equal to the bending radius R of the rotary constraint. The bending radius can be changed in the experimental setup. The laser displacement sensor installed at the right side measures another end of the coil spring that moves away from the sensor linearly.

Fig. 2.26 shows the relation between the bending radius and the velocity when the bending radius varies from 55 to 15 mm. The result shows that the velocity is constant regardless of the bending radius—a smaller bending radius travels a shorter distance at less travelling time, and vice versa. This is because the velocity of the coil spring slider is determined by the steady-state vibration velocity of the stator in the friction drive [87]. Even at the

smallest bending radius of 15 mm, the motor can generate an average translation velocity. The bending radius of 15 mm is close to the limit of bending because smaller bending radii are over the range of elastic deformation.

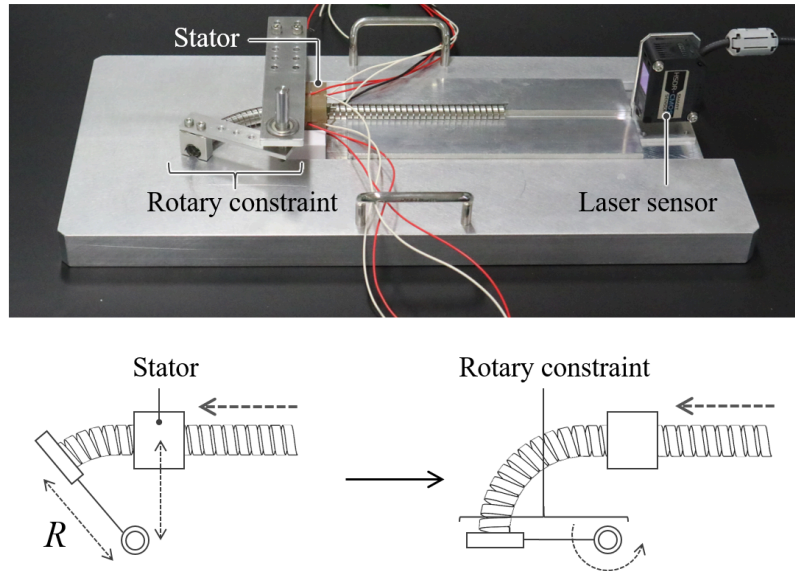


Fig. 2.25 Experimental setup to examine the relationship between the velocity and bending radius. The bending radius can be changed by the mechanical constraints.

2.4.3 Dynamic Evaluation

Step Response

We measure the step response of the flexible ultrasonic motor to show the vibration of the coil spring and verify the dynamic model by experiments. The experimental setup is the same as that without the rotary constraint component shown in Fig. 2.25. When the voltages are applied, the coil spring starts to move linearly. The displacement x with vibration is measured using the laser sensor. The vibration shown in the displacement x depends on the length of the coil spring, and the step responses are measured at the initial lengths l_{ini} of 40, 80, and 120 mm. The step responses are compared with the simulation. Assuming that the displacement x is independent of the vibration of the coil spring, the displacement x can be estimated from the coil spring's mass and the vibration velocity of the stator, as expressed in (2.11). The coil spring slider is supported by the experimental setup and is guided to move linearly, but a friction occurs by contact with the setup's base. A friction term $F_f = \mu m_R' g$ between the coil spring slider and the experimental setup is added in the left hand side of

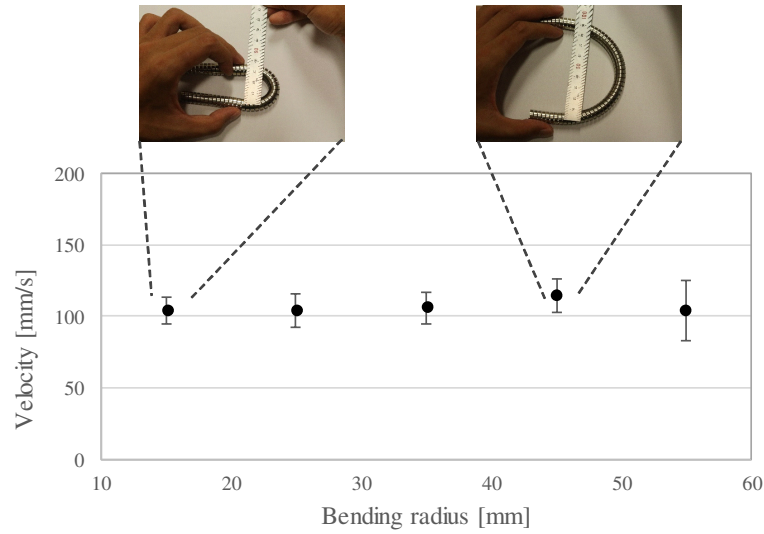


Fig. 2.26 The relationship between the velocity and bending radius (error bars indicate SD from 6 tests of one bending radius). The result shows that the velocity stays constant even if the coil spring is bent.

(2.15). When x is determined in (2.11), the motion of the coil spring end x_R' can be obtained in (2.15).

Fig. 2.27 shows the step responses when the control signal is on from time $t = 0$ to 50 ms. While the control signal is on, the voltages are applied to the motor from an external power source. In all responses, when $t = 50$ ms, the driving force generated in the stator stops, but the coil spring still has an elastic energy. After the input signal is off, the vibration of the coil spring remains for 0.1–0.2 seconds. The experimental step response is compared with the simulations. The model parameters for simulation are given in Table 2.1. The mass m , spring constant k and spring length l_{all} are determined from the design of the coil spring, and the damping coefficients c , c_R , and the friction coefficient μ are empirical. The motion of the coil spring is in agreement with the simulation. As the initial length l_{ini} shortens, the natural angular frequency increases as estimated in (2.16). This is because, at the short initial length, the mass m_R' reduces and spring constant k_R' enlarges. The natural angular frequencies of approximately 69, 100, and 201 rad/s, at the initial length l_{ini} of 120, 80, and 40 mm, respectively, are in agreement with the estimation.

2.4.4 Conclusion

In this paper, we demonstrated the first flexible ultrasonic motor using an elastic elongated coil spring. The proposed idea is the simplest way that provides a flexibility and a pre-pressure

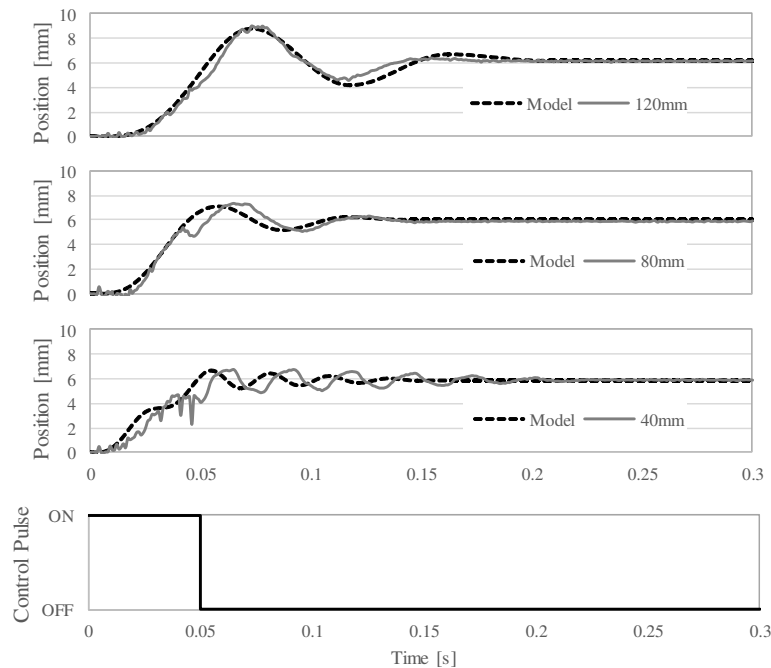


Fig. 2.27 Step response of the flexible ultrasonic motor when changing the initial length l_{ini} . The dashed and solid lines show the predicted result and the measured result, respectively.

because there is no additional mechanism. The experiments showed the sufficient flexibility under a mechanical constraint and an accordance between the model and experiments. Although only one example of the flexible ultrasonic motor is shown in this paper, the design strategy can be extended to the other designs for soft and flexible actuation technologies. In addition to the flexibility, this idea should be valuable as a simple pre-pressure mechanism for a rotary or linear motor with a rigid output shaft. Taking it into account that a typical advantage of ultrasonic motors is a high energy density, the pre-pressure mechanism has a potential to be miniaturized for narrow spaces, such as the inside of camera lenses and cell phones.

Our next step is the use of two or more flexible ultrasonic motors as a flexible and elongated continuum robot. Because the stator can generate a rotary motion, the combination of rotation and translation might be more attractive as a robotic application. Further investigation about contact problems at the stator-slider interface is important to generate a stable motion for controlling multiple flexible ultrasonic motors. Another study about a further miniaturization of the flexible ultrasonic motor might be required for smaller diameter continuum robots. We have achieved an ultrasonic motor that can generate both rotary and linear motions by the stator with a cube of 3.5 mm [79]. This miniaturization technology might be applied to build a medical continuum robot with smaller diameter. Another interesting aspect

Table 2.1 Model Properties of the Flexible Ultrasonic Motor

Symbol	Quantity	Value
m	Slider mass	0.006 kg
k	Spring constant	4.4 N/m
c	Damping coefficient	3.7 N·s/m
c_R	Damping coefficient	0.008 N·s/m
μ	Dynamic friction coefficient	0.24
l_{all}	Coil spring length	210 mm
F	Motor output	0.45 N

is an understanding contact between the stator and coil spring for stabilization and efficiency improvement. For example, when the coil spring moves linearly, the coil diameter increases and decreases sharply at both ends of the stator hole without a smooth slope. This can lead to unstable contact and reduced efficiency. Stator design optimization and dynamic contact modeling would approach this problem.

2.5 Twin-coil USM

In this chapter, we propose a twin coil spring-based continuum robot that can move forward and backward, and can bend left and right with flexibility and extensibility (Fig. 2.28). This is driven by two flexible ultrasonic motors, each consisting of a metallic stator and an elastic elongated coil spring. This robot has been named “Twin coil spring-based flexible ultrasonic motor (Twin-coil USM)”. The position of the end effector is determined by the positional relationship of the two coils and can be kinetically controlled with a constant curvature model. In the proposed actuator, the coil springs also act as resistive positional sensors. Changes in the resistance between the stator and the end of a coil are converted to a voltage and used for position detection. The resulting soft sensor-actuator system has good response characteristics, high linearity, and robustness, without reducing flexibility and controllability. We evaluate these advantages experimentally, build a twin coil spring-based flexible ultrasonic motor prototype, and demonstrate feedback control of planar motion based on the constant curvature model.

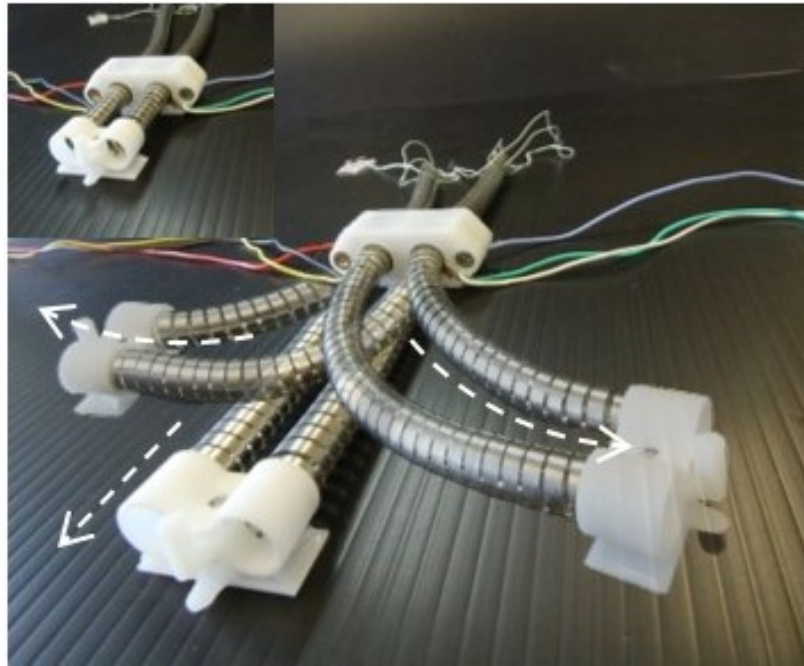


Fig. 2.28 Twin coil spring-based flexible ultrasonic motor (Twin-coil USM).

2.5.1 Design and Fabrication

Self-Sensing Using the Coil Spring

We present a new sensing methodology to detect the displacement of the coil spring slider. As mentioned above, the coil spring inserted into the stator hole has two essential roles: flexibility and pre-pressure. In this study, we also use the coil as a linear resistive sensor. In other words, this single flexible ultrasonic motor behaves like a linear resistive potentiometer, which is a kind of three-terminal resistor consisting of an electrical resistance and a sliding contact. Fig. 2.29(a) shows the self-sensing design concept for the coil. The coil and the stator are treated as the resistance element and the sliding contact of a linear potentiometer, respectively. When a voltage is applied to the ends of the coil, a voltage drop occurs between each end and the stator, which is at ground potential. When the coil moves, the voltage drop changes continuously in proportion to the displacement of the coil, and its position can be measured. One advantage of using such a potentiometer is the stability inherent in the electrical connection between the resistance element and the stator. In the design of the coil, the coil expands in the radial direction and makes firm contact with the inner surface of the stator hole. Wherever the stator is located along the resistance element, the electrical connection remains stable.

Fig. 2.29(b) shows an electrical model of the potentiometer. We define the resistance of the whole coil as R_0 , and the stator divides it into R_1 and R_2 . The resistances of the wires are denoted as R_3 and R_4 . When a voltage E_{in} is applied to both ends of the coil, the output voltage E_{out} is obtained as

$$E_{out} = \frac{R_3 + R_1}{R_1 + R_2 + R_3 + R_4} E_{in} \quad (2.17)$$

This is the output voltage from the potentiometer. With the cross-sectional area S and electrical resistivity ρ of the coil spring, the relative position of the coil spring to the stator is expressed as

$$p = \frac{S}{\rho} R_1 E_{in} \quad (2.18)$$

When (4) is substituted into (3), the position p is obtained from the measured voltage E_{out} .

$$p = \frac{S}{\rho} \left(\frac{R_0 + R_3 + R_4}{E_{in}} E_{out} - R_3 \right) \quad (2.19)$$

Since all variables in (5) are constant, it can be rewritten using the arbitrary constants C and D , as follows:

$$p = CE_{out} + D \quad (2.20)$$

This equation shows that the relationship between the measured voltage E_{out} and the position p is linear.

Constant Curvature Model

We model the motion of the Twin-coil USM to estimate the position of the end effector. The constant curvature model is a well-known forward kinematics formula for continuum robots [90]. A Twin-coil USM with two flexible ultrasonic motors can move and bend the end effector by the relationship between the two coils. Considering that the coils will move on a plane in the experiments, as described in a later section, we use a planar constant curvature model to express the motion.

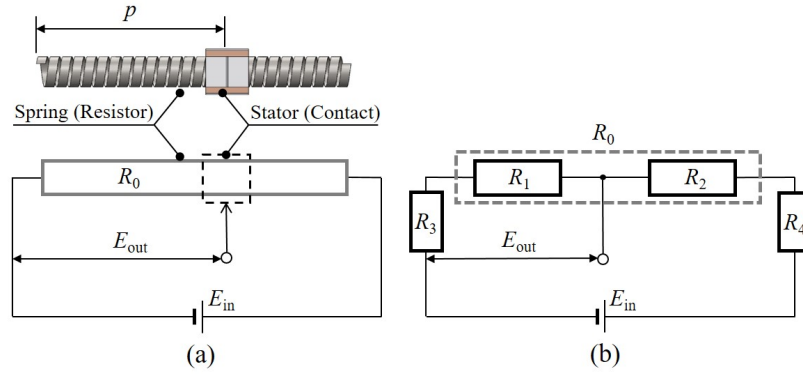


Fig. 2.29 Principle of self-sensing using the coil. (a) Mechanical components and the simplified electrical model. (b) Detailed electrical model.

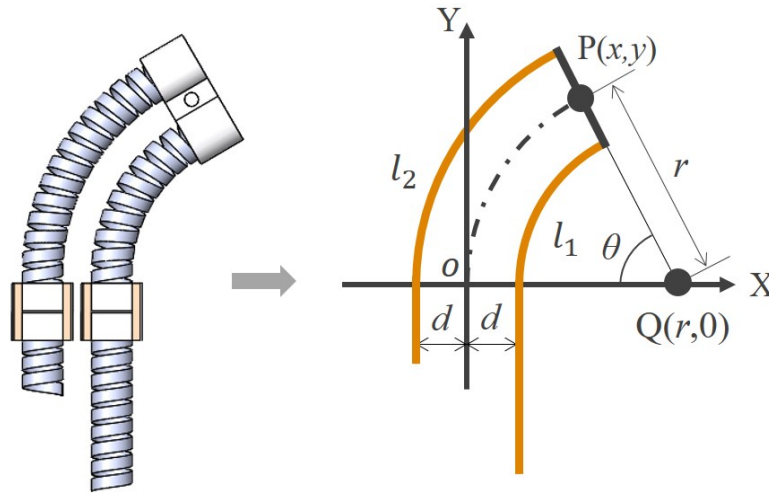


Fig. 2.30 Constant curvature model for the twin coil spring-based flexible ultrasonic motor.

Fig. 2.30 shows a schematic of the constant curvature model. The position of the end effector is expressed as $P_x = r(1 - \cos \theta)$ and $P_y = r \sin \theta$. Here, r is the bend radius and θ is the angle between the x -axis and the line PQ . The solid lines represent the coil springs of the Twin-coil USM. The springs are held at a distance of $2d$ from each other. The arc lengths of the coil springs (i.e., the dashed lines in the range $y > 0$) are set to l_1 and l_2 . Using the arc lengths l_1 and l_2 and the distance d , the end effector's position $P_x = r(1 - \cos \theta)$ and $P_y = r \sin \theta$ can be expressed as follows:

$$P_x = \frac{(l_1 + l_2)d}{l_2 - l_1} \left(1 - \cos \frac{l_2 - l_1}{2d} \right) \quad (2.21)$$

$$P_y = \frac{(l_1 + l_2)d}{l_2 - l_1} \sin \frac{l_2 - l_1}{2d} \quad (2.22)$$

These equations are the forward kinematics equation $f(l_1, l_2) = (P_x, P_y)$. The solution of the inverse kinematics equation $f^{-1}(P_x, P_y) = (l_1, l_2)$ can be solved numerically. Note that this constant curvature model ignores the influence of disturbances, such as external forces.

2.5.2 Experiments

Evaluation of Self-Sensing

The self-sensing apparatus is built and experimentally evaluated. During the experiments, a constant voltage E_{in} of 140 mV is applied to the coil spring. The output voltage E_{out} is amplified to 55 times by an amplifier circuit because the original signal is very low. This value is converted by a 10-bit analog-to-digital (AD) converter with a reference voltage of 5 V. The voltages obtained are averaged over 10 measurements to reduce noise. Fig. 2.31(a) shows the behavior of the sensor output when the coil moves. In the abscissa axis, the displacement between one end of the coil spring and the front surface of the stator is taken from 0 mm to 100 mm in 10 mm steps. In this experiment, the coil spring is manually moved using a scale. The error bars indicate the standard deviation from five tests at each position. The results show that the relationship between the displacement and the output voltage is linear, and the maximum standard deviation is 28.1 mV. The constants in (6) are obtained by approximating this result by a least-squares method ($C = 26.6$ and $D = 34.5$).

We examine how the sensor output changes when applying external forces such as those experienced when bending, extending, or contracting the coil spring. In the experiments, the output voltages in each condition are measured five times. The coil spring is set to a displacement of 50 mm and is fixed by insulating tape. The coil springs are set in constraint components with a radius of 5, 10, 15, or 20 mm. Fig. 2.31(b) shows the voltage change for each bending radius. The voltage change is slight at all bending radii, and the maximum is less than 4.0 mV even at a bending radius of 5 mm. This value is as small as the resolution of the AD converter.

The sensor output with the expansion and contraction of the coil is evaluated. One end of the coil spring is fixed to a force gauge to measure the restoring force. The voltage is measured while the restoring force changes from -0.5 N to $+0.5$ N in 0.1 N steps (negative values indicate compression). Fig. 2.31(c) shows the variation in voltage with changing force. When the restoring force is 0 N in the coil, the output voltage is defined as 0V. When

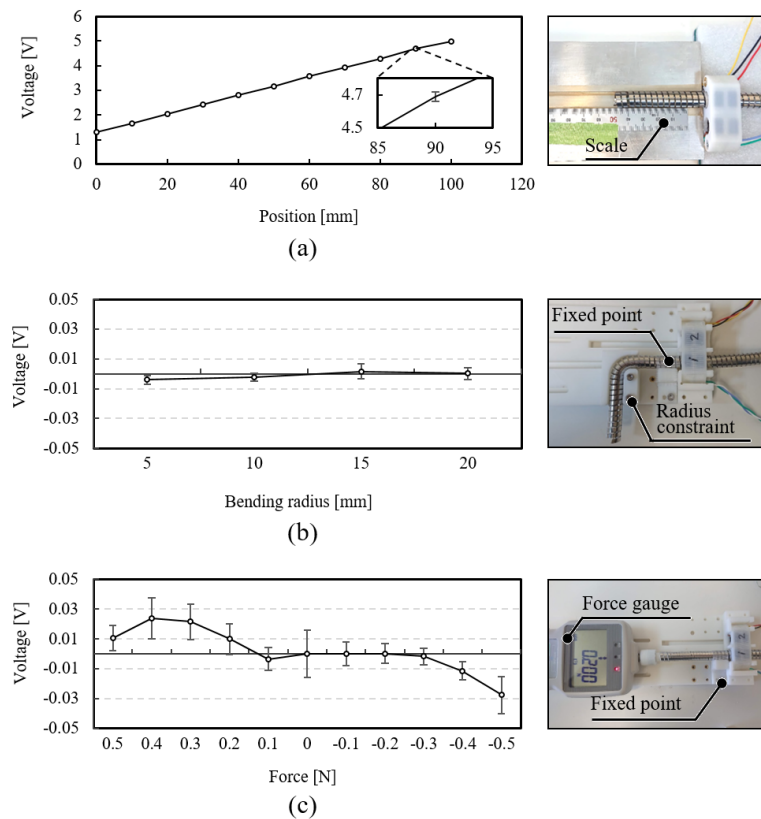


Fig. 2.31 Change in the sensor output when (a) the coil moves linearly, (b) the coil bends, and (c) the coil extends and contracts. (Error bars indicate SD from five tests of one condition).

the force of -0.5 N is applied, the voltage change is about 27.5 mV at maximum, which is equivalent to a displacement of 0.73 mm in this displacement sensor. This result indicates that the proposed sensor has high robustness against disturbances.

Feedback Control Experiment

We build a feedback control system consisting of a single flexible ultrasonic motor and the self-sensing. Fig. 2.32 shows the self-sensing feedback control loop. This circuit includes a central processing unit (an Arduino Uno), a two-phase inverter, a direct digital synthesizer (DDS), an amplifier, and a PC. To drive the flexible ultrasonic motor, the two-phase inverter converts a rectangular wave of 5 V_{p-p} from the DDS into a sine wave of 120 V_{p-p} by a bridge circuit and an LC filter circuit. To control the position and speed of the flexible ultrasonic motor, the Arduino changes the frequency and phase of the rectangular wave by

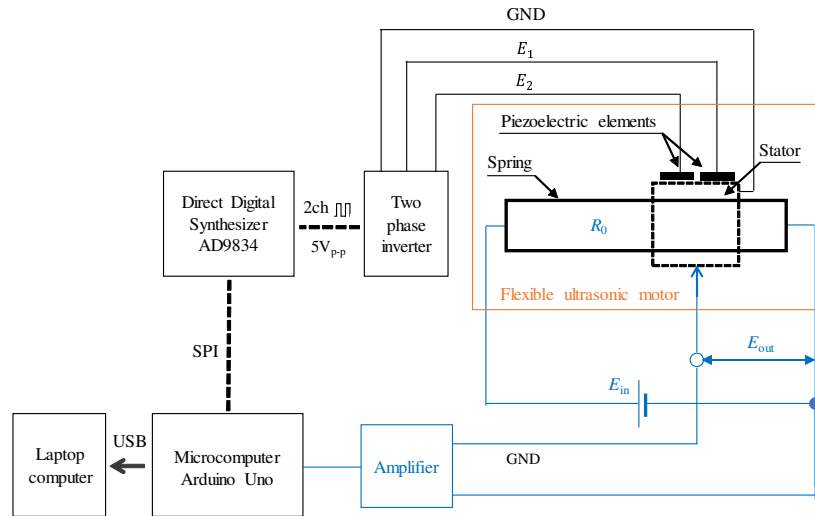


Fig. 2.32 Feedback control circuit for the flexible ultrasonic motor with self-sensing.

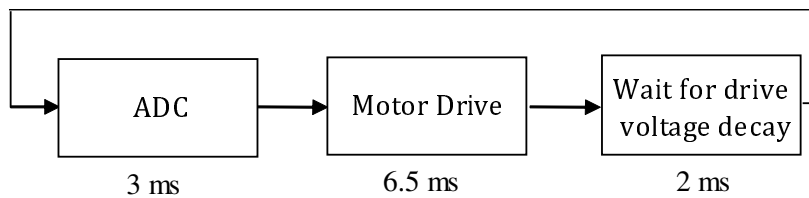


Fig. 2.33 Time table of the control cycle.

communication through the Serial Peripheral Interface (SPI). A USB cable connects the PC and Arduino.

One of the technical problems in the control system is that the actuation voltage and the sensing signal use the same terminal of the stator, as shown in Fig. 2.29. The sensor, therefore, suffers from noise due to the high driving voltage applied while the motor is moving. To overcome this problem, we implemented a program to divide the operating time into two separate sensing and actuation periods in one control cycle of 11.5 ms, as shown in Fig. 2.33. In the initial period of 3 ms, the AD converter reads the output voltage from the sensor. For the next period of 6.5 ms, the driving voltage is applied to the flexible ultrasonic motor. The remaining 2 ms is a waiting time for the safety of the system. The proportion of actuation time in one cycle is about 60%, and this reduces the speed of the motor. These times were determined experimentally to obtain stable movement.

Next, we consider how to control the motion of the flexible ultrasonic motor. The flexible ultrasonic motor changes its velocity and traveling direction by modulating the frequency f_E and the phase ϕ of the applied voltages, respectively, as described by (1) and (2). Fig. 2.34 shows the forward velocity ($\phi = \pi/2$) and the backward velocity ($\phi = -\pi/2$) of the

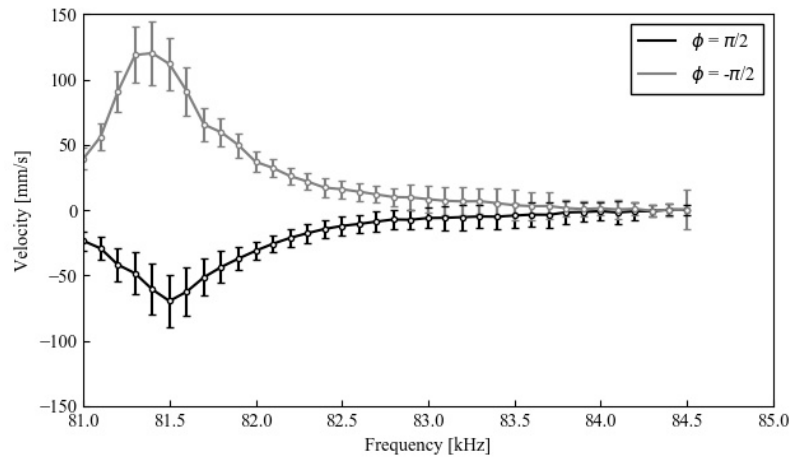


Fig. 2.34 Relationship between the velocity and the driving frequency. (Error bars indicate SD from five tests of one frequency).

motor when the frequency of the applied voltages is changed from 81.0 kHz to 84.5 kHz. The error bars show the standard deviations of five experiments because the coil vibrates in the traveling direction during the motion. Although there is a difference between the forward and backward velocities, both velocities peak at the resonance frequency (81.5 kHz) and gradually decrease at higher frequencies. Using these characteristics, it is possible to control the motion of the flexible ultrasonic motor by adjusting the driving frequency f_E between 81.5 kHz and 84.5 kHz.

Fig. 2.35 shows the closed-loop position control scheme. The proportional (P) controller determines the frequency f_E and the phase difference ϕ based on the displacement error e . Since the motor velocity depends on the traveling direction, the constant of P controller has different values in the forward and backward directions. Although the relationship between the voltage frequency and the velocity is non-linear, we assume it as linear for simplicity. The displacement of the coil is estimated by measuring the amplified voltage E_{out} . To reduce noise, the output signal passes through a 10-sample moving-average filter and a low pass filter with a cutoff frequency of 100 Hz.

We investigate the frequency response of the feedback control system. Fig. 2.36 shows the bode plot when reference sine waves of between 0.1 and 5 Hz and a constant amplitude of 60 mm are given as an input. The controller is able to follow the inputs up to about 0.5 Hz without any delay. Although the response depends on the reference displacement, the results show a good response characteristic in comparison with other linear motors because the inertia of the coil spring is very low for a generated torque.

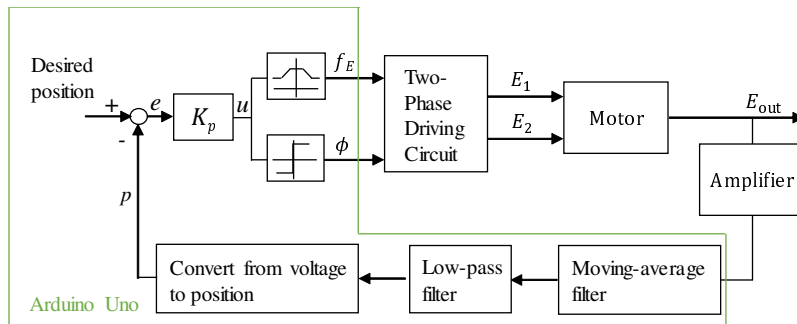


Fig. 2.35 Feedback control scheme.

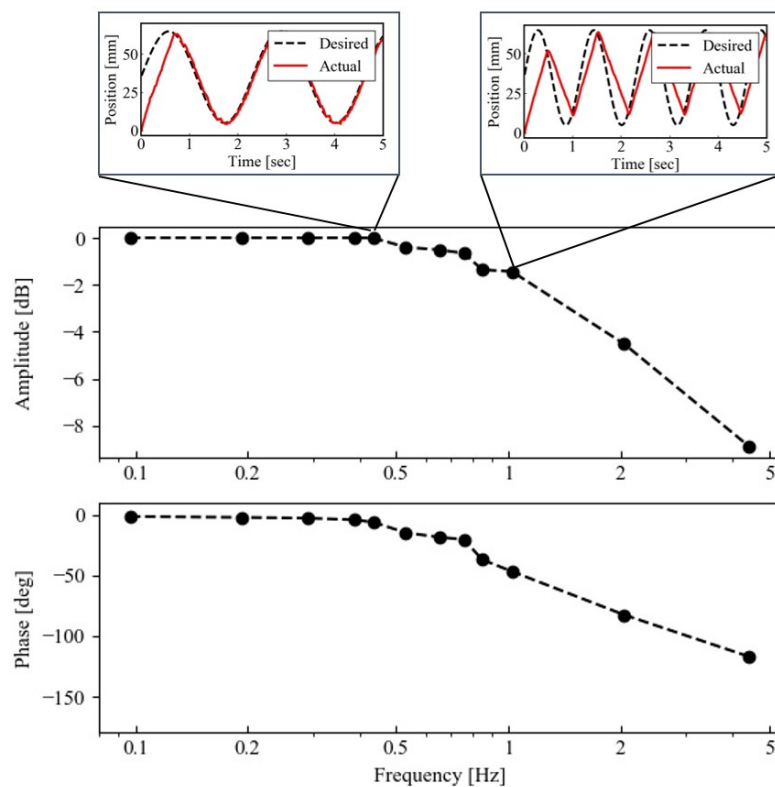


Fig. 2.36 Bode plot for the flexible ultrasonic motor.

2.5.3 Demonstration of a Twin-coil USM

We build a Twin-coil USM using two flexible ultrasonic motors and demonstrate its feedback control. Fig. 2.37(a) shows a schematic diagram of the Twin-coil USM, in which the two coils are aligned in parallel, and the ends of the coils are connected to form an end effector. The two stators are fixed to a housing part, and the distance between their centers is approximately 17 mm. As shown in Fig. 2.37(b), flexible bronze electrodes are attached to the housing to stabilize the electrical contact with the piezoelectric elements on the stator. Although the

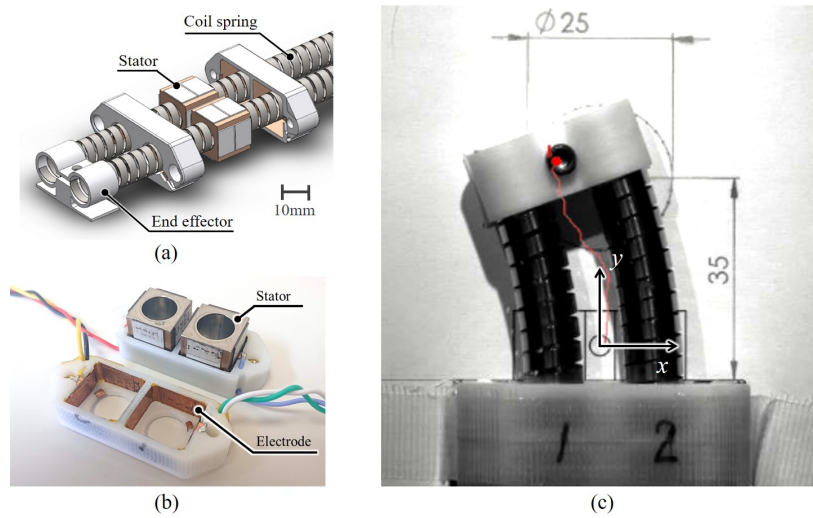


Fig. 2.37 Structure of Twin-coil USM. (a) Schematic diagram of Twin-coil USM. (b) Housing and electrodes for the stator. (c) Image taken by 2D tracking camera for tracking end effector.

end effector fixes one end of each coil, the other end remains free. The end effector of the Twin-coil USM can move and bend by controlling the displacement of the two coils. To control the two coils, we added a two-phase inverter and a DDS to the control circuit shown in Fig. 2.32.

For the demonstration of feedback control, a circle with a diameter of 25 mm at a position 35 mm away from the edge of the stator's housing is set as the desired trajectory. This circle is approximated by a 36-sided polygon prepared from an inverse kinematics correspondence table. The end effector is made to draw the same circle four times at a constant speed (11.5 s per lap) to evaluate repeatability. The motion of a marker on the end effector is tracked by a camera with a frame rate of 30 Hz (Fig. 2.37(c)). The sensor outputs from the two coils are also recorded at the same time.

Fig. 2.38 shows the response of each coil spring as measured by the self-sensing. The position of each coil spring shows a good agreement with the desired trajectory from the constant curvature model, without overshoot or delay. This result means that the end effector should have drawn the desired circle, but the actual motion showed an unexpected trajectory. Fig. 2.39 shows the motion of the end effector obtained by the camera. The recorded trajectory appears as a distorted ellipse, and it repeats the almost same trajectory four times. The difference between the sensor and the camera is caused by external forces and friction. It can be clearly seen in the x -direction, even though the stators move the coil based on the constant curvature model. There are two probable reasons for this: (1) friction between the end effector, and the ground restricts the motion, and (2) the stiffness of the proposed

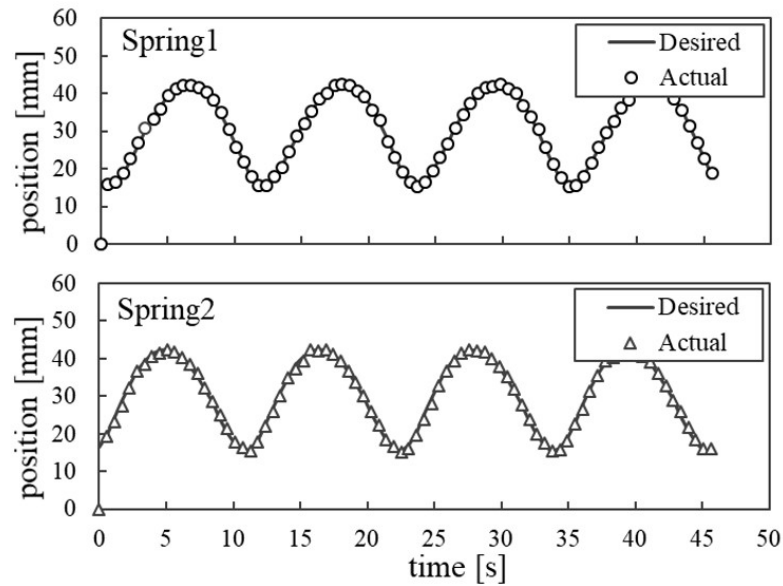


Fig. 2.38 The signals from the two coil spring-based resistive sensors. They are in good agreement with the curve from the constant curvature model.

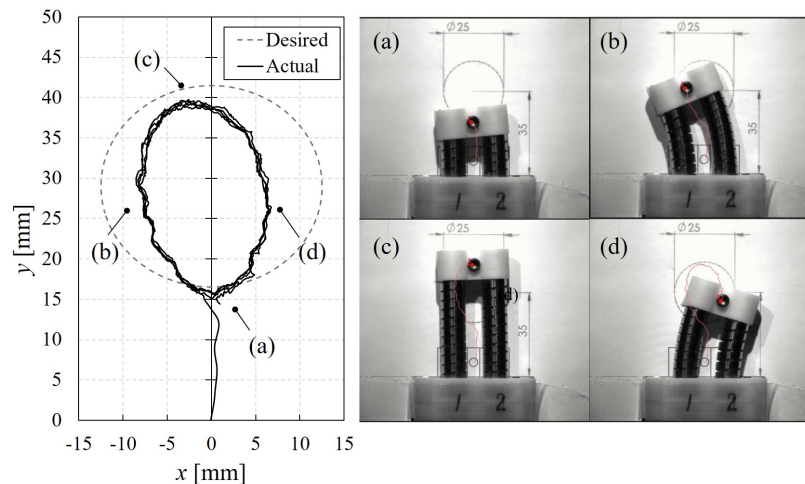


Fig. 2.39 Experimental circular motion obtained by the camera. Four snapshots from (a) to (d) are accorded to the points in the ellipse trajectory during the motion.

actuator in the x -direction is lower than that in the y -direction due to the inherently elongated structure of the spring.

2.5.4 Conclusion

We proposed a self-sensing-based soft sensor for a flexible ultrasonic motor and demonstrated the feedback control of a Twin-coil flexible ultrasonic motor. Hence, the elastic elongated

coil had three important functions: the flexibility (compliance), pre-pressure, and resistance sensor. This sensor was able to obtain a good positioning accuracy less than an error of 0.75 mm and linearity over a wide range of motion from 0 mm to 100 mm. Furthermore, the system showed high electrical stability even when the coil spring was sharply bent with a minimum radius of 5 mm or pulled/pushed with a maximum force of 0.5 N. A feedback control system was constructed and evaluated experimentally. A single flexible ultrasonic motor with a resistive sensor showed a frequency response that was able to follow an input of up to about 0.5 Hz without degradation of gain or phase delay. We built a Twin-coil USM using two flexible ultrasonic motors and implemented a feedback control of tracking a desired trajectory, but an unexpected error between the camera and the resistive sensor occurs. In future work, we will derive a correct model based on the modified constant curvature model incorporating friction and external forces.

The proposed sensor-actuator system is still under development, and there are many ways it can be improved. First, the noise resistance, which is robustness against the influence of external noise, can be enhanced. Since the coil spring is made from stainless steel and has low resistance, the sensor requires a very low voltage to minimize power consumption and heat dissipation, which results in weak noise resistance. Increasing the electrical resistance by an electrostatic coating can increase the resolution of the sensor and its susceptibility to noise. Second, the motor response can be improved. The controller restricts the motor response by alternating the operation between sensing and actuation in a control cycle. Electrically insulating a part of the stator to separate the sensing and actuation grounds would allow the controller to drive both the sensor and the actuator simultaneously, improving the motor response. Third, it would be possible for the sensor to measure more complex motion without changing its structure or adding additional components. Although the proposed sensor only measures the displacement of the coil, it is known that the strain of a coil spring can be estimated by measuring its inductance [91]. Inductance-based self-sensing could also be embedded in our proposed system without the need for extra mechanical parts.

Chapter 3

Flexible Rack Pinion Actuator

The proposal, design, modeling, and sensing of the flexible ultrasonic motor as the first flexible linear motor were studied in Chapter 2. We also built a 2 DoF continuum robot using this motor to demonstrate feedback control. This chapter introduces a flexible rack pinion actuator as the second flexible linear motor and shows robot implementation with three or more degrees of freedom using it. We investigate how the flexibility and stroke, which are excellent features of flexible linear motors, contribute to the locomotion by focusing on continuum robots which elongate their body. Section 3.2 presents the design of the flexible rack pinion actuator and how it works as continuum robots. Section 3.3 reports a mobile continuum robot with several actuated disks on its axis as a first application. We show basic modeling and elementary manipulation and locomotion test of the continuum robot. Section 3.4 build a climbing continuum robot as another application and study how the features of flexible linear motors can enhance the climbing capabilities of a robot.

3.1 Design and Mechanism

A flexible rack pinion actuator is a type of flexible linear motor that comprises a pinion gear and a flexible tube (instead of rigid rack with gears), which convert rotational motion to linear motion. The pinion gear attached to the DC motor engages with the helical groove on the surface of the flexible tube (Fig. 3.1 (a)). As with the rack and pinion mechanism, the rotational motion moves the flexible tube lineary. This enables the transmission of the motor power even when the flexible tube is bending or buckling. To improve the engagement between the gear and flexible tube, the gear was designed to be similar to an enveloping worm, whose diameter increases from its center toward the end and whose teeth twist clockwise along the axis, as shown in Fig. 2.22 (b). The flexible tube, called stripwound metal hose, has been used to protect electrical wires or liquid and gas tubes. The flexible design is formed by

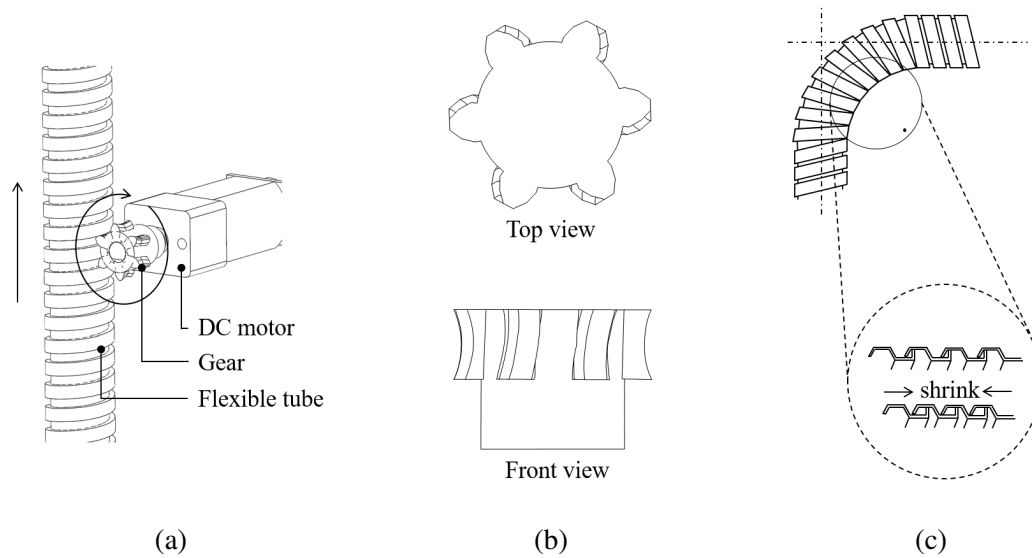


Fig. 3.1 Overview of the flexible rack pinion actuator.

spirally winding a metal plate with S-shaped profile, as shown in Fig. 2.22 (c). The bending motion is achieved because each S-shaped corrugation slides against each other and contracts. Although we can use a helical spring instead of the flexible tube [32, 92], the engagement with the gear would not be robust because of the elasticity. The flexible tube shrinks but does not elongate, potentially carrying heavy loads.

3.1.1 Robot Common Design

Fig. 3.2 shows an overview of a proposed continuum body composed of three flexible tubes that are connected in parallel. The flexible tubes, which are located at the vertices of an equilateral triangle, pass through a driving unit with three DC motors (75:1 Micro Metal Gearmotor HP 6V, Pololu Co.). One end of tube is fixed to an endpoint made of plastic, and the other end is free. As with the rack and pinion mechanism, the rotational motion moves the flexible tube laterally relative to the driving unit, as shown in Figure 4b. The continuum body can bend or elongate by controlling the length of each flexible tube. We adopted a flexible tube with a diameter of 10 mm and a minimum bending radius of 25 mm.

3.2 Mobile Continuum Robot

Locomotion of a flexible and elongated continuum robot in confined spaces allow the access for hard-to-reach targets. This is useful for applications including inspection, rescue, and

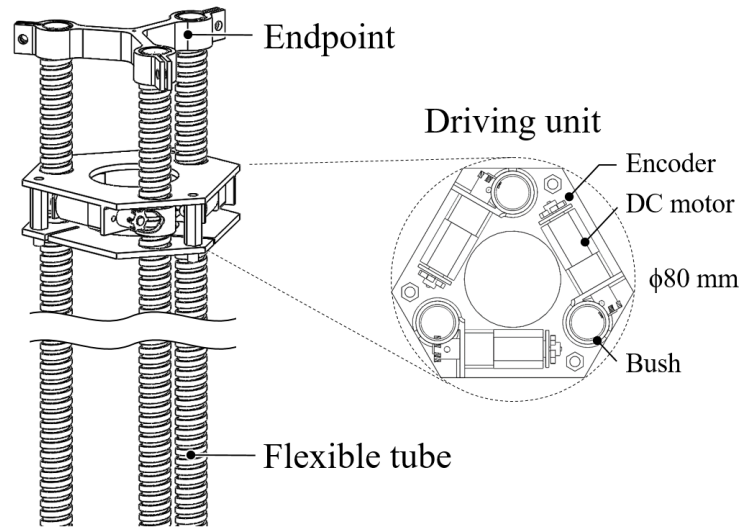


Fig. 3.2 Overview of the continuum robot using flexible rack pinion actuators

repair activity. The flexibility and stroke of the actuator will allow the continuum robot to move efficiently in such environments. We propose a mobile continuum robot as first application of the flexible rack pinion actuator that have both flexibility and stroke. Since each drive unit can be mounted on the same tube axis, by increasing the number of them, the robot can take various forms without expanding its diameter. First, we build a prototype of continuum robot with three degrees of freedom and controlled it based on the basic model. Next, the prototype with two drive units (6 DoF) is tested for the locomotion performance using two motion sequences.

3.2.1 Kinematics

To determine the position of the robot end effector, the kinematics of the robot were analyzed. The constant curvature model is a well-known forward kinematic formula for continuum robots [90]. Extrinsic actuated continuum robots driven by wire mechanism often require a model that takes into account the friction between the wire and the internal structure [93, 94], but our intrinsic actuated continuum robot driven by flexible tubes does not require it. In the constant curvature model model, the continuum sections are approximated using the shape parameters L , λ , ϕ , and θ . As shown in Fig. 3.3, L and λ are the length and radius, respectively, of the arc formed by the bending of the robot; ϕ determines the elevation; and θ is the angle of the plane containing the arc. Assuming that neither buckling nor compression occurs in each flexible tube, the kinematics of the proposed robot are given by the following

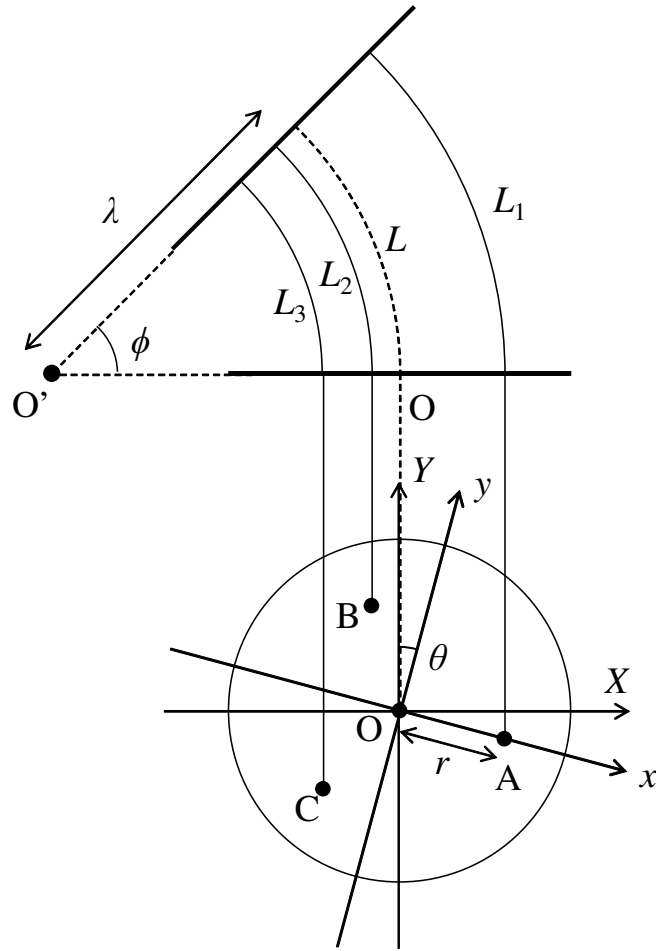


Fig. 3.3 Kinematics of a continuum section

five equations:

$$L = \frac{L_1 + L_2 + L_3}{3} \quad (3.1)$$

$$\lambda = \frac{r(L_1 + L_2 + L_3)}{2\sqrt{L_1^2 + L_2^2 + L_3^2 - L_1L_2 - L_2L_3 - L_3L_1}} \quad (3.2)$$

$$\phi = \frac{2\sqrt{L_1^2 + L_2^2 + L_3^2 - L_1L_2 - L_2L_3 - L_3L_1}}{3r} \quad (3.3)$$

$$\theta = \tan^{-1} \frac{\sqrt{3}(L_3 - L_2)}{L_2 + L_3 - 2L_1} \quad (3.4)$$

$$L = \lambda \phi \quad (3.5)$$

where L_1 , L_2 , and L_3 are the lengths of the three flexible tubes and r is the radial distance from the central axis to the tubes. Notice that the constant curvature model does not hold under heavy load conditions, because the flexible tubes contract and buckle.

3.2.2 Experiments

Circular Trajectory Tracking

To evaluate the dynamic response of the proposed robot, a circular trajectory tracking experiment under closed-loop control was conducted. A circular trajectory was generated by changing the θ while keeping the arc length L and elevation ϕ constant. Specifically, each flexible tube was instructed to follow the corresponding target trajectory D_n ($n = 1, 2, 3$) by applying proportional-derivative (PD) control to the motor encoder position. The target trajectories for the three tubes were defined as

$$D_1 = L_{\text{initial}} + A \sin(2\pi ft) \quad (3.6)$$

$$D_2 = L_{\text{initial}} + A \sin\left(2\pi ft - \frac{2}{3}\pi\right) \quad (3.7)$$

$$D_3 = L_{\text{initial}} + A \sin\left(2\pi ft - \frac{4}{3}\pi\right) \quad (3.8)$$

where L_{initial} is the initial length of each flexible tube and A and f are the amplitude and frequency of the circular target trajectory, respectively. During the experiments, the initial length L_{initial} and the amplitude A were set to constant values of 80 and 15 mm, respectively. The end position of the robot was measured using a high-speed camera (VW-9000, Keyence Co., Japan) at a frame rate of 250 Hz, as shown in Fig. 2.22. The camera system tracked a marker attached to the robot end effector, and the measurements were transferred to a computer for image processing.

The images on the right and left hand sides of Fig. 3.5 respectively show the circular trajectories traced by the robot end effector and the motor response measured by the encoders

over the course of the trajectories. The cases shown in Fig. 2.22 (a)-(c) correspond to trajectory frequencies of 0.5, 1, and 2 Hz, respectively. A nearly perfect circle with a large vibration was achieved at 0.5 Hz (Fig. 2.22 (a)). This is because an acceleration generated by the discontinuous engagement between the gear and the flexible tube caused the robot end effector to sway; even if the gear rotation is constant, variations in the flexible tube velocity are produced in this case. Elliptical trajectories were observed when the trajectory frequency exceeded 0.5 Hz because the inertial effect increases as the velocity of the robot end effector increases (Fig. 2.22 (b) and (c)). The asymmetry of the starting position when describing the trajectories generates the elliptical trajectory. In comparison with the error of the circle tracking measured by the high-speed camera, that of the motor response measured by the encoders is small (Fig. 2.22 (a) and (b)). However, a delay between the target positions of the tubes and those measured by the encoder was observed at 2 Hz (Fig. 2.22 (c)).

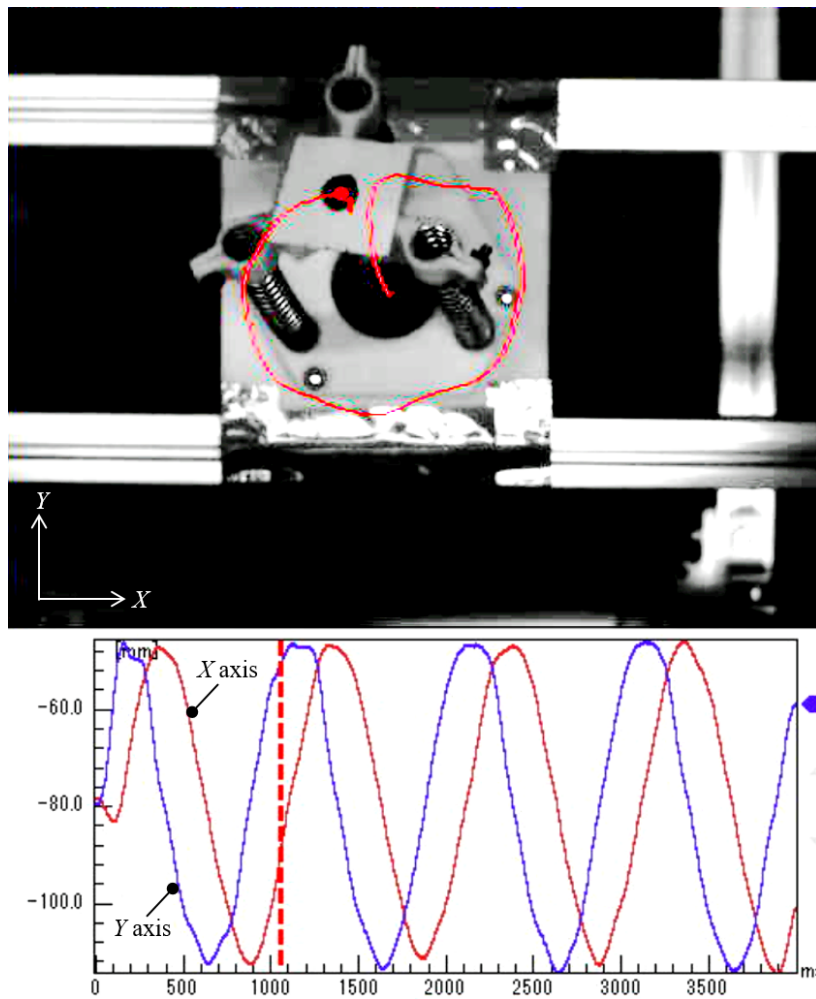


Fig. 3.4 Experimental setup for measuring the robot end effector position. A high-speed camera was used to track a marker attached to the robot end effector. In the lower image, the high speed camera software shows the coordinates of the robot end effector.

Locomotion

The above prototype continuum robot uses only one driving unit; however, the proposed design can take on various forms with higher numbers of driving units. Experiments using two driving units were conducted to investigate the locomotion performance of the robot. In nature, slender limbless organisms such as snakes and earthworms efficiently move and explore the surrounding space by using several different gaits. The robot was tested with two operating sequences inspired by these locomotion.

1) *Snake – like locomotion* : Real snakes exhibit many forms of locomotion, including linear progression, sidewinding, concertina movement, and lateral undulation [95]. In the present experiment, the locomotion of the robot was defined based on linear progression, which is motion that propels the moving body by generating sine waves that propagate along its length. The amplitude of the lateral wave was set to zero so that the robot only generates a vertical sine wave. The robot length was set to 200 mm, and a rubber mesh sheet with a large frictional force was laid on the ground. Fig. 3.6 (a) shows a snapshot of the locomotion experiment of the robot. Although the sine wave did not span the entirety of the robot's length because of the ease with which the flexible tube buckled, locomotion was successfully realized. An average locomotion speed of 16 mm/s was achieved using this type of locomotion.

2) *Earthworm – like locomotion* : An earthworm is composed of several segments, each of which has two types of muscles: longitudinal and circumferential muscles [96]. The contraction of the longitudinal muscles shortens the body and increases its diameter, whereas that of the circumferential muscles reduces the diameter and elongates the body. Locomotion is achieved by contracting both of these types of muscles, which results in the propagation of a longitudinal wave in the anteroposterior direction. Although the robot diameter is constant, similar behavior can be achieved by lifting the driving unit slightly above the ground. In this experiment, the locomotion velocity was measured on a slippery plastic sheet. A snapshot of the earthworm-like locomotion experiment is shown in Fig. 3.6 (b). The maximum length of the robot during locomotion was 370 mm, and the initial length was 220 mm. The robot moved forward with some slippage, and the average velocity was 10-20 mm.

Robustness

A key characteristic of the robot is its flexibility, which provides the structure with a high robustness. The robustness of the robot was tested by applying an impact to it using a hammer during operation. Fig. 3.7 shows a series of snapshots depicting when the robot was hit with a rubber hammer while it followed a circular trajectory. This experiment demonstrates the

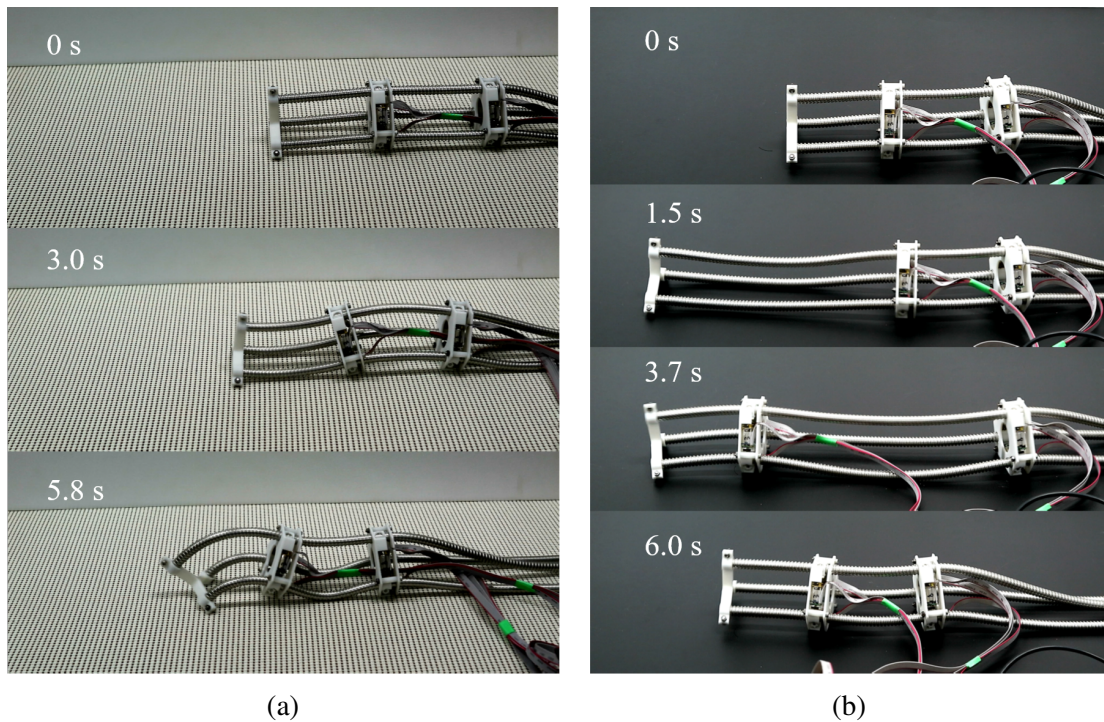


Fig. 3.6 Photo sequence of (a) snake-like and (b) earthworm-like locomotion. The proposed robot moves by generating sine waves that propagate along its length. In snake-like locomotion, the robot moves by generating sine waves that propagate along its length. In earthworm-like locomotion, it moves by alternately elongating and contracting the body.

high robustness of the robot in terms of its ability to maintain the target motion even under extreme conditions.

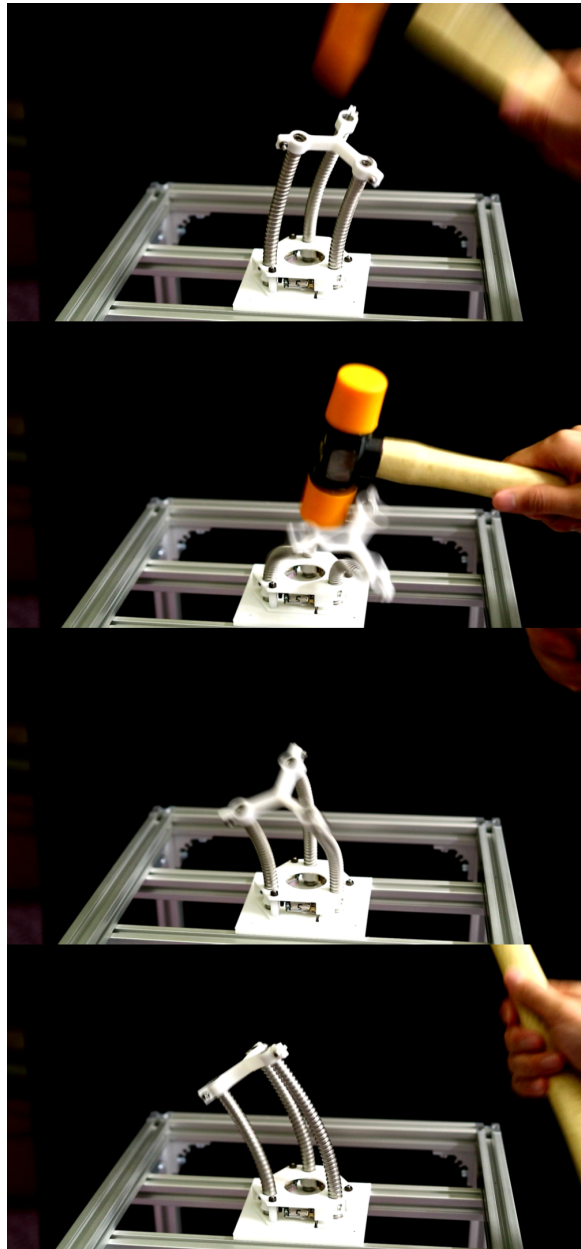


Fig. 3.7 Experiment to verify the robustness of the proposed robot. The robot maintains a motion following a circular trajectory even when it is hit with a hammer.

3.2.3 Conclusion

The proposed mobile continuum robot design is the design that provides unlimited extensible sections for locomotion. In the developed design, motor rotation is converted into the linear motion of a flexible tube, as with the rack-and-pinion mechanism. The long flexible tube length provides a large traveling distance unless it buckles.

The continuum robot enables the control of the section length and bending radius. In comparison with traditional continuum robots mostly used as manipulators, the proposed robot is better suited for locomotion because it performs intrinsic actuation using DC motors. This gives the robot a high locomotion efficiency by achieving low mechanical loss, high response frequency, simple modeling, and high control performance. Although the prototype drags the extra cables for the control, it could be on-board by installing a microcomputer and battery in the driving unit in the near future. The robot locomotion was experimentally tested using two operating sequences. The robot showed especially good earthworm-like locomotion performance on a slippery surface.

There is still plenty of room for improving the locomotion velocity of the proposed robot. Increasing the diameter of the flexible tube would make it more difficult for the tube to buckle, thus allowing the traveling distance to be increased. The efficiency of the robot can be improved by optimizing the motor gear ratio or the locomotion frequency depending on the required torque or the ground friction, respectively.

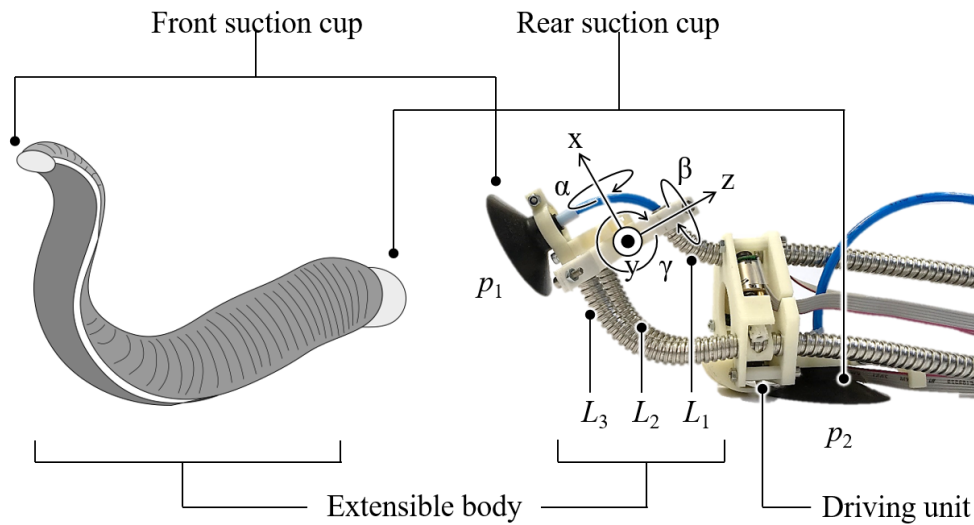


Fig. 3.8 The left figure shows real leech and the right figure shows LEECH. LEECH is a five DoF system, including two suction cups (p_1 and p_2), driven by pumps and three flexible tubes (L_1 , L_2 , and L_3) controlled by DC motors. DoF, degree of freedom; LEECH, Longitudinally Extensible Continuum-robot inspired by Hirudinea.

3.3 Climbing Continuum Robot

Locomotion of soft-bodied organisms, such as amoeba, worms, and octopuses, is safe, robust, and adaptable and has great promise for applications in complex environments. While such organisms fully exploit the potential provided by their soft structures, engineering solutions commonly constrain soft deformation in favor of controllability. In this subchapter, we study how soft deformations can enhance the climbing capabilities of a robot. We introduce a robot called Longitudinally Extensible Continuum-robot inspired by Hirudinea (LEECH), which has few shape constraints (Fig. 3.8). Inspired by real leeches, LEECH has a flexible extensible body and two suction cups at the ends. It is capable of performing 3D climbing locomotion using two vacuum suction cups and flexible rack pinion actuators. The large deformations occurring in LEECH extend its workspace compared to robots based on constant curvature models, and we show successful locomotion transition from one surface to another at angles between 0° and 180° in experiment. We develop a model based on multibody dynamics to predict the nonlinear deformations of the robot, which we verify in the experiment. The model reveals a nondimensional morphological parameter, which relates the robot's shape to its mass, stiffness, and size. The workspace of LEECH as a function of this parameter is studied in simulation and is shown to move beyond that of robots based on constant curvature models.

3.3.1 Modeling

The first step in exploiting the power of nonlinear deformations is to understand the physics behind deformation. In this work we present a model for large deformations to predict LEECH's body shape. The constant curvature model is the most widely used kinematic framework [90], and a variety of ways for deriving the homogeneous transformation have been studied such as D–H parameters [97, 98], Frenet–Serret formulas [97], and integral representation [99]. However, it restricts the achievable workspace of the end effector. In addition, Bernoulli–Euler beam theory [100] and Cosserat rod theory [101] have been used to describe continuum robots whose shapes are controlled primarily by elasticity. We describe a model based on multibody mechanics,³¹ which involves masses, springs, and dampers in discrete links.

The bending motions investigated in LEECH are flat-wall climbing and wall-to-wall transitions. These motions occur only in one plane at a time, which allows for an accurate description of the system with a planar model. To approximate the soft body, we use a chain of rigid bodies under the influence of gravity with acceleration g . We assign a linear torsional stiffness k and linear damping d at every joint. The first element is attached with a joint to an inertial reference system I . Each rigid body is associated with a mass m located at its tip and a length l . Fig. 3.9 (a) illustrates such a chain of n elements. The equations of motion are derived using the projected Newton-Euler equations with the generalised coordinates $q = [\theta_1, \theta_2, \dots, \theta_n]^T$, that is, the sum of all n bodies' generalised momenta render the inertial terms of the equations of motion

$$\sum_{k=1}^n \mathbf{J}_k^T \dot{p}_k = \mathbf{M}\ddot{q} + h \quad (3.9)$$

where \mathbf{J}_k is the Jacobian of the point mass in body k , \dot{p}_k is the time derivative of the momentum of the point mass in body k , \mathbf{M} is the mass matrix, \ddot{q} is the second derivative of the generalised coordinates, and h is the vector of gyroscopic accelerations.

Equations of motion

The equations of motion take the form

$$\mathbf{M}\ddot{q} + h = E + G + \mathbf{J}_c^T \lambda \quad (3.10)$$

where E is the vector of external forces acting on the system, G is the vector of the generalised gravitational force, and \mathbf{J}_c^T are the constraint forces. External forces can be applied at any

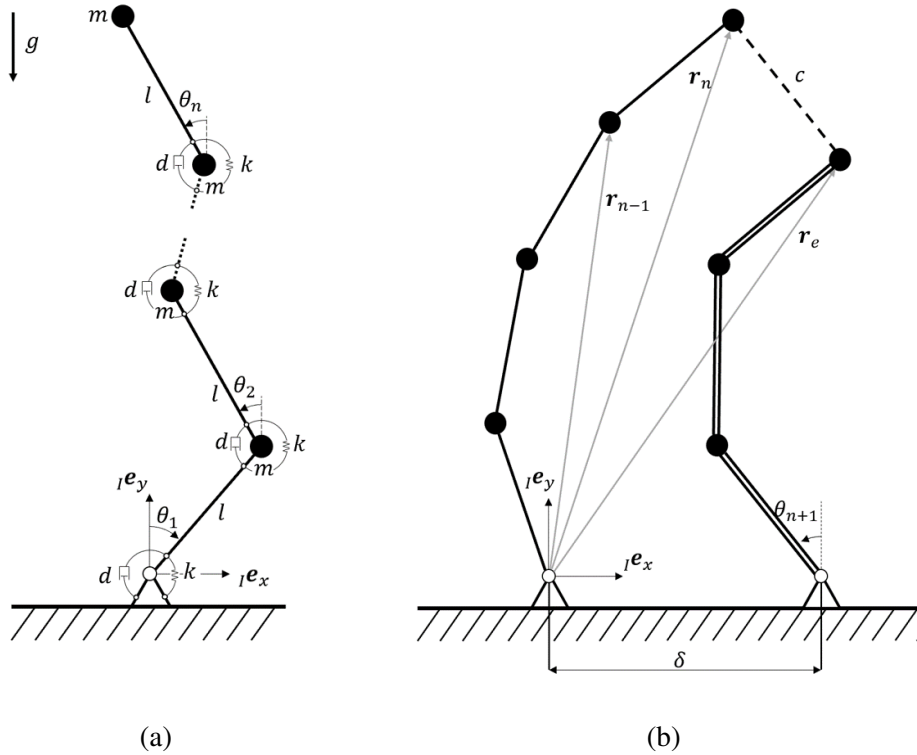


Fig. 3.9 Sketches of the proposed model. (a) One chain of rigid bodies with generalized coordinates $q = [\theta_1, \theta_2, \dots, \theta_n]^T$ and mass m , length l , stiffness k , and damping d per body. (b) Two chains located a distance δ apart and connected at their tips with geometric constraints.

point i on the model and are computed by

$$F_i = \mathbf{J}_i f_i \quad (3.11)$$

with \mathbf{J}_i the Jacobian of the system at point i and f_i the planar force applied at point i . Furthermore, external forces contain the stiffness and damping terms due to the springs and dampers we apply to the chain. The i th link in the chain is subject to the forces

$$S_i = -k(\theta_i - \theta_{i-1}) - k(\theta_i - \theta_{i+1}) \quad (3.12)$$

and

$$D_i = -d(\dot{\theta}_i - \dot{\theta}_{i-1}) - d(\dot{\theta}_i - \dot{\theta}_{i+1}) \quad (3.13)$$

Note that the first and the last element in the chain are described by

$$S_1 = -k\theta_1 - k(\theta_1 - \theta_2) \quad (3.14)$$

$$S_n = -k(\theta_n - \theta_{n-1}) \quad (3.15)$$

and

$$D_1 = -d\dot{\theta}_1 - d(\dot{\theta}_1 - \dot{\theta}_2) \quad (3.16)$$

$$D_n = -d(\dot{\theta}_n - \dot{\theta}_{n-1}) \quad (3.17)$$

The spring and damper generalised force terms can therefore be written as a matrix-vector multiplication by $\mathbf{S}q + \mathbf{D}\dot{q}$ which leads to the external force vector

$$E = \mathbf{J}_i f_i + \mathbf{S}q + \mathbf{D}\dot{q} \quad (3.18)$$

For the generalised gravitational force we have

$$G = \sum_{i=1}^n \mathbf{J}_i^T \begin{pmatrix} 0 \\ -mg \end{pmatrix} \quad (3.19)$$

As we will see in the next subsection, we model the robot with parallel chains of rigid bodies that are interacting through geometric constraints which are enforced on the equations of motion by Lagrange multipliers. Assume we have defined a geometric constraint $g(q) = 0$. The second derivative of this constraint with respect to time takes the form

$$\ddot{g} = \mathbf{J}_c \ddot{q} + \xi(q, \dot{q}) = 0 \quad (3.20)$$

with $\mathbf{J}_c = \mathbf{J}_c(q)$ what we call the constraint Jacobian and ξ containing all the terms not depending on \ddot{q} . We will now make use of Gauss' principle to enforce the constraints in the equations of motion. First recall that we need to find the constraint force λ given in the equations of motion

$$\ddot{q} = \mathbf{M}^{-1} (E + G + \mathbf{J}_c^T \lambda - h) \quad (3.21)$$

With (3.20) we obtain

$$\mathbf{J}_c \mathbf{M}^{-1} (\mathbf{E} + \mathbf{G} + \mathbf{J}_c^T \boldsymbol{\lambda} - \mathbf{h}) = -\boldsymbol{\xi} \quad (3.22)$$

Solving for $\boldsymbol{\lambda}$ we get

$$\boldsymbol{\lambda} = (\mathbf{U}_c \mathbf{M}^{-1} \mathbf{J}_c^T)^{-1} (-\boldsymbol{\xi} - \mathbf{I}_c \mathbf{M}^{-1} (\mathbf{E} + \mathbf{G} - \mathbf{h})) \quad (3.23)$$

Inserting the found $\boldsymbol{\lambda}$ back to the equations of motion leads to the constrained equations of motion.

Robot model

For the chain of links to represent a model of our robot we add a second chain located a distance δ from the first one apart as shown in Fig. 3.9 (b). Note that we doubled the stiffness, damping, and mass to model two tubes instead of just one in the second chain. This way, we can model the motion of our 3-tube robot in the plane. The interaction between the two chains is implemented by geometric constraints as outlined in the last subsection. More precisely, we added three constraints to model a bridge between the last element of each link:

$$\text{-Parallel:} \quad g_1(q) = \theta_n - \theta_e \quad (3.24)$$

$$\text{-Distance:} \quad g_2(q) = r_{ne} - c \quad (3.25)$$

$$\text{-Perpendicular:} \quad g_3(q) = r_{n(n-1)}^T r_{ne} \quad (3.26)$$

The parallel constraint ensures that the last two elements of each chain, element n on the first chain and element e on the second, are parallel to each other. The distance constraint enforces the tip of each chain to be a distance c apart from each other. Finally, the perpendicular constraint makes sure that the last link of the first chain is perpendicular to the distance vector of the two chain tips. The robot's suction cup with mass m_s is affecting its behaviour and we thus model it as an external force acting on the element e on the second chain with

$$\mathbf{F}_{m_s} = \mathbf{J}_e^T \begin{pmatrix} 0 \\ -m_s g \end{pmatrix} \quad (3.27)$$

For the subsequent investigation we have used model parameters as indicated in Table 3.1. We found the stiffness by comparing the model prediction of a chain with a tube experiment, where we measured the slacking of the tube under the influence of gravity for different tube

Table 3.1 Values of Physical Parameters of LEECH Model

Symbol	Quantity	Value
k	Stiffness	0.055 Nm/rad
m	Element mass	4.4 N/m
m_s	End effector mass	0.0068 kg
δ	Chain distance bottom	0.0398 m
c	Chain distance top	0.0398 m
l	Element length	0.01 m
g	Gravitational acceleration	9.81 m/s ²

lengths, as shown in Fig. 3.10 (a). The element mass is simply found by weighing the tube and dividing it by the element length l .

The presented model is dynamic, but since we are interested in the static solution we will compute the forward dynamics in simulation until we reach the static equilibrium. Therefore, we do not need to get an accurate value for the damping terms from the real system but need to make sure that the simulation converges to the static solution. In most of our simulations we therefore chose a value of 0.1 Nms/rad which was underdamped but converged to the equilibrium in a reasonable time.

Fig. 3.10 (b) shows the simulation result of the proposed model with a constant curvature model. The chains in both models have the same length, but the proposed model is bending under the effect of gravity due to its stiffness, constraints, and inertial properties.

3.3.2 Robot Architecture and Locomotion Principle

Fig. 3.11 shows the control system of the proposed robot. A personal computer hosting the user interface is connected to an Arduino Mega by USB and sends commands for specific motions. The Arduino generates a PWM signal based on the command and supplies voltages to motors and pumps through drivers. The front and rear suction cups with a diameter of 50 mm (ZP50CN; SMC Co., Japan) are actuated using two vacuum pumps (D2028B; AIRPON, China). In this suction system, the payload capacity per one suction cup is up to ~ 1.7 kg on a vertical wall, and it is possible to lift our robot with a weight of 240 g (on-board). Each DC motor moves the flexible tube according to the applied voltage and elongates or bends the robot body. Encoders attached to the end of the motors send position information of the flexible tube to the Arduino, closing a feedback loop. Control in the present system does not need to be very precise and we therefore neglect additional effects arising in our soft-tube actuators, such as backlash, for the sake of simplicity. For tasks requiring high accuracy, however, the controller needs to consider such effects. The locomotion of the proposed robot

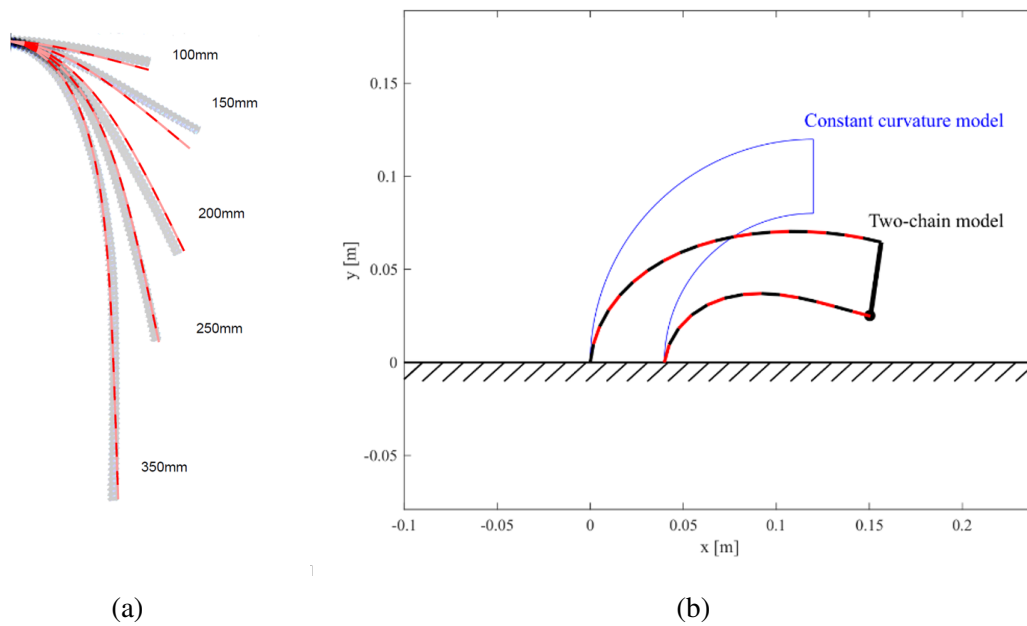


Fig. 3.10 Simulation results of the model. (a) Comparison of the static solution of the model in simulation with the real-world tube for different tube lengths. (b) Comparison of the two-chain model with the constant curvature model.

is similar to that of leeches and inchworms, which involves repeated elongation/contraction of the continuum body and releasing/grasping of the front and rear suction cups. The steps in the locomotion procedure are shown in Fig. 3.12 and can be described as follows. The circle with hatch pattern represents the suction cup that attaches to the substrate, while the other white circle represents the suction cup that detaches to the substrate. First, we choose the locomotion type such as climbing and bending and set the flexible tube length (L_1 , L_2 , and L_3). For example, when the robot moves while turning to the right, the length of the left tube L_2 is set larger compared with the right tube L_3 . After the rear suction cup adheres to the substrate, the front suction cup releases. Then, each tube is pushed until it has the set length. At this time, if the length of the center tube L_1 is short, the robot lifts its end, and if the tube on either side is short, the robot body turns to either left or right. After the front suction cup attaches to the substrate, the rear suction cup releases. The robot contracts by pulling all flexible tubes which completes one stride of the locomotion procedure.

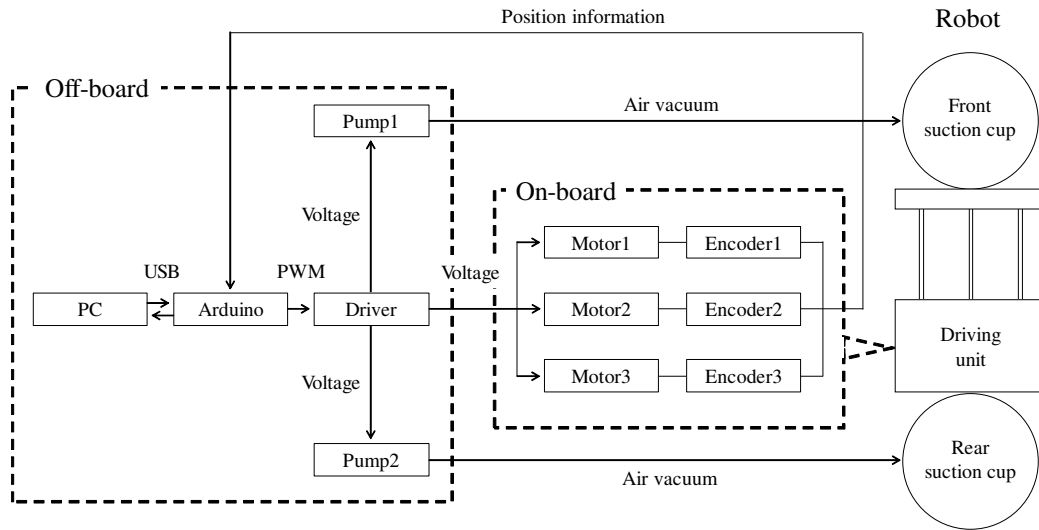


Fig. 3.11 System hierarchy.

3.3.3 Experiments

Model Comparison

To evaluate the accuracy of the proposed model, we measured the deformations of the flexible tubes in our robot. A comparison of the robot shape in simulation with the real world is shown in Fig. 3.13. In this experiment, we took several pictures while the robot was attached to a vertical wall. The tube shape was measured from the images and resized for comparison with the model. The stiffness of the model was tuned manually until the deformations of the model and the experiment were matched. Furthermore, we measured tube lengths from the picture images and substituted these values for the two models: The two-chain model and constant curvature model. When the tube lengths are short, there is almost no difference between these two models, whereas when the tube lengths are long, the tube shape and robot endpoint differ greatly due to the effect of gravity and internal elasticity. The proposed model predictions match the real robot deformations well, even when the tubes are greatly deformed. Minor errors between the real robot and the proposed model are detectable, which probably arise because of stiffness nonlinearities in the real system and neglected mass and hardness of the air supply tubes inside the central flexible tube.

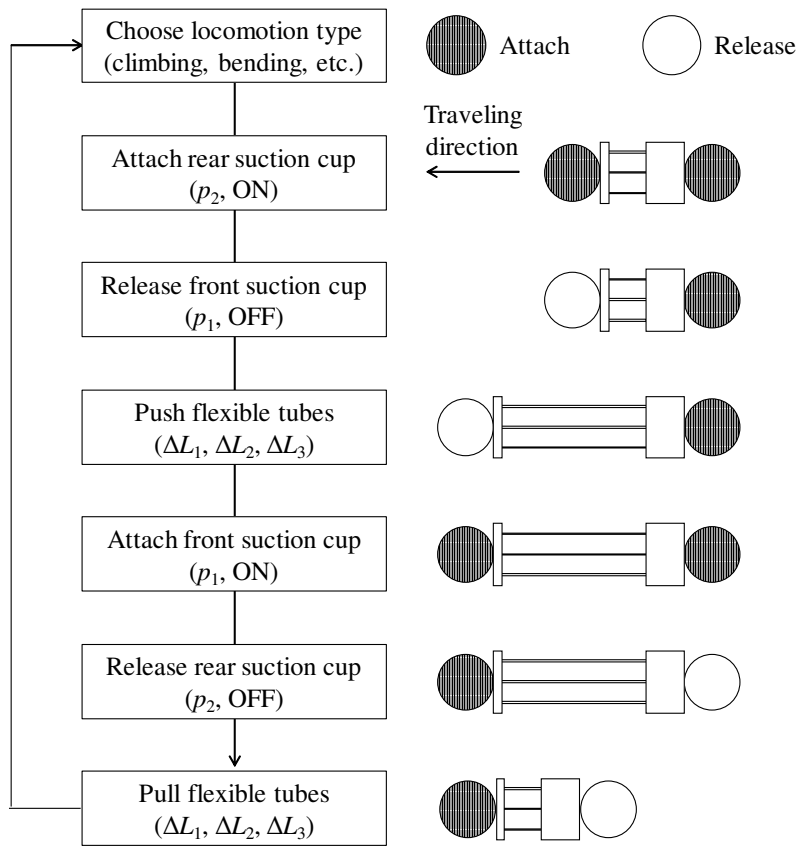


Fig. 3.12 Steps in the locomotion procedure.

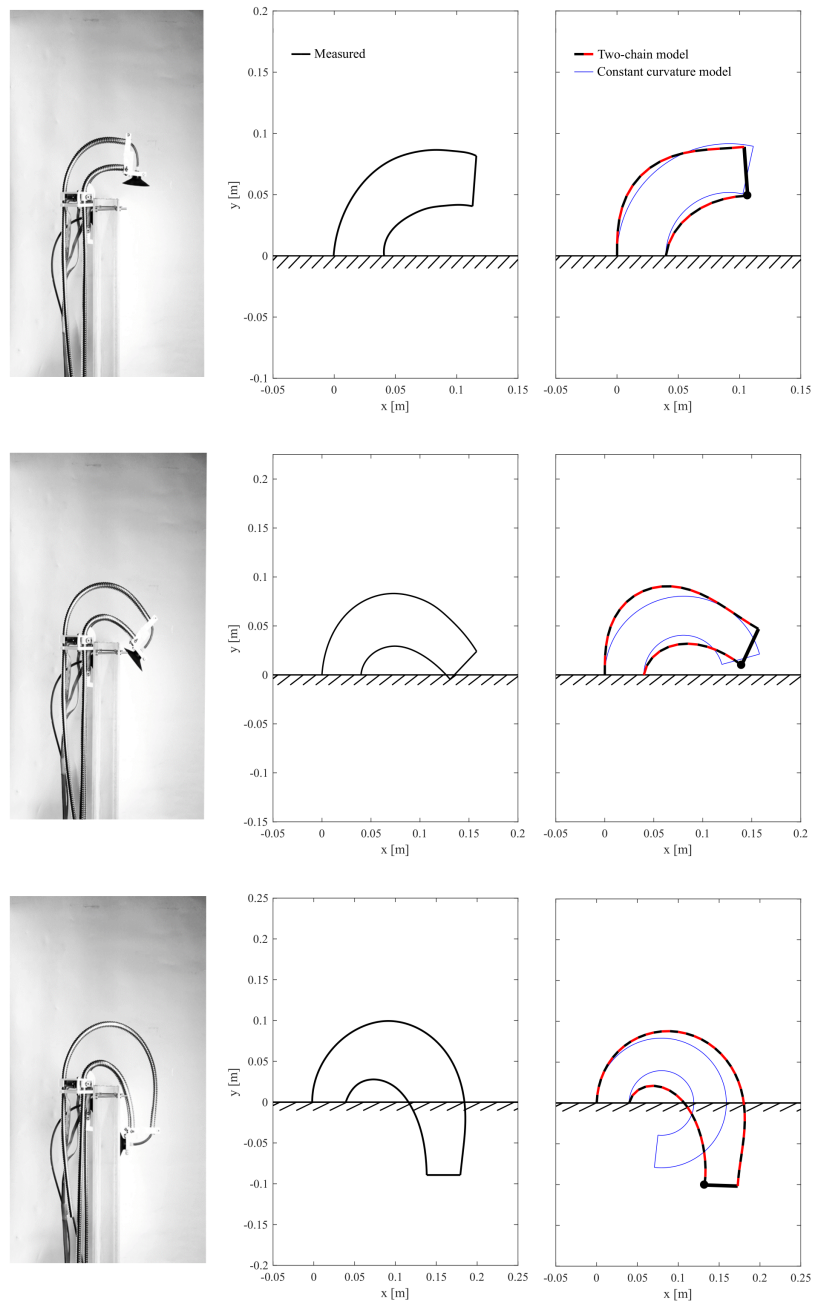


Fig. 3.13 Comparison of the flexible tube shape in simulation with the real world. The left images show the real robots attached on the vertical wall. The middle column of figures shows a simplified representation of the real robot deformations, and the figures on the right-hand side show the two-chain model and the constant curvature model.

Non-dimensional Shape Parameter

The constant curvature model is a kinematic model and, thus, describes the position of the end effector as a geometric property. In LEECH, the position also depends on the internal stiffness, mass distribution, gravity, and length of the extendable robot segments. When looking at the moment balance of a single chain in our model, one can see that the element angles depend only on these four parameters. For an element i , the moment balance reads

$$mg \sum_{j=i}^n x_j = -k(\phi_i - \phi_{i-1}) \quad (3.28)$$

where $\phi_0 = 0$. This is equal to

$$mg \sum_{j=i}^n \sum_{p=i}^j l \sin \phi_p = -k(\phi_i - \phi_{i-1}) \quad (3.29)$$

with m the mass per element, g gravity, x_j the x coordinate of the mass j as shown in Fig. 3.14, l the element length, k the torsional stiffness per element, and ϕ_i/l the angle of element i with respect to the frame of reference I . Thus, we have for the angle of element i

$$-\frac{1}{(\phi_i - \phi_{i-1})} \sum_{j=i}^n \sum_{p=i}^j \sin \phi_p = \frac{k}{mgl} \quad (3.30)$$

We see that the resulting angles are completely defined by the nondimensional parameter k/mgl which we will refer to as the shape parameter σ from here on. For any σ which remains constant, the resulting angles stay constant under the conditions that the number of elements does not change, that the initial conditions are identical, and that the payload m s at the tip is zero. This means that we can, for instance, change the size of the robot by changing l and guarantee the same robot shape as long as we change the other parameters to keep σ constant. Fig. 3.15 illustrates this using our model and changing stiffness, mass, and element length but keeping σ constant. We see that for all configurations the overall shape does not change although the size of the robot may. For all cases, the vector pointing to r_c which is located at the tip of chain 2 is located at the coordinates $[20l, 6l]$ irrespective of size. This is particularly interesting in the third case where we changed the element length which led to a further reach than in the other cases. Note, however, that we also adapted the chain distance at the bottom and top by the same factor as the element length. Interestingly, such a scaling is relevant in the natural world. For example, although caterpillars increase their body weight by 10,000 times in 2 weeks, they maintain the same locomotion kinematics by changing muscle activation and therefore the stiffness k [102].

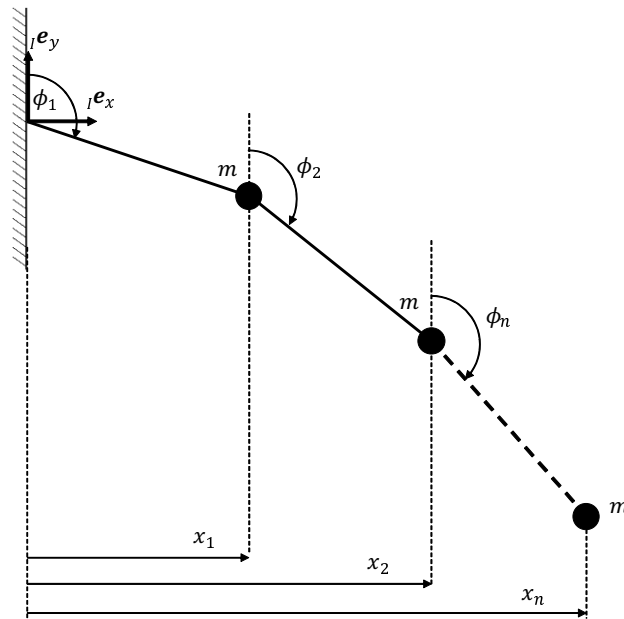
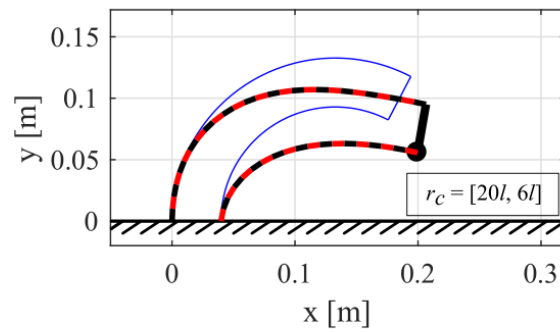


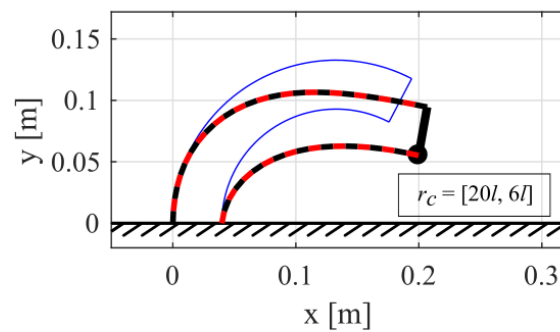
Fig. 3.14 One-chain model of n elements used for the derivation of the shape parameter σ

Fig. 3.16 shows how the two-chain model approaches the constant curvature model when stiffness and mass are changed, giving rise to different shape parameters σ . We set the endpoints of the constant curvature model to draw a linear curve and compared to that of our model with different stiffness parameters. The predicted endpoints in the simulation decline greatly due to the effects of gravity when σ is low, that is, close to that of our real robot. As σ increases, our model becomes stiffer and approaches the constant curvature model, but it does not match it completely. This is probably because the difference in the number of elements n and tubes in the left and right generates different bending moments in the two chains.

$\sigma = 824$: $k = 55 \text{ mNm/rad}$, $m = 0.68 \text{ g}$, $l = 10 \text{ mm}$



$\sigma = 824$: $k = 1000 \text{ mNm/rad}$, $m = 12.36 \text{ g}$, $l = 10 \text{ mm}$



$\sigma = 824$: $k = 275 \text{ mNm/rad}$, $m = 0.68 \text{ g}$, $l = 50 \text{ mm}$

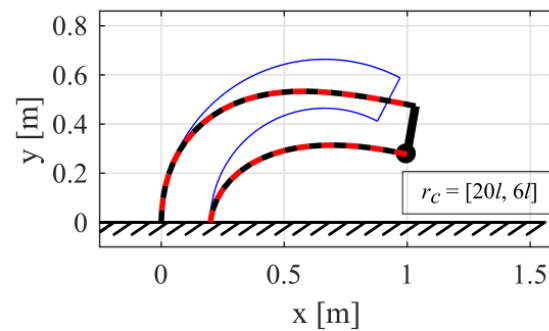


Fig. 3.15 Deformation for constant shape parameter σ but changing stiffness k , mass m , and element length l . The constant guarantees the same robot shape under certain conditions such as the number of elements n does not change.

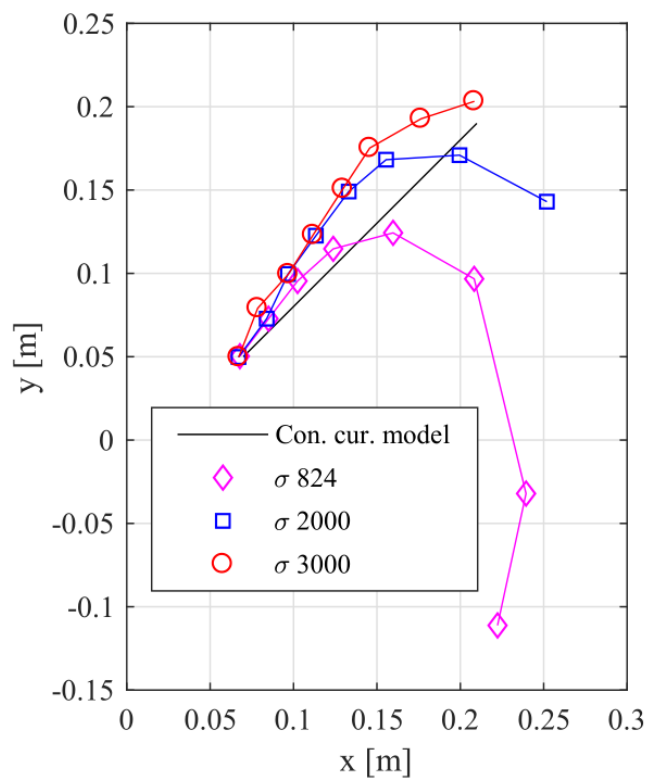


Fig. 3.16 Comparison between the predicted endpoints of the constant curvature model and the two-chain model when changing the shape parameter σ by changing stiffness k and mass m . The constant guarantees the same stiffness of the robot as long as element length l and gravitational acceleration g are constant even when changing the robot size by changing the number of elements n .

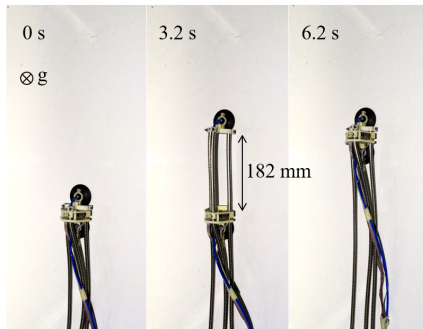
Locomotion

The lengthening based on the rack and pinion mechanism using flexible tubes enables the robot to deform greatly, augmenting reachability in locomotion. To understand the locomotion behavior in our robot, six types of locomotion maneuvers were tested on a plastic plate as shown in Fig. 3.17. On the flat ground, the tube length can be increased without buckling because the robot does not apply its load on the flexible tubes. A maximum speed of 20 mm/s was observed at a maximal tube length of 180mm (left top figure).

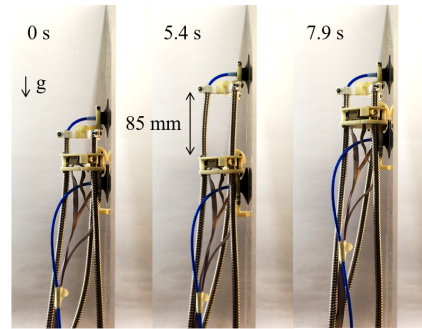
The robot also achieved upward and downward climbing locomotion on a vertical wall (right top and left middle figures). We can see that the tube lengths when climbing downward are shorter than when climbing upward. This is to guarantee that the rear suction cup is parallel to the wall at the point when it is being pressed against it. The middle right figure shows a sideway climbing maneuver. After the front suction cup with a free rotation joint is attached to the wall, the robot releases the rear suction cup and turns due to gravity, recovering the original posture. Note that this strategy for sideway climbing allows lateral movement but prevents steering of the entire robot (e.g., from vertical position to horizontal position) on vertical walls. If the free rotation joint is fixed the robot can achieve these movements, but the passive self-righting of the body posture upon release of the rear suction cup would be lost. The current version of our robot therefore possesses a rotational joint for simplified climbing control.

Locomotion for the transition from the vertical wall to the ground (90° – 180° transition) and the climb over a wall (90° – 270° transition) are described (bottom figures). A climbing strategy which was not tested in our experiments is moving along a ceiling. This is currently not possible in our robot but can be achieved in future versions by improving the suction cup performance and reducing the robot weight. The robot was operated manually because when the tube lengths are long, autonomous control of the robot end is difficult due to its nonlinear deformation. An operator controls the motors to move the robot's end and looks for a touchdown position of the front suction cup. Note that the touchdown position of the front suction cup depends on that of the rear suction cup. The wall to ground transition and the thin wall transition take ~ 18 and 86 s, respectively. The latter is relatively slow because the driving unit is caught on the corner when getting over the wall.

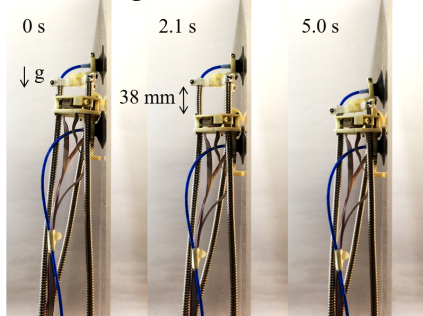
Walking on ground



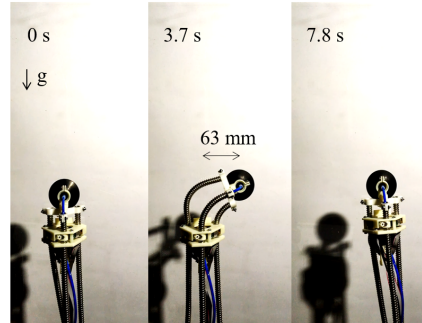
Climbing upward



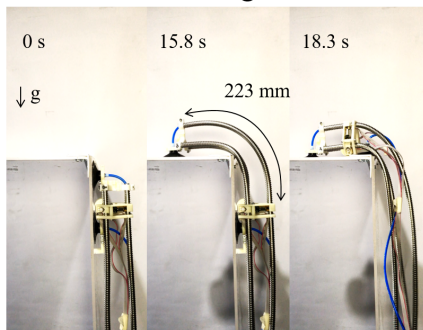
Climbing downward



Climbing sideward



Transition wall to ground



Transition over thin wall

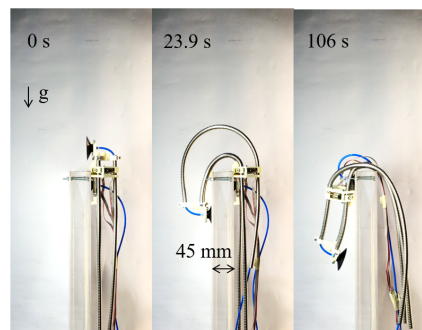


Fig. 3.17 Six types of locomotion maneuvers.

Reachability

In this study, we investigate to what extent the reachability with limited tube lengths is improved when using a multibody mechanics model as opposed to the constant curvature model. To do this, we set the range of each tube length from 0.05 to 0.3 m, varied each within this range, and numerically visualized the endpoints for each of these models for different shape parameter values σ as shown in Fig. 3.18. The shape parameter values are changed by changing only the element torsional stiffness k and element mass m as with Figure 10. Note that since we assume a scenario where the real robot gets over walls, the left tube is always longer than the right tube and the payload at the tip is set as m_s .

We can see that the downward reachability is greatly increased using the two-chain model when $\sigma = 824$ or less, as it allows us to utilize the effect of gravity and tube bending. Note that $\sigma = 824$ corresponds to LEeCH's shape parameter when using the parameters in Table 3.1. Moreover, we can increase the upward reachability by increasing the shape parameter σ . This shows that we can design the robot's reachability by changing its shape parameter. Conversely, we see that the upward reachability is better in the constant curvature model, because gravity is not influencing the kinematic posture. It can also reach points in the neighborhood somewhat lower than the origin that cannot be accessed with the two-chain model.

The results show that both models have their unique advantages. While the constant curvature model can target specific points in space precisely, it does not take into account the effect of external forces and thus cannot exploit properties of the physical environment such as gravity. In the two-chain model, we can exploit the environment to extend its workspace, but cannot turn beyond 180° without help (e.g., environmental constraints). In continuum robots, both properties are needed depending on the problem. For example, accurate positioning is required in medical application such as endoscopes [10], while soft deformations are beneficial for moving and climbing in unstructured environments [71, 32]. In practical applications, stiffness parameters should be tunable depending on desired reachability. Even robots having poor upward reachability, that is low stiffness, can climb walls with the help of environmental constraints, but decreasing stiffness leads to difficult controllability of their body ends.

3.3.4 Conclusion

To demonstrate the potential of a climbing robot with large deformation, we built a Longitudinally Extensible Continuumrobot inspired by Hirudinea, or LEeCH. An extensible body based on a rack and pinion mechanism can increase reachability of the robot end effector.

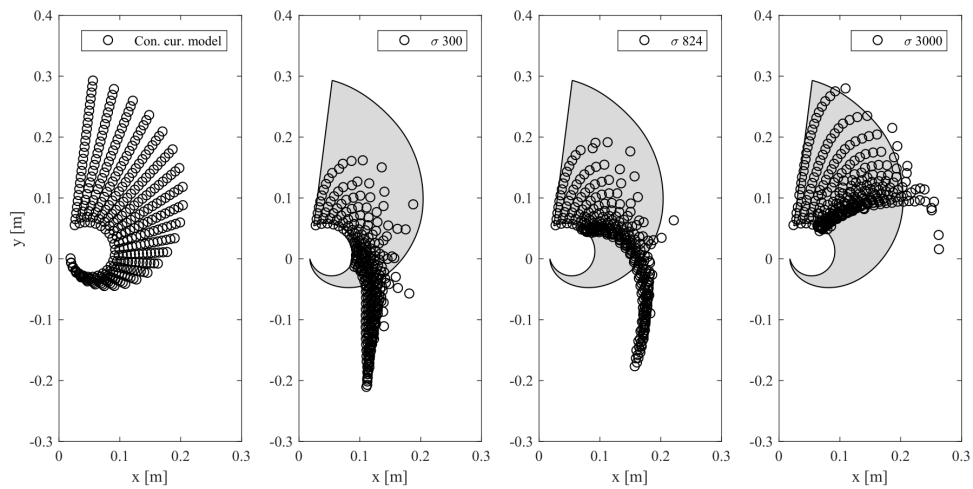


Fig. 3.18 Manipulator workspace for constant curvature and two-chain model when changing the shape parameter σ by changing only stiffness k and mass m as with Figure 10. Circles show the reachable points of the end effector, and the gray area indicates the reachable area of the constant curvature model.

The use of flexible tubes (stripwound metal hoses) as the rack showed great advantages for continuum robots: (1) flexible yet strong and (2) robust engagement with gears. Six types of locomotion, including wall-to-wall transition, were tested to demonstrate the robot's capability, and we found that large deformation is beneficial in certain situations. While our first prototype is inspired by the leech's basic morphology and locomotion, we are currently planning to adopt other features such as their special suckers and multiple muscles for grasping in unstructured substrates and achieving more complex tasks [103]. Compared to the constant curvature model, the two-chain model based on multibody mechanics can accurately predict the real robot's deformation and improve the downward reachability under gravity. The motion studied in our work can be expressed in a planar model; however, more complex movements will involve rotations and motions out of the plane which require more degrees of freedom to be considered. In future work, we will extend our 2D model to 3D and allow for additional physical effects such as twist or stretch.

Moreover, we derived the nondimensional morphological parameter which defines the robot's shape and showed that the desired reachability can be designed by changing this parameter. In a real system, a change of shape parameter can be achieved by modifying system size, stiffness, mass density, or gravity. As the latter two are hard to alter and the system size might be constrained by the particular task at hand, a change in stiffness appears to be a reasonable tuning parameter, which could be achieved using variable stiffness actuators.

In future work, we will investigate such mechanisms for live changes in shape parameters. Our study helps lay the foundation for soft robots that achieve complex locomotion such as overcoming obstacles and transitioning from wall to wall while using large and nonlinear deformation.

Chapter 4

Conclusion and Future Work

4.1 Conclusion

In this thesis, the concept of the flexible linear motor was described and its benefits for the locomotion of continuum robots were presented. Flexible linear motors are actuators combined soft and classical technologies, meaning that they are composed of a rigid stator of traditional motors and a flexible shaft of which appearance is similar to soft actuators. By moving the flexible shaft linearly via changes of a relative position to the stator, flexible linear motors provide a large stroke that can not be achieved with soft actuators that change themselves with internal stress. This thesis described two flexible linear motors: the flexible ultrasonic motor and the flexible rack pinion actuator. In Chapter 2, we proposed the flexible ultrasonic motor, argued the modeling, sensing, and design methodology, and demonstrated a 2 DoF continuum robot with self sensing sensor. In Chapter 3, we built mobile continuum robots using flexible rack pinion actuators and demonstrated that large strokes are useful for locomotion and climbing. Here, we will consider the findings and contributions obtained through this research.

Our research started with thinking about how to realize flexible linear motors. It is not easy to move a flexible drive shaft. For example, when the flexible drive shaft is driven by electromagnetic or electrostatic forces, the distance between the stator and the shaft cannot be kept constant due to the shaft's flexibility, and the driving forces may not be transmitted. In other words, such driving principles that the force changes greatly depending on the distance are not suitable for flexible linear motors. Our idea was the use of friction-driven stators with a through hole, and shafts with anisotropy rigidity. The shafts that are flexible in the bending direction but rigid in the circumferential direction are inserted in the stator hole. The circumferential rigidity keeps the distance between the shaft and stator constant and helps to stably receive driving friction forces such as a vibration and gear feed. This thesis reported

an ultrasonic vibration and a rack and pinion mechanism as examples of driving principles suitable for flexible linear motors.

The application of flexible linear motors to robots was also studied. Flexible linear motors are applied to all kinds of soft robots, but the most effective application is possibly continuous robots. The flexible linear motors have advantages such as electric drive, high response, and easy to control (easily assemble feedback loops), but particularly important is a large stroke. We showed that the large stroke improves the workspace and mobilities of continuum robots. Another advantage of flexible linear motors is sensing. Most soft actuators suffer from sensing with the use of traditional sensors whose rigidity preclude actuator's compliance. On the other hand, flexible linear motors succeeded a feedback control by using position sensors such as variable a resistance and encoder. Although these sensors cannot detect bending or torsion of the flexible shaft, the position of the continuum robot end is geometrically calculated from the length of the shafts.

4.2 Future Work

There are many opportunities for future developments of flexible linear motors. For example, one problem is to prevent an uncontrolled rotational or helical degree of freedom of the flexible shafts. Both flexible linear motors we proposed have no constraint to restrict the rotation. In the flexible ultrasonic motors, the linear motion of the coil spring slider might be with a slight rotational motion. In the flexible rack pinion actuator, even when the position of the driving unit is fixed, the axial rotation of the flexible tube is still possible due to the helical pitch of the tube grooves. One solution to this problem is to make the rotational motion controllable. For example, since the flexible ultrasonic motor is based on a rotary linear motion motor, the rotary motion can be controlled independently using a driving principle different from the one used for linear motion. Another solution is to prevent the rotation. Making the cross-section of the flexible shaft square may eliminate the rotational instability.

Another opportunity for improvement is the reduction in controllability as the shaft lengths increase, which makes it difficult to position the robot end. One way to improve controllability is to increase the number of the driving units controlling the flexible shafts. This allows the continuum robot using the flexible linear motors not only to assume various shapes but also to control the stiffness by changing the distance between the driving units.

References

- [1] B. Dynamics, <https://www.bostondynamics.com/atlas>, 2019.
- [2] H.-W. Park, M. Y. Chuah, and S. Kim, “Quadruped bounding control with variable duty cycle via vertical impulse scaling,” in *2014 IEEE/RSJ International Conference on Intelligent Robots and Systems (IROS)*, 2014, pp. 3245–3252.
- [3] H.-W. Park, P. Wensing, and S. Kim, “Online planning for autonomous running jumps over obstacles in high-speed quadrupeds,” in *Proceedings of Robotics: Science and Systems*, 2015.
- [4] C. Lee, M. Kim, Y. J. Kim, N. Hong, S. Ryu, H. J. Kim, and S. Kim, “Soft robot review,” *International Journal of Control, Automation and Systems*, vol. 15, no. 1, pp. 3–15, 2017.
- [5] D. Rus and M. T. Tolley, “Design, fabrication and control of soft robots,” *Nature*, vol. 521, no. 7553, pp. 467–475, 2015.
- [6] F. Iida and C. Laschi, “Soft robotics: challenges and perspectives,” *Procedia Computer Science*, vol. 7, pp. 99–102, 2011.
- [7] T. Owen, “Biologically inspired robots: Snake-like locomotors and manipulators,” *Robotica*, vol. 12, no. 3, pp. 282–282, 1994.
- [8] U. Robots, <https://www.universal-robots.com/>, 2019.
- [9] I. D. Walker, “Continuous backbone “continuum” robot manipulators,” *ISRN robotics*, vol. 2013, pp. 1–19, 2013.
- [10] J. Burgner-Kahrs, D. C. Rucker, and H. Choset, “Continuum robots for medical applications: A survey,” *IEEE Transactions on Robotics*, vol. 31, no. 6, pp. 1261–1280, 2015.
- [11] V. Anderson, R. Horn, and A. S. of Mechanical Engineers, *Tensor Arm Manipulator Design*, ser. American Society of Mechanical Engineers. Papers. American Society of Mechanical Engineers, 1967. [Online]. Available: <https://books.google.co.jp/books?id=Zc7QtgAACAAJ>
- [12] C. Laschi, M. Cianchetti, B. Mazzolai, L. Margheri, M. Follador, and P. Dario, “Soft robot arm inspired by the octopus,” *Advanced Robotics*, vol. 26, no. 7, pp. 709–727, 2012.

- [13] M. Calisti, G. Picardi, and C. Laschi, "Fundamentals of soft robot locomotion," *Journal of The Royal Society Interface*, vol. 14, no. 130, p. 20170101, 2017.
- [14] D. Trivedi, C. D. Rahn, W. M. Kier, and I. D. Walker, "Soft robotics: Biological inspiration, state of the art, and future research," *Applied Bionics and Biomechanics*, vol. 5, no. 3, pp. 99–117, 2008.
- [15] W. M. Kier and K. K. Smith, "Tongues, tentacles and trunks: the biomechanics of movement in muscular-hydrostats," *Zoological Journal of the Linnean Society*, vol. 83, no. 4, pp. 307–324, 1985.
- [16] D. B. Camarillo, C. F. Milne, C. R. Carlson, M. R. Zinn, and J. K. Salisbury, "Mechanics modeling of tendon-driven continuum manipulators," *IEEE Transactions on Robotics*, vol. 24, no. 6, pp. 1262–1273, 2008.
- [17] I. A. Gravagne, C. D. Rahn, and I. D. Walker, "Large deflection dynamics and control for planar continuum robots," *IEEE/ASME Transactions on Mechatronics*, vol. 8, no. 2, pp. 299–307, 2003.
- [18] H.-S. Yoon and B.-J. Yi, "A 4-dof flexible continuum robot using a spring backbone," in *2009 International Conference on Mechatronics and Automation (ICMA)*, 2009, pp. 1249–1254.
- [19] N. Simaan, K. Xu, W. Wei, A. Kapoor, P. Kazanzides, R. Taylor, and P. Flint, "Design and integration of a telerobotic system for minimally invasive surgery of the throat," *The International Journal of Robotics Research*, vol. 28, no. 9, pp. 1134–1153, 2009.
- [20] J. Ding, R. E. Goldman, K. Xu, P. K. Allen, D. L. Fowler, and N. Simaan, "Design and coordination kinematics of an insertable robotic effectors platform for single-port access surgery," *IEEE/ASME Transactions on Mechatronics*, vol. 18, no. 5, pp. 1612–1624, 2012.
- [21] K. Zhang, C. Qiu, and J. S. Dai, "An extensible continuum robot with integrated origami parallel modules," *Journal of Mechanisms and Robotics*, vol. 8, no. 3, p. 031010, 2016.
- [22] R. J. Webster III, J. M. Romano, and N. J. Cowan, "Mechanics of precurved-tube continuum robots," *IEEE Transactions on Robotics*, vol. 25, no. 1, pp. 67–78, 2008.
- [23] P. E. Dupont, J. Lock, B. Itkowitz, and E. Butler, "Design and control of concentric-tube robots," *IEEE Transactions on Robotics*, vol. 26, no. 2, pp. 209–225, 2009.
- [24] I. D. Walker, D. Nahar, S. Verma, M. B. Wooten, and A. D. Kapadia, "Challenges in creating long continuum robots," in *2016 21st International Conference on Methods and Models in Automation and Robotics (MMAR)*, 2016, pp. 339–344.
- [25] T.-D. Nguyen and J. Burgner-Kahrs, "A tendon-driven continuum robot with extensible sections," in *2015 IEEE/RSJ International Conference on Intelligent Robots and Systems (IROS)*, 2015, pp. 2130–2135.

- [26] A. Kapoor, N. Simaan, and R. H. Taylor, "Suturing in confined spaces: constrained motion control of a hybrid 8-dof robot," in *12th International Conference on Advanced Robotics*, 2005, pp. 452–459.
- [27] M. B. Pritts and C. D. Rahn, "Design of an artificial muscle continuum robot," in *2004 IEEE International Conference on Robotics and Automation (ICRA)*, vol. 5, 2004, pp. 4742–4746.
- [28] G. Chen, M. T. Pham, and T. Redarce, "A guidance control strategy for semi-autonomous colonoscopy using a continuum robot," in *Proceedings of The International Conference on Advanced Robotics (ICAR)*, 2008, pp. 63–78.
- [29] A. Bartow, A. Kapadia, and I. Walker, "A novel continuum trunk robot based on contractor muscles," in *Proceedings of the 12th WSEAS International Conference on Signal Processing, Robotics, and Automation*, 2013, pp. 181–186.
- [30] S. Y. Kim, R. Baines, J. Booth, N. Vasios, K. Bertoldi, and R. Kramer-Bottiglio, "Reconfigurable soft body trajectories using unidirectionally stretchable composite laminae," *Nature Communications*, vol. 10, no. 1, pp. 1–8, 2019.
- [31] C. Urban, R. Gunther, T. Nagel, R. Richter, and R. Witt, "Development of a bendable permanent-magnet tubular linear motor," *IEEE Transactions on Magnetics*, vol. 48, no. 8, pp. 2367–2373, 2012.
- [32] T. L. Lam and Y. Xu, "Biologically inspired tree-climbing robot with continuum maneuvering mechanism," *Journal of Field Robotics*, vol. 29, no. 6, pp. 843–860, 2012.
- [33] K. Ohyama, Y. Hyakutake, and H. Kino, "Verification of operating principle of flexible linear actuator," in *2009 International Conference on Electrical Machines and Systems (ICEMS)*, 2009, pp. 1–6.
- [34] C. S. Haines, M. D. Lima, N. Li, G. M. Spinks, J. Foroughi, J. D. Madden, S. H. Kim, S. Fang, M. J. De Andrade, F. Göktepe *et al.*, "Artificial muscles from fishing line and sewing thread," *Science*, vol. 343, no. 6173, pp. 868–872, 2014.
- [35] R. V. Martinez, C. R. Fish, X. Chen, and G. M. Whitesides, "Elastomeric origami: programmable paper-elastomer composites as pneumatic actuators," *Advanced Functional Materials*, vol. 22, no. 7, pp. 1376–1384, 2012.
- [36] N. Kellaris, V. G. Venkata, G. M. Smith, S. K. Mitchell, and C. Keplinger, "Peano-hassel actuators: Muscle-mimetic, electrohydraulic transducers that linearly contract on activation," *Science Robotics*, vol. 3, no. 14, p. eaar3276, 2018.
- [37] M. Calisti, M. Giorelli, G. Levy, B. Mazzolai, B. Hochner, C. Laschi, and P. Dario, "An octopus-bioinspired solution to movement and manipulation for soft robots," *Bioinspiration & Biomimetics*, vol. 6, no. 3, p. 036002, 2011.
- [38] S. Seok, C. D. Onal, K.-J. Cho, R. J. Wood, D. Rus, and S. Kim, "Meshworm: a peristaltic soft robot with antagonistic nickel titanium coil actuators," *IEEE/ASME Transactions on Mechatronics*, vol. 18, no. 5, pp. 1485–1497, 2012.

- [39] H.-T. Lin, G. G. Leisk, and B. Trimmer, “Goqbot: a caterpillar-inspired soft-bodied rolling robot,” *Bioinspiration & Biomimetics*, vol. 6, no. 2, p. 026007, 2011.
- [40] A. Menciassi, S. Gorini, G. Pernorio, and P. Dario, “A sma actuated artificial earthworm,” in *2004 IEEE International Conference on Robotics and Automation (ICRA)*, vol. 4, 2004, pp. 3282–3287.
- [41] G. K. Klute, J. M. Czerniecki, and B. Hannaford, “Artificial muscles: Actuators for biorobotic systems,” *The International Journal of Robotics Research*, vol. 21, no. 4, pp. 295–309, 2002.
- [42] C.-P. Chou and B. Hannaford, “Measurement and modeling of mckibben pneumatic artificial muscles,” *IEEE Transactions on Robotics and Automation*, vol. 12, pp. 90–102, 1996.
- [43] T. V. J. Tarvainen and W. Yu, “Pneumatic multi-pocket elastomer actuators for metacarpophalangeal joint flexion and abduction-adduction,” *Actuators*, vol. 6, no. 3, 2017. [Online]. Available: <https://www.mdpi.com/2076-0825/6/3/27>
- [44] R. F. Shepherd, F. Ilievski, W. Choi, S. A. Morin, A. A. Stokes, A. D. Mazzeo, X. Chen, M. Wang, and G. M. Whitesides, “Multigait soft robot,” *Proceedings of the National Academy of Sciences*, vol. 108, no. 51, pp. 20400–20403, 2011. [Online]. Available: <https://www.pnas.org/content/108/51/20400>
- [45] K. Suzumori, “Elastic materials producing compliant robots,” *Robotics and Autonomous Systems*, vol. 18, no. 1, pp. 135–140, 1996.
- [46] T. Helps and J. Rossiter, “Proprioceptive flexible fluidic actuators using conductive working fluids,” *Soft Robotics*, vol. 5, no. 2, pp. 175–189, 2018, PMID: 29211627. [Online]. Available: <https://doi.org/10.1089/soro.2017.0012>
- [47] F. Schmitt, O. Piccin, L. Barbé, and B. Bayle, “Soft robots manufacturing: A review,” *Frontiers in Robotics and AI*, vol. 5, p. 84, 2018. [Online]. Available: <https://www.frontiersin.org/article/10.3389/frobt.2018.00084>
- [48] M. Okui, Y. Nagura, S. Iikawa, Y. Yamada, and T. Nakamura, “A pneumatic power source using a sodium bicarbonate and citric acid reaction with pressure booster for use in mobile devices,” in *2017 IEEE/RSJ International Conference on Intelligent Robots and Systems (IROS)*, Sep. 2017, pp. 1040–1045.
- [49] M. Wehner, R. L. Truby, D. J. Fitzgerald, B. Mosadegh, G. M. Whitesides, J. A. Lewis, and R. J. Wood, “An integrated design and fabrication strategy for entirely soft, autonomous robots,” *Nature*, vol. 536, no. 7617, p. 451, 2016.
- [50] V. Cacucciolo, J. Shintake, Y. Kuwajima, S. Maeda, D. Floreano, and H. Shea, “Stretchable pumps for soft machines,” *Nature*, vol. 572, no. 7770, pp. 516–519, 2019.
- [51] Y. Bar-Cohen, “Electroactive polymers as artificial muscles-reality and challenges,” in *Proceedings of the 42nd AIAA Meeting on Structural Dynamics and Materials*, vol. 1492, 2001, pp. 1–9.

- [52] E. Y. Yarbasi and E. Samur, "Design and evaluation of a continuum robot with extendable balloons," *Mechanical Sciences*, vol. 9, no. 1, pp. 51–60, 2018.
- [53] E. W. Hawkes, L. H. Blumenschein, J. D. Greer, and A. M. Okamura, "A soft robot that navigates its environment through growth," *Science Robotics*, vol. 2, no. 8, p. eaan3028, 2017.
- [54] S. Seok, C. D. Onal, R. Wood, D. Rus, and S. Kim, "Peristaltic locomotion with antagonistic actuators in soft robotics," in *2010 IEEE International Conference on Robotics and Automation (ICRA)*, 2010, pp. 1228–1233.
- [55] J. Z. Ge, A. A. Calderon, and N. O. Pérez-Arancibia, "An earthworm-inspired soft crawling robot controlled by friction," in *2017 IEEE International Conference on Robotics and Biomimetics (ROBIO)*, 2017, pp. 834–841.
- [56] A. S. Boxerbaum, A. D. Horchler, K. M. Shaw, H. J. Chiel, and R. D. Quinn, "A controller for continuous wave peristaltic locomotion," in *2011 IEEE/RSJ International Conference on Intelligent Robots and Systems (IROS)*, 2011, pp. 197–202.
- [57] H. Omori, T. Nakamura, and T. Yada, "An underground explorer robot based on peristaltic crawling of earthworms," *Industrial Robot*, vol. 36, no. 4, pp. 358–364, 2009.
- [58] B. Chu, K. Jung, C.-S. Han, and D. Hong, "A survey of climbing robots: Locomotion and adhesion," *International Journal of Precision Engineering and Manufacturing*, vol. 11, no. 4, pp. 633–647, 2010.
- [59] S. Nansai and R. E. Mohan, "A survey of wall climbing robots: recent advances and challenges," *Robotics*, vol. 5, no. 3, pp. 1–14, 2016.
- [60] M. F. Silva and J. T. Machado, "A survey of technologies and applications for climbing robots locomotion and adhesion," in *Climbing and walking robots*. InTech, 2010, pp. 1–22.
- [61] D. Schmidt and K. Berns, "Climbing robots for maintenance and inspections of vertical structures—a survey of design aspects and technologies," *Robotics and Autonomous Systems*, vol. 61, no. 12, pp. 1288–1305, 2013.
- [62] R. L. Tummala, R. Mukherjee, N. Xi, D. Aslam, H. Dulimarta, J. Xiao, M. Minor, and G. Dang, "Climbing the walls [robots]," *IEEE Robotics & Automation Magazine*, vol. 9, no. 4, pp. 10–19, 2002.
- [63] Y. Guan, H. Zhu, W. Wu, X. Zhou, L. Jiang, C. Cai, L. Zhang, and H. Zhang, "A modular biped wall-climbing robot with high mobility and manipulating function," *IEEE/ASME Transactions on Mechatronics*, vol. 18, no. 6, pp. 1787–1798, 2012.
- [64] G. Lee, H. Kim, K. Seo, J. Kim, and H. S. Kim, "Multitrack: A multi-linked track robot with suction adhesion for climbing and transition," *Robotics and Autonomous Systems*, vol. 72, pp. 207–216, 2015.
- [65] T. Seo and M. Sitti, "Tank-like module-based climbing robot using passive compliant joints," *IEEE/ASME Transactions on Mechatronics*, vol. 18, no. 1, pp. 397–408, 2012.

- [66] S. Kalouche, N. Wiltsie, H.-J. Su, and A. Parness, "Inchworm style gecko adhesive climbing robot," in *2014 IEEE/RSJ International Conference on Intelligent Robots and Systems (IROS)*, 2014, pp. 2319–2324.
- [67] L. S. Cowan and I. D. Walker, "Soft continuum robots-the interaction of continuous and discrete elements," in *Proceedings Artificial Life IX*, 2008, pp. 126–133.
- [68] M. A. Robertson and J. Paik, "New soft robots really suck: Vacuum-powered systems empower diverse capabilities," *Science Robotics*, vol. 2, no. 9, p. eaan6357, 2017.
- [69] Y. Tang, Q. Zhang, G. Lin, and J. Yin, "Switchable adhesion actuator for amphibious climbing soft robot," *Soft Robotics*, vol. 5, no. 5, pp. 592–600, 2018.
- [70] M. S. Verma, A. Ainla, D. Yang, D. Harburg, and G. M. Whitesides, "A soft tube-climbing robot," *Soft Robotics*, vol. 5, no. 2, pp. 133–137, 2018.
- [71] M. Malley, M. Rubenstein, and R. Nagpal, "Flippy: a soft, autonomous climber with simple sensing and control," in *2017 IEEE/RSJ International Conference on Intelligent Robots and Systems (IROS)*, 2017, pp. 6533–6540.
- [72] S. Ueha, Y. Tomikawa, M. Kurosawa, and N. Nakamura, *Ultrasonic motors: theory and applications*, ser. Monographs in electrical and electronic engineering. Clarendon Press, 1993. [Online]. Available: <https://books.google.co.jp/books?id=gOlSAAAAMAAJ>
- [73] T. Sashida and T. Kenjo, *An introduction to ultrasonic motors*. Clarendon Press Oxford, 1993. [Online]. Available: <https://books.google.co.jp/books?id=T1tpZk3TWe8C&dq=An+introduction+to+ultrasonic+motors&hl=ja&sa=X&ved=0ahUKEwjklfmxjuLnAhULyIsBHVatAqMQ6AEIKDAA>
- [74] K. Uchino, "Piezoelectric ultrasonic motors: overview," *Smart Materials and Structures*, vol. 7, no. 3, p. 273, 1998.
- [75] Y. Peng, Y. Peng, X. Gu, J. Wang, and H. Yu, "A review of long range piezoelectric motors using frequency leveraged method," *Sensors and Actuators A: Physical*, vol. 235, pp. 240–255, 2015.
- [76] T. Hemsell and J. Wallaschek, "Survey of the present state of the art of piezoelectric linear motors," *Ultrasonics*, vol. 38, no. 1-8, pp. 37–40, 2000.
- [77] B. Koc and K. Uchino, *Piezoelectric Ultrasonic Motors*, 12 2016.
- [78] T. Mashimo and S. Toyama, "Rotary-linear piezoelectric actuator using a single stator," *IEEE Transactions on Ultrasonics, Ferroelectrics, and Frequency Control*, vol. 56, no. 1, pp. 114–120, 2009.
- [79] T. Mashimo and S. Toyama, "Rotary-linear piezoelectric microactuator with a cubic stator of side length 3.5 mm," *IEEE Transactions on Ultrasonics, Ferroelectrics, and Frequency Control*, vol. 57, no. 8, pp. 1825–1830, 2010.
- [80] T. Mashimo and S. Toyama, "Vibration analysis of cubic rotary-linear piezoelectric actuator," *IEEE Transactions on Ultrasonics, Ferroelectrics, and Frequency Control*, vol. 58, no. 4, pp. 844–848, 2011.

- [81] T. Funakubo, T. Tsubata, Y. Taniguchi, K. Kumei, T. Fujimura, and C. Abe, "Ultrasonic linear motor using multilayer piezoelectric actuators," *Japanese Journal of Applied Physics*, vol. 34, no. 5B, pp. 2756–2759, 1995.
- [82] T. Funakubo and Y. Tomikawa, "Characteristics of 10 mm multilayer 11-f2 mode vibrator and application to a linear motor," *Japanese Journal of Applied Physics*, vol. 42, no. 5, pp. 3002–3006, 2003.
- [83] K. Takemura and T. Maeno, "Design and control of an ultrasonic motor capable of generating multi-dof motion," *IEEE/ASME Transactions on Mechatronics*, vol. 6, no. 4, pp. 499–506, 2001.
- [84] M. Aoyagi, S. P. Beeby, and N. M. White, "A novel multi-degree-of-freedom thick-film ultrasonic motor," *IEEE Transactions on Ultrasonics, Ferroelectrics, and Frequency Control*, vol. 49, no. 2, pp. 151–158, 2002.
- [85] C. Truesdell, "Timoshenko's history of strength of materials (1953)," in *An Idiot's Fugitive Essays on Science*. Springer, 1984, pp. 251–253.
- [86] K. Nakamura, M. Kurosawa, H. Kurebayashi, and S. Ueha, "An estimation of load characteristics of an ultrasonic motor by measuring transient responses," *IEEE Transactions on Ultrasonics, Ferroelectrics, and Frequency Control*, vol. 38, no. 5, pp. 481–485, 1991.
- [87] A. M. Flynn, "Piezoelectric ultrasonic micromotors," Ph.D. dissertation, Massachusetts Institute of Technology, 1995.
- [88] T. Mashimo and K. Terashima, "Dynamic analysis of an ultrasonic motor using point contact model," *Sensors and Actuators A: Physical*, vol. 233, pp. 15–21, 2015.
- [89] J. Wu, Y. Mizuno, and K. Nakamura, "Polymer-based ultrasonic motors utilizing high-order vibration modes," *IEEE/ASME Transactions on Mechatronics*, vol. 23, no. 2, pp. 788–799, 2018.
- [90] R. J. Webster III and B. A. Jones, "Design and kinematic modeling of constant curvature continuum robots: A review," *The International Journal of Robotics Research*, vol. 29, no. 13, pp. 1661–1683, 2010.
- [91] O. Azami, D. Morisaki, T. Miyazaki, T. Kanno, and K. Kawashima, "Development of the extension type pneumatic soft actuator with built-in displacement sensor," *Sensors and Actuators A: Physical*, vol. 300, p. 111623, 2019.
- [92] A. Sadeghi, A. Mondini, E. Del Dottore, V. Mattoli, L. Beccai, S. Taccola, C. Lucarotti, M. Totaro, and B. Mazzolai, "A plant-inspired robot with soft differential bending capabilities," *Bioinspiration & Biomimetics*, vol. 12, no. 1, p. 015001, 2016.
- [93] K. Hsiao and H. Mochiyama, "A wire-driven continuum manipulator model without assuming shape curvature constancy," in *2017 IEEE/RSJ International Conference on Intelligent Robots and Systems (IROS)*, 2017, pp. 436–443.

- [94] J. Jung, R. S. Penning, N. J. Ferrier, and M. R. Zinn, "A modeling approach for continuum robotic manipulators: Effects of nonlinear internal device friction," in *2011 IEEE/RSJ International Conference on Intelligent Robots and Systems (IROS)*, 2011, pp. 5139–5146.
- [95] H. Marvi, C. Gong, N. Gravish, H. Astley, M. Travers, R. L. Hatton, J. R. Mendelson, H. Choset, D. L. Hu, and D. I. Goldman, "Sidewinding with minimal slip: Snake and robot ascent of sandy slopes," *Science*, vol. 346, no. 6206, pp. 224–229, 2014.
- [96] K. Quillin, "Ontogenetic scaling of hydrostatic skeletons: geometric, static stress and dynamic stress scaling of the earthworm *lumbricus terrestris*," *Journal of Experimental Biology*, vol. 201, no. 12, pp. 1871–1883, 1998.
- [97] M. W. Hannan and I. D. Walker, "Kinematics and the implementation of an elephant's trunk manipulator and other continuum style robots," *Journal of Robotic Systems*, vol. 20, no. 2, pp. 45–63, 2003.
- [98] B. A. Jones and I. D. Walker, "Kinematics for multisection continuum robots," *IEEE Transactions on Robotics*, vol. 22, no. 1, pp. 43–55, 2006.
- [99] G. S. Chirikjian and J. W. Burdick, "A modal approach to hyper-redundant manipulator kinematics," *IEEE Transactions on Robotics and Automation*, vol. 10, no. 3, pp. 343–354, 1994.
- [100] K. Xu and N. Simaan, "Analytic formulation for kinematics, statics, and shape restoration of multibackbone continuum robots via elliptic integrals," *Journal of Mechanisms and Robotics*, vol. 2, no. 1, p. 011006, 2010.
- [101] D. Trivedi, A. Lotfi, and C. D. Rahn, "Geometrically exact models for soft robotic manipulators," *IEEE Transactions on Robotics*, vol. 24, no. 4, pp. 773–780, 2008.
- [102] H.-T. Lin, D. J. Slate, C. R. Paetsch, A. L. Dorfmann, and B. A. Trimmer, "Scaling of caterpillar body properties and its biomechanical implications for the use of a hydrostatic skeleton," *Journal of Experimental Biology*, vol. 214, no. 7, pp. 1194–1204, 2011.
- [103] T. Kampowski, L. Eberhard, F. Gallenmüller, T. Speck, and S. Poppinga, "Functional morphology of suction discs and attachment performance of the mediterranean medicinal leech (*hirudo verbana carena*)," *Journal of The Royal Society Interface*, vol. 13, no. 117, p. 20160096, 2016.

Appendix A

Experimental Verification of the Strain Energy

In 2.9, we estimated the strain energy of the coil spring by the model of the bending deformation of the Euler–Bernoulli beam. There is another computational method for the strain energy using the bending moment [23]. The advantage of using the bending moment is that shows the strain energy from the angular displacement by a simple experiment. In this section, we derive the strain energy using the bending moment and verify it experimentally. We consider the case that the coil spring inserted to the stator hole generates the pre-pressure P between the stator and coil (Figure 2.17(a)). At this time, the bending moment M acts both the ends of the coil spring and makes the beam planes either lengthen or shorten, thereby creating strains. The bending moment is expressed by integrating the strains:

$$M = \int_A E \epsilon y dA \quad (\text{A.1})$$

where dA is the differential element of the beam area. In the Euler–Bernoulli beam, the bending moment M can be solved from a given angular displacement ϕ . This is expressed as

$$\phi = \frac{ML}{EI} \quad (\text{A.2})$$

ϕ can be geometrically determined by the parameters of the coil spring and the hole diameter. Using the relation between ϕ and M , the strain energy U_s is rewritten to

$$U_s = \frac{M^2 L}{2EI} \quad (\text{A.3})$$

The energy U_s equals to the strain energy derived in 2.8.

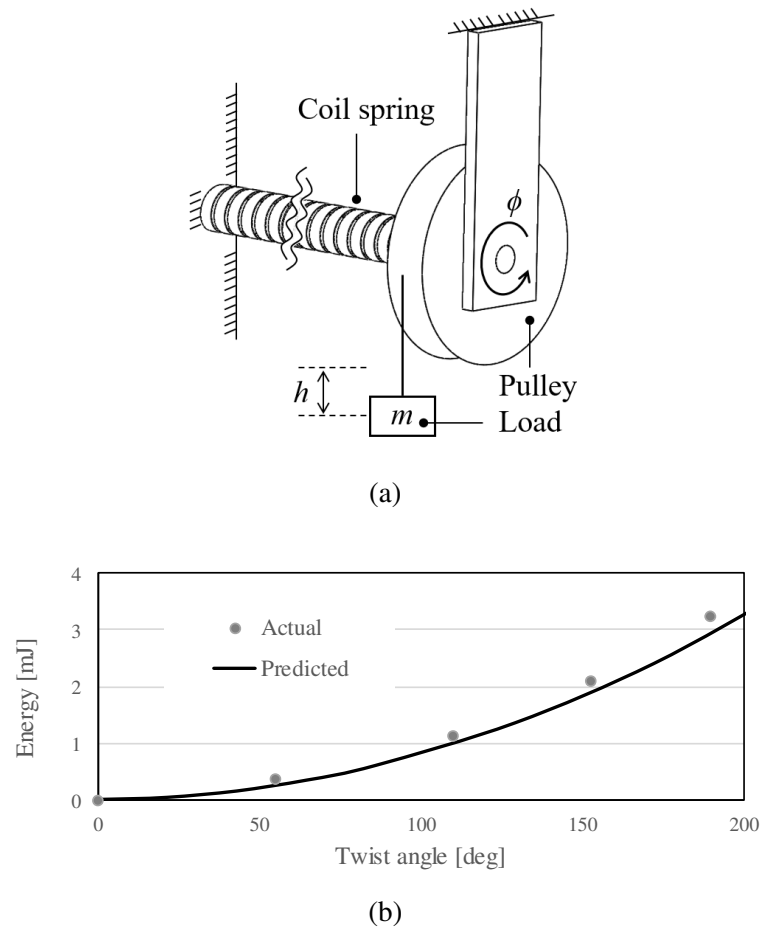


Fig. A.1 Strain energy stored by the twist of the coil spring. The strain energy estimated is accorded to the experimental result obtained from the change in the potential energy.

Let us confirm the relation between the strain energy and the angular displacement experimentally. Figure A.1(a) shows the experimental setup. One end of the coil spring is fixed and the other free end is attached to a pulley. The coil spring has a diameter of 11 mm and a wire total length of 310 mm. A weight is loaded to the string connected to the pulley that fixes the free end. When a weight is applied, it moves downwards due to gravity and twists the coil spring with an angular displacement ϕ circumferentially. In this case, the strain energy stored by the twist is equal to the work done by the displacement of the weight. It is described as a half of the potential energy of the weight m and the change in height h :

$$U_p = \frac{1}{2}mgh \quad (\text{A.4})$$

This value should take the same value as the strain energies in (A3). Figure A.1(b) shows the

experimental behavior of U_s and U_p when ϕ and h are determined. The plots obtained in the change in the displacement of the mass are in good agreement with the curve of the strain energy. This fact means that the strain energy computed by 2.8 and (A3) is correct.